Slices of theoretical astrophysics: solar system dynamics and relativistic explosions

Thesis by

Margaret Pan

in partial fulfillment of the requirements

for the degree of

Doctor of Philosophy

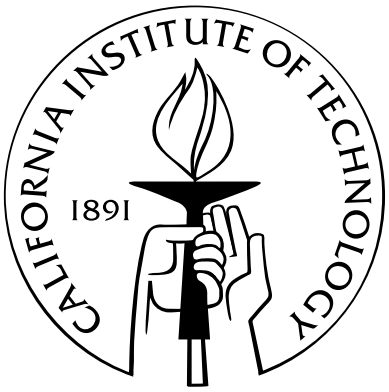

California Institute of Technology

Pasadena, California

2006

(Defended May 23, 2006)

Abstract

This thesis presents studies in two distinct areas of theoretical astrophysics: dynamics of planetary systems and relativistic fluid flows from shocks emerging from stellar envelopes. The first pertains to the early solar system, planet formation, and extrasolar planets; the second is related to extreme explosions like gamma-ray bursts and supernovae.

We present two investigations of the dynamics and population evolution of solar system bodies. First, we explore the dynamics of mean-motion resonances for a test particle in a highly eccentric long-period orbit in the restricted circular planar three-body problem—a scenario relevant to the scattered Kuiper belt and the formation of the Oort cloud. We find infinitely many analogues to the Lagrange points; an explanation for the presence of asymmetric librations in particular mean-motion resonances; and a criterion for the onset of chaos at large semimajor axes.

Second, we study the size distribution of Kuiper belt objects (KBOs), which is observed to be a broken power law. We apply a simple mass conservation argument to the KBO collisional cascade to get the power-law slope for KBOs below the break in the distribution; our result agrees well with observations if KBOs are held together by self-gravity rather than material strength. We then explain the location and time evolution of the break.

We also present investigations of the flow that results when a relativistic shock propagates through and breaks out of a stellar envelope with a polytropic density profile. This work informs predictions of the speed of and energy carried by the relativistic ejecta in supernovae and perhaps in gamma-ray bursts. We find the asymptotic solution for the flow as the shock reaches the star's edge and find a new self-similar

solution for the flow of hot fluid after breakout. Since the post-breakout flow accelerates by converting thermal energy into bulk kinetic energy, the fluid eventually cools to nonrelativistic temperatures. We derive a second new self-similar solution that includes the cooling portions of the flow. This second solution gives an exact relation between the terminal Lorentz factor of each fluid element and the Lorentz factor it acquired upon being shocked before breakout.

Acknowledgements

The truth is, I've really enjoyed being a graduate student, and most of my good experience is due the people I've known while at Caltech.

First of all, I'm very grateful to Re'em Sari for everything he has done for me and for all the care he has put into my education. I couldn't have asked for a better advisor and mentor than Re'em: almost entirely because of him, graduate school has been the best academic experience of my life. I've taken great pleasure in learning from someone whom I respect so much for his scientific insight and innovations, high standards, and wonderfully clear explanations. Re'em has also been a good friend to me, and I'm lucky to have benefitted from his great generosity, kindness, patience, and tact as well as his infectious enthusiasm for figuring out how things work.

Without Peter Goldreich's planetary dynamics class, I'd almost certainly have become an observer. I'd like to thank Peter for introducing me to theory and for keeping a benevolent eye on my scientific and athletic affairs long after he ceased to be officially responsible for me. I'm glad to have collaborated with Mike Brown, and I want to thank him for that and for all the Kuiper belt gossip that I got to hear at his group meetings.

I'd like to thank my friends at Caltech for their company, encouragement, and diversions. In particular, Milan Bogosavljević, Stuartt Corder, Melissa Enoch, Laura Hainline, and Cathy Slesnick provided much-needed support and comic relief during our first two years in the Robinson dungeons. Alison Farmer shared many racquetball, rock climbing, and meringue-eating sessions with me and added a healthy dose of spice to life in Tapir. My academic siblings, Ben Collins and Hilke Schlichting, are

responsible for many amusing and enlightening discussions (with and without coffee) on just about anything. I'll miss chatting with Miloš Milosavljević late at night. I've enjoyed living with Karín Menéndez-Delmestre, Thiago Gonçalves, and Elina Brobeck, and I appreciate their kindness and their patience with my erratic schedule.

As always, I'm grateful to my parents, my sister Alice, and my brother David for caring so much about me, and for their continuing support.

Thank you all so much!

Contents

List of Figures

List of Tables

Chapter 1

Introduction

While "theoretical astrophysics" includes an enormous range of phenomena, relates to nearly all the physics now known, and spans, for example, size scales ranging from neutron stars ($\sim 10^6$ cm) to the observable universe ($\sim 10^{28}$ cm), the same principles and techniques recur surprisingly often in studies of different phenomena. The dynamical friction that operates on dwarf galaxies in rich clusters also applies to protoplanets in a circumstellar disk; turbulence that in the earth's atmosphere blurs stars seen from the ground also manifests itself as galactic blobs of gas that cause scintillation of Sagittarius A* and compact extragalactic sources. As a result, theoretical astrophysics remains a field in which ongoing curiosity about and investigations into subfields outside one's own specialty is tolerated and even encouraged, valued, and widely practiced.

In that spirit of continuing broad education, this thesis presents investigations into two very different areas of theoretical astrophysics: applications of planetary dynamics and self-similar solutions for relativistic shocks in the envelopes of exploding stars. These topics are introduced separately below.

1.1 Small bodies in the solar system

Chapters 2 and 3 describe the dynamics and population evolution of small bodies in the solar system including, in particular, Kuiper belt objects (KBOs) and comets. The Kuiper belt is a collection of bodies smaller than a few thousand kilometers in size

which are believed to consist of ice and rock. While most KBOs reside in a puffy disk—the "classical belt"—between 30 and 50 AU from the sun, a significant fraction—the "scattered disk"—are characterized by long-period orbits with high eccentricities and inclinations probably acquired through interactions with Neptune. By contrast, most comets are believed to reside in the Oort cloud, a spherically symmetric population located ∼10,000 AU from the sun. The Oort cloud is believed to have formed as the giant planets perturbed nearby small bodies onto high-eccentricity long-period orbits that were later circularized by passing stars or galactic tides.

Both KBOs and comets are interesting and important to our understanding of planetary systems for several reasons. First, small, cold bodies like comets and KBOs are some of the least processed bodies in the solar system since they were never subject to the heat or pressure associated with the accretion and differentiation of the major planets. As such, comets and KBOs are relics of the early solar system; an understanding of, for example, their size distribution and composition may provide clues to early solar system composition and the accretion process.

Also, while the planets were forming, numerous small bodies provided a mass reservoir for accretion and constrained the major planets' velocity evolution. Since small bodies now contain much less mass than the planets and are concentrated in just a few regions, most of the small bodies must have been removed. Small-body reservoirs like the Kuiper belt represent the tail end of the removal process; comets were removed from areas near the giant planets' orbits. The Kuiper belt and Oort cloud may therefore shed light on the final stages of planet formation and the fate of the disappearing planetesimals and dust.

Finally, interactions between small bodies and the giant planets should have caused the giant planets' orbits to migrate and evolve. An analysis of small-body orbits may yield a picture of how and why the planets attained their current marginally stable configuration and why this configuration looks so different from most other planet systems seen to date. An understanding of the small-body populations in our solar system may thus also inform investigations into the formation and evolution of extrasolar planetary systems.

1.1.1 Eccentric test particles and analogues to the Lagrange points

Chapter 2 describes work on the dynamics of a test particle moving in the same plane as a massive planet in a circular orbit around a much heavier star, a system known as the restricted circular planar three-body problem. The Lagrange points are well-known fixed points for low-eccentricity test particles in such a system. Associated with the two stable Lagrange points are families of orbits known as "tadpoles" and "horseshoes." The Trojan asteroids, ∼1700 objects in two groups which lead and trail Jupiter in its orbit, are examples of objects in tadpole orbits. While these standard Lagrange points, tadpoles, and horseshoes correspond to low-eccentricity orbits, we found an infinite number of Lagrange point analogues and tadpole and horseshoe analogues that are associated with test particles in highly eccentric long-period orbits. These analogues resulted from a framework we developed for the evolution of high-eccentricity long-period test particle orbits and used to explore mean-motion resonances between a particle and the massive bodies.

Though this work is quite mathematical, it has led to results of considerable physical interest. Determination of the resonance widths gave a condition for the onset of chaos at large semimajor axis — the analogue to the Wisdom (1980) criterion for chaos for particles in nearly circular orbits close to the planet. These explorations also produced 1) a redefinition of resonance orders for the high-eccentricity regime in which a $p : p + q$ resonance is called "pth order" instead of the usual "qth order" to reflect the importance of interactions at periapse; and 2) a simple explanation for the presence of "asymmetric librations" in exterior $1 : N$ resonances and the absence of these librations in other exterior resonances.

Our framework for high-eccentricity particles might be applied to the origins of long-period comets and the structure of Oort cloud. This population is believed to have formed from small bodies originally on roughly circular orbits within Neptune's orbit; these were kicked by the giant planets into very eccentric orbits ∼10,000 AU in size which were later circularized by bodies outside the solar system. One surprising

result of our work is that for sufficiently small planets (planet/star mass ratio $\mu < 5 \times 10^{-6}$), a test particle initially close to the planet cannot escape from the system.

1.1.2 The size spectrum of Kuiper belt objects

Chapter 3 investigates the size distribution of KBOs. Early observations of KBOs gave a power-law size distribution but were unable to probe KBO sizes below ∼100 km. However, the size distribution produced in the most recent KBO survey conducted by Bernstein et al. (2004) using the Hubble Space Telescope was a broken power law that became shallower for KBOs smaller than about 70 km in size. We explained these results by assuming that KBOs are gravity-dominated bodies with negligible material strength and are part of an equilibrium collisional cascade. Using a simple mass conservation argument, we derived the slope of the size distribution in the collisional cascade. The break location followed from this slope through a self-consistent calculation: while bodies smaller than the size at the break are effectively in collisional equilibrium, bodies larger than the break size have never undergone catastrophic collisions. The existence of this break, the break's location, and the power-law slope we expect below the break are consistent with the findings of Bernstein et al. (2004). The agreement with observations indicates that KBOs as small as ∼40 km are held together by self-gravity rather than material strength.

1.2 Relativistic shocks and self-similar solutions

Chapters 4 and 5 describe the physics of relativistic shocks passing through stellar envelopes, a topic relevant to energetic explosions such as gamma-ray bursts (GRBs) and supernovae. Over the last decade, studies of GRBs and supernovae have flourished. GRBs are flashes of γ-rays lasting between $\sim 10^{-3}$ and $\sim 10^{3}$ seconds that are often followed over several days by x-ray, ultraviolet, and optical radiation known as an afterglow. They occur at cosmological distances, are very energetic ($\sim 10^{51}$ ergs), and must involve extremely relativistic motion. Like some supernovae, GRBs are

believed to be associated with the deaths of massive stars. A physical understanding of these extreme phenomena would shed light on the process of stellar death.

Since these explosions are believed to deposit their energy in the stellar and/or circumstellar material via strong shocks, they have motivated much numerical and analytic work on the physics of shock propagation. While analytic work on shock propagation is confined to particular geometries and density profiles for which the calculations are tractable, analytic results often yield physical insight that enhances our understanding of numerical simulations. The investigations we present here give analytic descriptions of flows produced by shocks.

Because studies of shocks require solutions of the nonlinear partial differential hydrodynamic equations, much of the analytic work on strong shock propagation to date has focused on self-similar solutions of these equations. In these solutions, the profiles of the hydrodynamic variables have constant overall shapes whose time evolution consists simply of scalings in amplitude and position. This form of solution allows the simplification of the usual system of partial differential hydrodynamic equations to a system of ordinary differential equations. However, it can be applied only to systems that contain no natural scales. Fortunately, many stellar envelopes have polytropic profiles in which the pressure scales as a power law of the density. In the envelopes' outermost layers, where gravity can be assumed constant, the polytropic profiles imply that the density is a power-law function of the distance from the star's surface and, therefore, scale-free.

1.2.1 Shock breakout through polytropic stellar envelopes

When the engine producing a GRB or supernova explosion deposits $\sim 10^{51}$ ergs of thermal energy in the interior of a star, we expect a strong shock to be driven through the star's envelope. We investigated the case in which this shock accelerates to ultrarelativistic speeds in a star whose envelope has a polytrope-like density profile. When the shock is close to the star's outer boundary, its behavior follows the self-similar solution given by Sari (2006) for implosions in planar geometry. We used this

solution to find the asymptotic solution as the shock reaches the star's edge. We then showed that the motion after the shock breaks out of the star is described by a new self-similar solution remarkably like the solution for the motion inside the star. In particular, the characteristic Lorentz factor, pressure, and density vary with time according to the same power laws both before and after the shock breaks out of the star. After emergence from the star, however, the self-similar solution's characteristic position corresponds to a point behind the leading edge of the flow rather than at the shock front, and the relevant range of values for the similarity variable changes. Our numerical integrations agree well with the analytic results both before and after the shock reaches the star's edge.

1.2.2 Relativistic solutions with cold fluid temperatures

The energy and Lorentz factor of the ejecta in models of supernovae/GRBs are important because they constrain the amount of energy that can be deposited in the photons we observe from these explosions. Previous calculations of the final Lorentz factors in relativistic explosions have all been approximate: analytic results for the accelerating fluid flow apply only while the flow is hot and so do not account correctly for the period after the fluid cools to nonrelativistic temperatures, when the acceleration slows and stops. Here we present a new self-similar solution encompassing both hot and cold fluid in the flow produced when a relativistic shock breaks out of a star. The key ingredient in this new solution is to identify the characteristic position with the point where the fluid becomes cold—in other words, to realize that the transition between hot and cold fluid in the flow is self-similar. This is surprising since the cold fluid is not self-similar in the original solution for the post-breakout flow discussed in section 1.2.1. The new solution for the cooling fluid is valid at late times when the accelerating fluid's bulk kinetic Lorentz factors are large but when the thermal Lorentz factors of given fluid elements are not necessarily large.

Chapter 2

A generalization of the Lagrangian points: studies of resonance for highly eccentric orbits

Abstract

We develop a framework based on energy kicks for the evolution of high-eccentricity long-period orbits in the restricted circular planar three-body problem with Jacobi constant close to 3 and with secondary to primary mass ratio $\mu \ll 1$. We use this framework to explore mean-motion resonances between the test particle and the massive bodies. This approach leads to a redefinition of resonance orders for the high-eccentricity regime in which a $p : p + q$ resonance is called "pth order" instead of the usual "qth order" to reflect the importance of interactions at periapse. This approach also produces a pendulum-like equation describing the librations of resonance orbits about fixed points that correspond to periodic trajectories in the rotating frame. A striking analogy exists between these new fixed points and the Lagrangian points as well as between librations around the fixed points and the well-known tadpole and horseshoe orbits; we call the new fixed points the "generalized Lagrangian points." Finally, our approach gives a condition $a \sim \mu^{-2/5}$ for the onset of chaos at large semimajor axis a; a range $\mu < \sim 5 \times 10^{-6}$ in secondary mass for which a test particle initially close to the secondary cannot escape from the system, at least in the planar problem; and a simple explanation for the presence of asymmetric librations in exterior $1 : N$ resonances and the absence of these librations in other exterior

resonances.

2.1 Introduction

The three-body problem, or the dynamics of three masses due to their mutual gravitational influences, has a number of well-known special cases. One of these, the circular planar restricted case, requires that the primary and secondary bodies, m_1 and m_2, follow circular orbits about their common center of mass and that the third body be a massless test particle moving in the massive bodies' orbit plane. These conditions simplify the three-body problem enough to produce an integral of the motion: the Jacobi constant $C_J = -2(E - \Omega h)$ where E is the particle's energy[1], h is the particle's angular momentum, and Ω is the massive bodies' constant angular velocity.

Still, the circular planar restricted case has important applications to the dynamics of our solar system. Many of the orbits of major planets about the sun are nearly circular and are roughly confined to a plane; the same goes for many of the orbits of large moons about their planets. Common examples of applications for the circular planar restricted case include the effects of Jupiter on the asteroid belt; of Neptune on the Kuiper belt; of moons on planetary rings; and of giant planets on comets.

This paper describes a study of this problem in the regime where $m_2 \ll m_1$, the test particle's eccentricity is large, and the Jacobi constant is greater than but close to 3 in the standard system of units where $G = 1$, the primary-secondary separation is 1, $1 = m_1 + m_2 \simeq m_1$, and, therefore, $\Omega = 1$. Since values of C_J near 3 correspond to test particles on circular orbits close to the secondary, this special regime includes particles originally in circular orbits around a star close enough to a planet for the planet to perturb them into very eccentric orbits. Our interest in this regime arises from an intent to investigate the paths through which small particles are perturbed by a planet until they escape or are captured. This problem was studied by Ford et al. (2001) and Rasio & Ford (1996) via numerical simulations of three massive bodies in

[1]We refer to the test particle as "the particle" and to its energy per unit mass and angular momentum per unit mass (in the limit of a massless test particle) as its "energy" and "angular momentum."

three dimensions. Due to this motivation we use "star" and "planet" to refer to the primary and secondary in the remainder of this paper.

In §2.2 we derive to first order in $\mu = m_2/(m_1 + m_2) = m_2$ the energy kick received by a particle in a highly eccentric orbit with semimajor axis $a \gg 1$ at each periapse passage. We show that since the interaction is localized at periapse, this energy kick is essentially independent of a and depends only on the periapse distance and the azimuth difference between the planet and particle at periapse. In §2.3, §2.4, and §2.5 we use these energy kicks to find "fixed" particle orbits and describe motion near them. These "fixed" orbits are located at planet-particle mean-motion resonances. When observed stroboscopically at periapse only, they appear as fixed points just like the well-known Lagrangian points. We use both a continuous approximation and a discrete mapping in a derivation of the particle's motion around resonances, the resonance widths, and the libration periods. When these librations are observed stroboscopically, they likewise become analogies of the well-known tadpole and horseshoe orbits. In §2.6 we discuss types of chaos for large-eccentricity orbits, and in §2.7 we summarize and discuss our findings.

2.2 Energy kick to first order in μ

Let ΔE be the change in the particle's energy between its consecutive apoapse passages. In our units, where the angular velocity of the star-planet is set to unity, the change in angular momentum is also ΔE [2]. Therefore, it can be calculated by integrating the torque exerted on the particle:

$$\Delta E = \int -\left.\frac{\partial V}{\partial f}\right|_r dt \tag{2.1}$$

where V is the gravitational potential produced by the planet and star and f is the particle's azimuth in inertial space.

[2]Since the angular momentum is always perpendicular to the orbit plane, only one of its components is nonzero. We therefore treat the torque and the change in angular momentum as scalars equal to the components of the vector torque and the vector change in angular momentum, which are perpendicular to the orbit plane.

To begin with, we estimate the energy kicks to first order in μ. We express ΔE as $\Delta E = \mu \Delta E^1 + \mathcal{O}(\mu^2)$. To evaluate ΔE^1 we calculate the torque assuming that the particle moves on a Keplerian trajectory around the star, with its focus at the center of mass. The effect of the deviation of the trajectory from that description on ΔE is of order μ^2 or higher.

Since we are considering only the time elapsed between two consecutive apoapses, we choose coordinates such that the time $t = 0$ when the particle is at periapse and the direction of periapse is along the positive x-axis. The planet and star are in uniform circular motion, so we can write $V = V(\theta, r)$ where θ is the angle between the planet and the particle and r is the particle's distance from the origin. This gives

$$\Delta E = \int \left. \frac{\partial V}{\partial \theta} \right|_r dt \quad . \tag{2.2}$$

V is given explicitly by

$$V = V_{\text{planet}} + V_{\text{star}} = -\frac{\mu}{|\vec{r} - \vec{r}_{\text{planet}}|} - \frac{1}{|\vec{r} - \vec{r}_{\text{star}}|} \quad ; \tag{2.3}$$

to first order in μ, this gives

$$V = -\frac{1}{r} - \mu \left(\frac{1}{(r^2 + 1 - 2r\cos\theta)^{1/2}} - \frac{\cos\theta}{r^2} \right) \quad . \tag{2.4}$$

Let ϕ be the angle between the planet and the particle at periapse[3], so that $\theta = \phi + t - f$. Then the derivative with respect to θ at fixed r that appears in Eq. (2.2) can be replaced by a derivative with respect to ϕ. To first order in μ the particle trajectory $r(t)$ can be assumed fixed and independent of ϕ, so we can move the ϕ derivative outside the integral of Eq. (2.2). Using the first-order expression for V we get

$$\Delta E^1 = -\frac{dU^1}{d\phi} \tag{2.5}$$

[3]Thus defined, ϕ is the usual resonant argument measured at periapse only.

where the effective potential U^1 is given by

$$U^1 = \int \left[\frac{1}{\sqrt{r^2+1-2r\cos\theta}} - \frac{1}{\sqrt{r^2+1+2r\cos(t-f)}} - \frac{\cos\theta+\cos(t-f)}{r^2} \right] dt \quad . \tag{2.6}$$

The integral is performed over one Keplerian orbit of the particle.

In this expression for U^1, the first term in the brackets is the "direct" term; it represents the planet's contribution. The second term does not contribute to ΔE^1; it keeps U^1 from diverging when $a \to \infty$ and is obtained from the first term by substituting $\phi = \pi$. The third term is the "indirect" term; it represents interactions with the star. ΔE^1 and its effective potential U^1 are functions of μ, ϕ, and the particle trajectory shape, which determines r and f as a function of t. Note that up to a constant, the effective potential U^1 is simply the time-integrated potential over the trajectory of the particle.

When the apoapse distance $a(1+e)$ is much larger than both 1 and the periapse distance $r_p = a(1-e)$, the perturbing effects of the star and planet on the particle near periapse dominate over perturbing effects on the particle elsewhere in its orbit. In this regime, the entire energy kick ΔE occurring between consecutive apoapse passages can be thought of as a discrete event associated with a particular periapse passage. In the limit as a diverges due to energy kicks but C_J remains constant, $e \to 1$, r_p approaches a constant, and except near apoapse the entire trajectory approaches a parabola independent of a: $a \to \infty$. If the particle is outside the planet's Hill sphere,

$$\lim_{a\to\infty} r_p = \lim_{a\to\infty} \left[-\frac{1}{2}\left(C_J + \frac{1}{a}\right) \frac{1}{\sqrt{1+e}} \right]^2 = \frac{C_J^2}{8} \tag{2.7}$$

$$r = 2r_p/(1+\cos f) \tag{2.8}$$

$$\frac{df}{dt} = \frac{(1+\cos f)^2}{(2r_p)^{3/2}} \tag{2.9}$$

$$t = (2r_p)^{3/2} \cdot \frac{1}{6} \tan\frac{f}{2}\left(3 + \tan^2\frac{f}{2}\right) \quad . \tag{2.10}$$

For particles that start close to the orbit of the planet, the periapse distance is

therefore $r_p = 9/8$.

Given this asymptotic form for the orbit, we can calculate the asymptotic forms of $U^1(a, e, \phi) \to U^1(r_p, \phi)$ and $\Delta E^1(a, e, \phi) \to \Delta E^1(r_p, \phi)$ in the large-a limit. For $C_J = 3$, the computed values of U^1 and its derivative ΔE^1 as a function of ϕ are shown in Figures 2.1 and 2.2. Near $\phi = 0$, ΔE^1 is dominated by the direct particle-planet interaction because the minimum planet-particle distance is much less than the star-particle distance. When $\phi = 0$, $\Delta E^1 = 0$ because of symmetry. When $\phi < 0$ but $|\phi| \ll 1$, the planet lags the particle for most of the time the particle spends near periapse, so $\Delta E^1 < 0$. Similarly, when $\phi > 0$ and $|\phi| \ll 1$, $\Delta E^1 > 0$.

When $||\phi| - \pi| \ll 1$, the indirect contribution $\Delta E^1_{\rm ind}$ due to the star's reflex motion dominates because the star passes closer to the particle. From the ϕ-dependent part of star's contribution to the integral in Eq. (2.6), $\Delta E^1_{\rm ind}$ is a sinusoidal function of ϕ:

$$\frac{\partial}{\partial \phi} \int_{-\infty}^{\infty} \frac{\cos\theta}{r^2}\, dt = -\frac{\sin\phi}{\sqrt{2r_p}} \int_{-\pi}^{\pi} \cos(t - f)\, df \simeq -2.0 \sin\phi \tag{2.11}$$

where in the last step we use $r_p = 9/8$ as an example in evaluating the coefficient.

The integral in Eq. (2.11) seems to suggest that star-particle interactions over all intervals in f should contribute significantly to $\Delta E^1_{\rm ind}$. However, as Eq. (2.10) shows, $|t|$ increases much faster than $|f|$ as $|f|$ approaches π. As a result, oscillations in $\cos(t - f)$ kill contributions to the integral at $|f|$ near π, and the star-particle interaction is important only near periapse.

We can also get the total contribution of terms that are second order or above in μ: this is just the difference between values of ΔE found by numerical integration of the equations of motion and values of $\mu \Delta E^1$ given by Eq. (2.6) (see Figure 2.1).

2.3 First-order resonances

Resonances occur when the particle completes p orbits in exactly the time needed for the planet to complete $p + q$ orbits for some integers p, q. This situation is known as a $p : p + q$ resonance. In the standard treatment of these resonances,

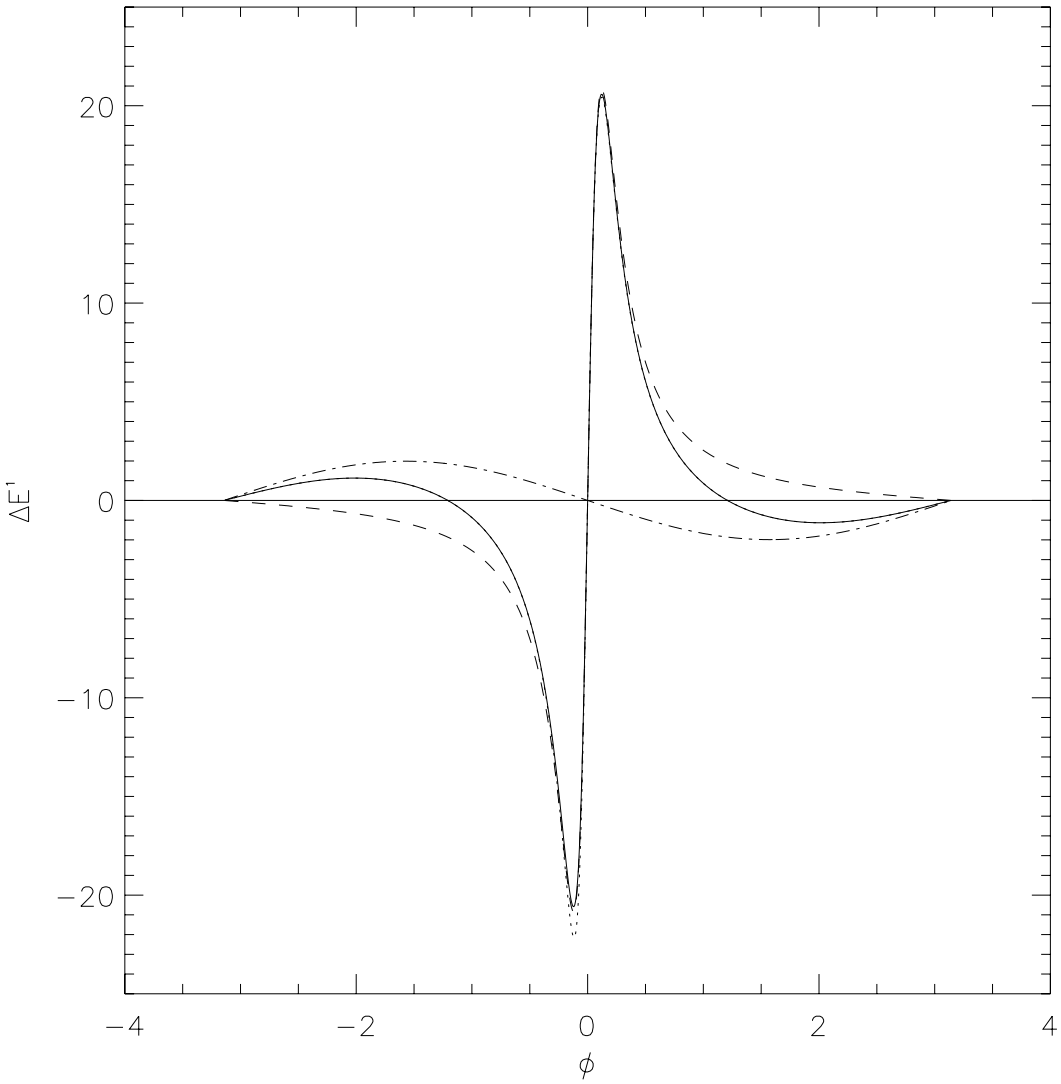

Figure 2.1: First-order energy kick ΔE^1 in the large-a regime (solid line) with $C_J = 3$ computed using Eqs. (2.5) and (2.6). The dotted line is the energy kick $\Delta E/\mu$ calculated using Eqs. (2.2) and (2.3) for a $\mu = 10^{-3}$, $C_J = 3$ parabolic orbit with all higher-order terms included. For this μ, the first-order term clearly dominates for all values of ϕ; higher-order effects in μ are visible only near $\phi = -0.12$. The dashed line is the planet's direct contribution to ΔE^1 using Eq. (2.5) and Eq. (2.6) with the third term dropped; the dash-dotted line is the indirect contribution to ΔE^1 from the star's reflex motion calculated using Eq. (2.5) and Eq. (2.6) with the third term only.

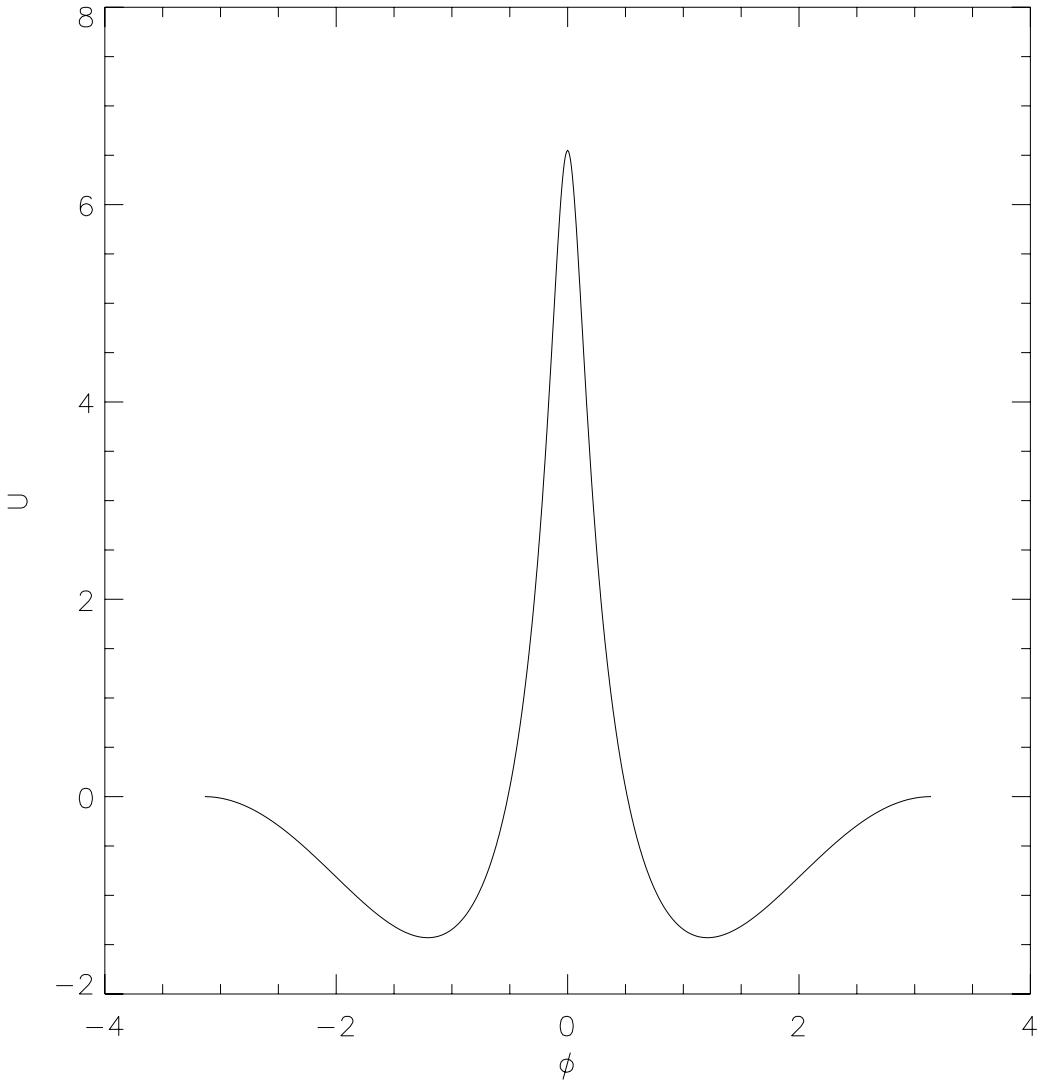

Figure 2.2: Potential U^1 in the large-a regime (heavy solid line) with $C_J = 3$ computed using Eq. (2.6). For comparison we also show U^1 for $C_J = 3$ elliptical orbits with finite a. For later reference we chose as examples orbits corresponding to mean-motion resonances. The dotted line is U^1 for $a \simeq 2.5$ (1:4 resonance); the dashed line corresponds to $a \simeq 4.6$ (1:10 resonance); and the lighter solid line corresponds to a $a \simeq 10.1$ (1:32 resonance). Though these curves show some quantitative differences due to changes in the orbit shape, they and particularly the shapes of their potential wells are qualitatively similar.

both orbits in question are usually nearly circular and a significant interaction occurs every time the bodies are at conjunction, i.e., whenever their azimuths coincide. This happens once every resonant cycle if $q = 1$, so $q = 1$ resonances are usually termed "first-order" resonances. During a conjunction between a test particle and planet in orbits with low eccentricity $e \ll 1$, the torque exerted on the particle while the particle precedes the planet almost cancels the torque exerted while the particle lags the planet; the residual is of order e. When $q > 1$, q conjunctions occur during each resonant cycle. Because they occur in different positions in inertial space, their effects tend to cancel each other, leaving a residual torque of order e^q. Since the interaction strength decreases exponentially with increasing q as e^q, resonances in the standard treatment are usually classified by q value. Accordingly, a $p : p+q$ resonance is called a "qth-orde'r' resonance regardless of the value of p.

However, the high eccentricities of orbits in the large-a regime discussed here make the standard definition of resonance order meaningless. Since $e \to 1$, resonances of different order under the standard definition have comparable significance because $e^q \simeq 1$. Also, encounters at periapse are physically far more important than conjunctions at other points in the particle's orbit. We therefore redefine the "orders of resonance" to focus on interactions at periapse. If the planet completes an integer number of orbits in the time it takes the particle to orbit exactly once, then we say the particle is in a "first-order" resonance. In general, we say the particle is in an "pth-order" resonance if the planet completes an integer number of orbits in the time it takes the particle to orbit p times: then there are p interactions within one resonant cycle. In terms of the standard resonance treatment, we say a $p : p + q$ resonance in the large-a regime is "pth-order" regardless of the value of q. In both the large- and small-eccentricity cases, the order of the resonance is given by the number of significant interactions within a single resonant cycle.

In the following we show that this revised definition does indeed make sense. We calculate the widths of resonances of various orders in the large-a limit and show that with this new definition, their widths decay exponentially with the order of the resonance. We discuss in detail the first-order or $1 : N$ resonances and begin

by making a 'continuous approximation' to the action of the discrete energy kicks discussed in §2.2.

According to the new definition of resonance orders, ϕ should be constant in time if we consider a particle exactly at a first-order resonance of semimajor axis $a_{\rm res}$ and if we ignore the effects of energy kicks. A particle close to resonance with, say, semimajor axis $a = a_{\rm res} + \Delta a$ should drift in ϕ over time at a constant rate, again ignoring energy kicks. The amount of drift per orbit of the test particle is just the difference between its orbital period $2\pi a^{3/2}$ and the resonant one $2\pi a_{\rm res}^{3/2}$. We can express this drift as

$$\frac{d\phi}{dt} = \frac{3}{2}\frac{\Delta a}{a} \quad . \tag{2.12}$$

The differential is a good approximation assuming $\Delta a \ll a^{-1/2}$ so that many particle orbits must elapse before ϕ changes by an angle of order π. We refer to this differential form as the continuous approximation.

Energy kicks cause the semimajor axis to evolve in time. To first order in μ we have

$$\frac{d(\Delta a)}{dt} = \frac{1}{\pi}a^{1/2}\frac{dE}{dn} = -\frac{1}{\pi}a^{1/2}\mu\frac{dU^1}{d\phi} \quad . \tag{2.13}$$

To justify the differentials here we require that μ be small enough for the change in Δa due to a single kick to be much less than the typical Δa. We differentiate Eq. (2.12) and substitute Eq. (2.13) to get

$$\frac{d^2\phi}{dt^2} = -\frac{3}{2\pi}a^{-1/2}\mu\frac{dU^1}{d\phi} \quad . \tag{2.14}$$

This shows that ϕ simply evolves as a particle moving in the potential $U^1(\phi)$.

2.3.1 Generalized Lagrangian points

Since U^1 has four extrema[4] at the four zeroes of ΔE^1, there are four fixed points in ϕ. According to Eqs. (2.13) and (2.12), these fixed points in ϕ are also fixed points in a with $\Delta a = 0$. Then each particle trajectory corresponding to one of these fixed points must be a resonance trajectory whose periapse direction is constant with respect to the planet's position. These fixed points therefore represent periodic orbits of the particle in the planet's rotating frame and in the inertial frame[5].

Of the four fixed points, two are unstable since they correspond to maxima of the potential $\theta = 0, \pi$. The other two are stable since they correspond to potential minima at $\theta = \pm 1.21$. The existence of two extrema at $\theta = 0, \pi$ is guaranteed by symmetry arguments. The two additional extrema at $\phi = \pm 1.21$ occur where the energy kicks from the planet and star cancel each other exactly. These extrema therefore appear only when the indirect term—or, equivalently, the star's motion—is taken into account.

This discussion suggests an analogy between the five well-known Lagrangian points and the new fixed points. The two stable points correspond to the stable Lagrangian points L_4 and L_5, which also appear only when the motion of the star, i.e., the indirect term, is taken into account. The unstable fixed point at $\phi = \pi$ is the analogue of L_3; the one at $\phi = 0$ corresponds to L_1 and L_2, which merge in this generalization. For a given resonance $1 : N$, $N = a^{3/2}$, we therefore denote the fixed points by L_{12}^N, L_3^N, L_4^N, and L_5^N. The positions of these new fixed points in comparison to their standard Lagrangian counterparts is summarized in Table 2.3.1.

[4]These extrema are shown in Figure 2.2 for $C_J = 3$. Since, given a value for C_J, we can use Eq. 2.6 to set bounds on U^1 and its derivatives with respect to ϕ, we can check that, at least for $C_J = 3$, U_1 has no other extrema. We have done this for several C_J in the regime we are considering: C_J close to but greater than 3. Physically, this is equivalent to saying that changes in the system over time and space are slow and smooth enough that sharp variations in U_1 do not occur.

[5]When higher-order terms in μ are included, the shape of ΔE^1 changes slightly (see Figure 2.1 for an example); this shifts the positions of the fixed points in ϕ. The positions of the fixed points in a also shift slightly away from resonance due to the effects of precession. With the higher-order terms, then, the particle trajectories corresponding to the fixed points remain periodic in the rotating frame but become aperiodic in the inertial frame.

	Lagrangian Points	Generalized Lagrangian Points			
resonant index	$(N=1)$	$N=2$	$N=3$	$N=4$	large a
semimajor axis	1	$2^{2/3}$	$3^{2/3}$	$4^{2/3}$	$a=N^{2/3}$
physical meaning of fixed points	particle is *stationary* in rotating frame	particle moves on *periodic orbit* in rotating frame			
definition of angular variable	azimuth of particle in the rotating frame	azimuth of particle in rotating frame when it is at periapse			
L_1 & L_2	$\phi_1=0$, $\phi_2=0$	single point L_{12}^N with $\phi_{12}=0$			
L_3	$\phi_3=\pi$	$\phi_3=\pi$			
L_4 & L_5 $(\phi_5=-\phi_4)$	$\phi_4=\pi/3\simeq 1.04$	$\phi_4^2=1.196$	$\phi_4^3=1.196$	$\phi_4^4=1.198$	$\phi_4=1.21$
min. tadpole period	$\frac{4\pi}{3\sqrt{3}}\mu^{-1/2}\simeq 2.42\mu^{-1/2}$	$4.4\mu^{-1/2}$	$5.1\mu^{-1/2}$	$5.5\mu^{-1/2}$	$5.0a^{1/4}\mu^{-1/2}$
$\Delta a_{\max}$ tadpole	$\sqrt{8/3}\mu^{1/2}\simeq 1.63\mu^{1/2}$	$1.4\mu^{1/2}$	$1.6\mu^{1/2}$	$1.8\mu^{1/2}$	$0.78a^{3/4}\mu^{1/2}$
$\Delta a_{\max}$ horseshoe	$2(3)^{1/6}\mu^{1/3}\simeq 2.40\mu^{1/3}$	$4.6\mu^{1/2}$	$4.7\mu^{1/2}$	$5.0\mu^{1/2}$	$1.8a^{3/4}\mu^{1/2}$

Table 2.1: Comparison of generalized and standard Lagrangian points. All quantities are given to lowest order in μ. In particular, expressions for the $N=2,3,4$ resonances were calculated using a potential computed to first order in μ at $a=N^{2/3}$ rather than in the large-a limit. The numerical values for the generalized Lagrangian points and orbits are given for $C_J=3$.

2.3.2 Generalized tadpoles

The analogy is more obvious when motion around the fixed points is investigated. Small-amplitude motion around the stable fixed points L_4^N and L_5^N can be approximated by expanding U^1 around its minimum. This results in a harmonic oscillator equation:

$$\frac{d^2\phi}{dt^2} = -\frac{3}{2\pi}a^{-1/2}\mu \left(\frac{d^2U^1}{d\phi^2}\right)\Bigg|_{\phi=\phi_{4,5}^N} (\phi - \phi_{\rm res}) \quad . \tag{2.15}$$

The small-amplitude libration period around either L_4^N or L_5^N is therefore given by

$$K = \frac{T_{\rm libration}}{2\pi a^{3/2}} = \left(\frac{3}{2\pi}\left.\frac{d^2U^1}{d\phi^2}\right|_{\phi=\phi_{4,5}^N}\right)^{-1/2} a^{-5/4}\mu^{-1/2} = 0.79a^{-5/4}\mu^{-1/2} \tag{2.16}$$

where in the last step we use $r_p = 9/8$ in the large-a limit to get $d^2U^1/d\phi^2 \simeq 3.3$ at $\phi = \phi_{4,5}$. Note that K gives the number of periapse crossings per libration period. In our units, where 2π is the period of the massive bodies, the libration period is then $2\pi a^{3/2}K$.

Since Eq. (2.14) describes motion under the influence of a fixed potential, we can write down the conservation of energy equation by multiplying Eq. (2.14) by $\frac{d\phi}{dt}$ and integrating with respect to t:

$$\frac{1}{2}\left(\frac{d\phi}{dt}\right)^2 + \frac{3}{2\pi}a^{-1/2}\mu U^1 = \text{constant} \quad . \tag{2.17}$$

The constant of integration is the 'energy' associated with the movement of the orbit in ϕ and a. Since the potential is finite, it can only support a finite particle 'speed' in libration around L_4^N or L_5^N. The 'speed' is directly related to the deviation of the semimajor axis from the resonance via Eq. (2.12), so the maximal width of these librations in a is given by

$$\Delta a_{\rm max} = \left(\frac{4}{3\pi}\right)^{1/2} \mu^{1/2}a^{3/4}[U^1(\pi) - U^1(\phi_4)]^{1/2} \simeq 0.78a^{3/4}\mu^{1/2} \quad . \tag{2.18}$$

These librations around the fixed points L_4^N or L_5^N are analogues of the well-known

tadpole orbits. Note that the maximal widths of both the standard and generalized tadpole orbits scale as $\mu^{1/2}$ (see Table 2.3.1). The similarity is more apparent if we treat the (a, ϕ) parameters, which describe the orbit of the particle, as polar coordinates as shown in Figure 2.3. Seen in this way, (a, ϕ) are analogous but not identical to the polar coordinates of the particle in the rotating frame: a is the semimajor axis, not the radius, and ϕ is the azimuth of the test particle in the rotating frame only at periapse passage. Then the fundamental difference between the (a, ϕ) plane and the rotating frame is that while generalized Lagrangian points and the motion around them exist in a surface of section made up of discrete points representing periapse passages, the standard rotating frame with the standard Lagrangian points is made up of continuous trajectories. Therefore, while the standard Lagrangian points are fixed points in the rotating frame, the generalized points represent periodic orbits in that frame.

Since ϕ is equivalent to the usual resonant argument measured at periapse only, and since the drift in ϕ is assumed to be slow, librations in ϕ about ϕ_4^N or ϕ_5^N are equivalent to librations of the resonant angle about ϕ_4^N or ϕ_5^N. Then the generalized tadpoles are equivalent to 'asymmetric librations'—trajectories whose resonant arguments librate about a value other than 0 or π. In this context, L_4^N and L_5^N correspond to 'asymmetric periodic orbits' whose resonant argument is constant but not equal to 0 or π. Our discussion above gives a simple physical argument for the existence of asymmetric librations in all stable $1 : N$ exterior resonances. Again, note that the existence of these asymmetric librations and asymmetric periodic orbits follows from analysis of U^1 only when both the direct and indirect terms are accounted for.

2.3.3 Generalized horseshoes

As the energy of the particle moving under the U^1 potential increases beyond that of the maximal tadpole orbit, it overcomes the lower potential barrier at $\phi = \pi$. As long as its energy is still below the higher barrier at $\phi = 0$, the particle will librate around both the L_4^N and L_5^N points, avoiding only a narrow range in ϕ around $\phi = 0$. These

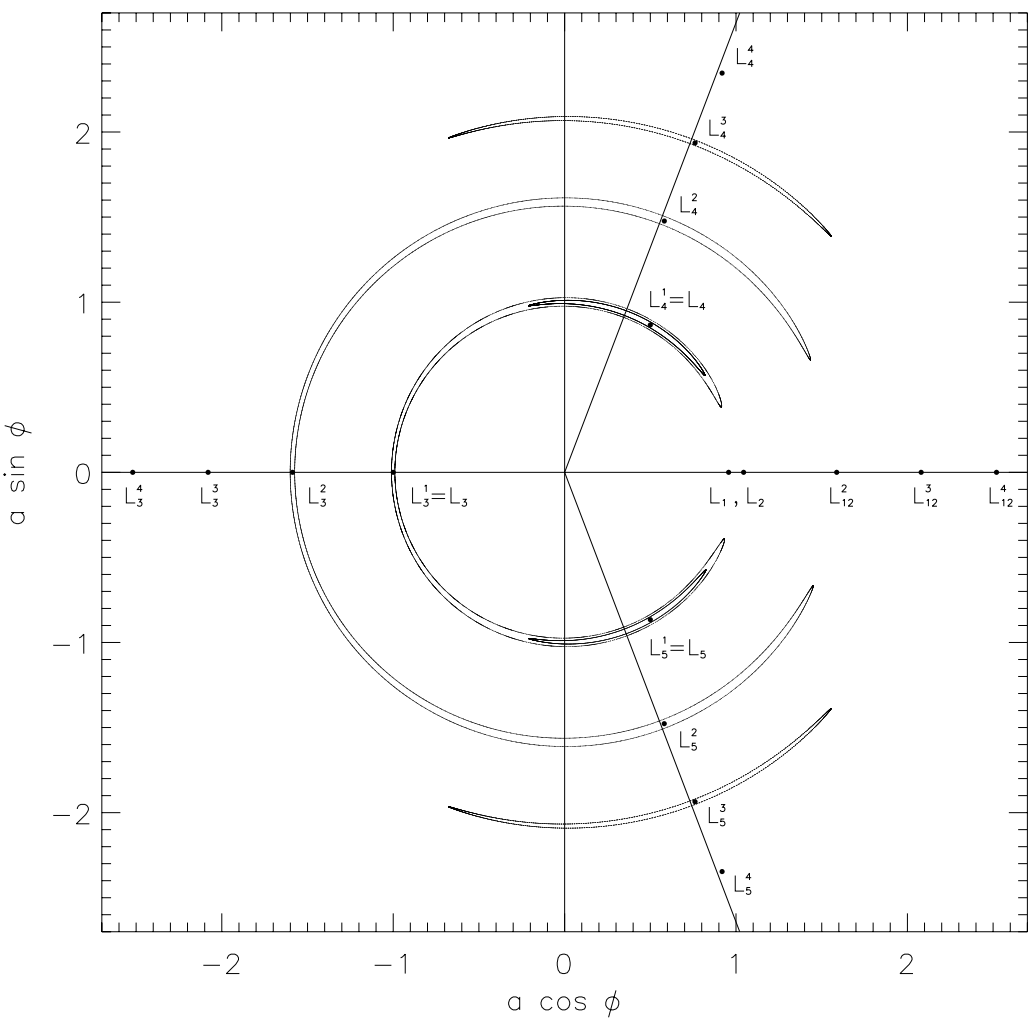

Figure 2.3: The Lagrangian point analogues L_i^N for $N = 1, 2, 3, 4$ with generalized horseshoes and tadpoles. The diagonal lines trace the azimuths of $L_{4,5}^{\infty}$—that is, the ϕ values of the minima in U^1. The horseshoes and tadpoles shown were calculated with $\mu = 2.5 \times 10^{-4}$ via full numerical integration of the circular planar restricted three-body problem. The L_i^N, the diagonal lines, and the 'horseshoes' and 'tadpoles' all have $C_J = 3$.

trajectories are the generalized horseshoe orbits. Using the same method as we used for the tadpoles, we calculate their widths in the continuous approximation to be

$$\Delta a_{\max} = \left(\frac{4}{3\pi}\right)^{1/2} \mu^{1/2} a^{3/4} [U^1(0) - U^1(\phi_4)]^{1/2} = 1.8 a^{3/4} \mu^{1/2} \quad . \tag{2.19}$$

The width of the maximal standard horseshoe does not follow this $\mu^{1/2}$ pattern, since the standard horseshoe case differs qualitatively from its generalized version. For the standard horseshoe, the angular momentum change is concentrated near the horseshoe's two ends. The close approach of the particle to the planet there increases the strength of the interaction beyond μ. As a result, the width of the horseshoe scales as $\mu^{1/3}$ rather than $\mu^{1/2}$. For a generalized horseshoe, the librating particle never gets closer to the planet than $r_p - 1$.

In Figures 2.4 and 2.5 we show libration around $L^4_{4,5}$ and $L^{10}_{4,5}$. In order to focus on the motion close to these points we plot a and ϕ as Cartesian rather than polar coordinates. In these plots, the librations in the surfaces of section appear to be 'warped' when compared to the continuous approximations calculated using the pendulum-like Eq. (2.14). This 'warping' is due to the discrete nature of the motion in the surfaces of section. As a trajectory moves from $\Delta a = 0$ toward larger positive Δa values, for example, the energy kicks stay positive and Δa should keep increasing until the trajectory reaches a ϕ value corresponding to a zero in the ΔE^1 versus ϕ curve. Within the continuous approximation, we expect the trajectory to begin moving back toward $\Delta a = 0$ at exactly this ϕ because ΔE^1 changes sign. A discrete trajectory will 'overshoot' the nominal ϕ where $\Delta E^1 = 0$ since a positive energy kick will carry the trajectory past this ϕ before the first negative kick is applied. As a result, the libration trajectories in the surfaces of section tend to become warped in the direction in which orbits move when librating. A quantitative discussion of this feature is given in the next section.

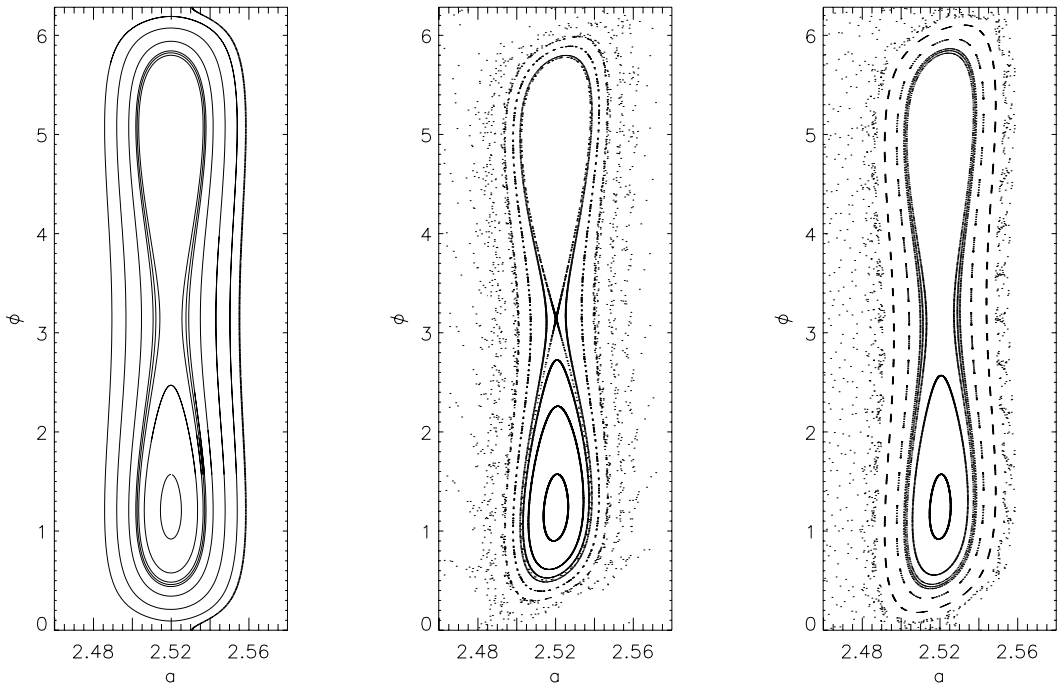

Figure 2.4: a vs. ϕ plot for $N = 4$, $\mu = 10^{-4}$, $C_J = 3$. We use $[0, 2\pi]$ as the range in ϕ to show the trajectories more clearly. The left-hand plot contains trajectories computed under the continuous approximation. The middle plot contains a surface of section computed via full numerical integration of the circular planar restricted three-body problem. The right-hand plot contains trajectories computed via the eccentric mapping discussed in §2.4. The same initial conditions were used for the trajectories in all three plots. The continuous approximation plot lacks the chaotic behavior evident in the numerical integration and eccentric mapping plots. Trajectories in the mapping plot differ from the numerical integration plot mostly because they were calculated with U^1, the potential in the large-a limit. Note that the separatrix trajectory in the middle plot is chaotic but on a scale too small to see in this figure (see Figure 2.9).

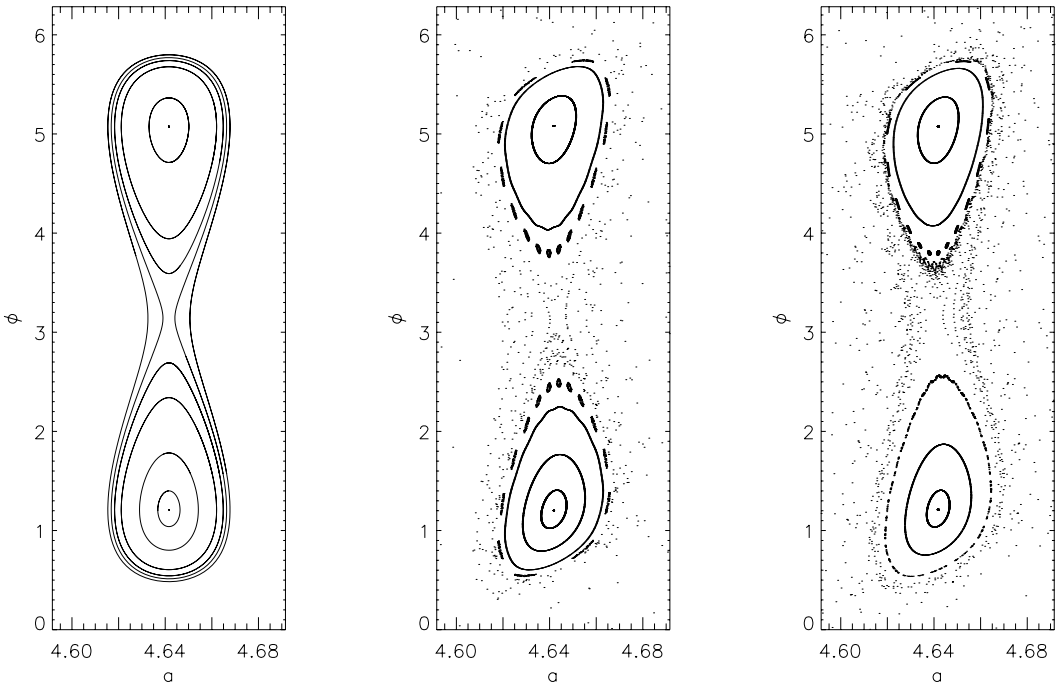

Figure 2.5: Same as Figure 2.4 but for $N = 10$. For this larger N, the resonances are wider. So the resonance overlap is more severe for the outer edges of the $N = 10$ resonance than for the $N = 4$ one. This causes the destruction of all horseshoe orbits and the distortion of the tadpoles relative to those computed in the continuous approximation.

2.4 The eccentric mapping

The 'warping' noted above suggests that the discrete nature of the surface of section is essential to understanding some feature of the motion in the (a, ϕ) plane. To study this, we define a mapping from the (a, ϕ) plane to itself. Beginning at an arbitrary point, this mapping produces an infinite series $(a^{(i)}, \phi^{(i)})$ of points visited by the test particle in the (a, ϕ) plane. Except perhaps in the few lowest-N resonances, we can build an excellent approximation to the correct mapping by applying the first-order kicks in the large-a limit:

$$-\frac{1}{2a^{(i+1)}} = -\frac{1}{2a^{(i)}} + \mu \Delta E^1(\phi^{(i)}) \tag{2.20}$$

$$\phi^{(i+1)} = \phi^{(i)} + 2\pi (a^{(i+1)})^{3/2} \tag{2.21}$$

where the new value of ϕ is calculated modulo 2π, i.e., brought back into the interval $(-\pi, \pi)$ by adding an integer multiple of 2π. Note that the a-value used to find $\phi^{(i+1)}$ itself has index $i + 1$; physically, this corresponds to the large-a limit assumption that each energy kick is a discrete event associated with a given periapse passage. Applying this mapping for several initial values in the (a, ϕ) plane results in the right panels of Figures 2.4 and 2.5. The close resemblance between trajectories generated with the mapping and with numerical orbit integrations demonstrate this mapping's accuracy.

It turns out that the warping of the small amplitude tadpoles can be understood completely in terms of the mapping. Close to the fixed points L_4^N and L_5^N, we define $\Delta a^{(i)} = a^{(i)} - a_{res}$ and $\Delta \phi^{(i)} = \phi^{(i)} - \theta_{res}$ so that the mapping becomes

$$\Delta a^{(i+1)} = \Delta a^{(i)} - 2a_{\rm res}^2 \mu \Delta \phi^{(i)} \left. \frac{d^2 U^1}{d\phi^2} \right|_{\phi = \phi_{4,5}^N} \tag{2.22}$$

$$\Delta \phi^{(i+1)} = \Delta \phi^{(i)} + 3\pi a_{\rm res}^{1/2} \Delta a^{(i+1)} \quad . \tag{2.23}$$

Since these are linear recursive equations, they can be solved analytically by standard techniques. We seek a solution of the form $(\Delta a^{(i)}, \Delta \phi^{(i)}) = (A, \Phi)\alpha^{(i)}$. Substituting

in the recursive equations, and seeking a non-trivial solution, we obtain

$$(\alpha - 1)^2 + 6\pi\mu a_{\rm res}^{5/2} \left.\frac{d^2U^1}{d\phi^2}\right|_{\phi=\phi_{4,5}^N} \alpha = 0 \quad . \tag{2.24}$$

Note that the dimensionless parameter in this equation is simply $(2\pi/K)^2$ where K is the number of periapse passages per libration in the continuous approximation as given by Eq. (2.16). If we denote the solutions as α_1 and α_2, it is clear from the above equation that their product $\alpha_1\alpha_2$ equals 1. Since we are interested in potential minima, $K^2 > 0$.

For $K \geq \pi$, the two roots are complex conjugates and each has unity norm. The fixed point is therefore an elliptical point in the discrete mapping as well as in the continuous approximation. The two values of α are given by

$$\alpha_{1,2} = 1 - 2(\pi/K)^2 \pm 2\sqrt{1-(\pi/K)^2}(\pi/K)i \quad . \tag{2.25}$$

The number of periapse passages per libration is given by

$$K^{\rm map} = \frac{2\pi}{\arg(\alpha)} = 2\pi \left[\arctan\left(\frac{2\sqrt{1-(\pi/K)^2}(\pi/K)}{1-2(\pi/K)^2}\right)\right]^{-1} \quad . \tag{2.26}$$

As $K \to \infty$, $K^{\rm map}/K \to 1$. This is expected since the continuous approximation is justified in this limit. Using the two values of α, we can find the eigenvectors:

$$(A, \Phi) = \left(\mu a_{\rm res}^2 \frac{d^2U^1}{d\phi^2}, (\pi/K)^2 \pm \sqrt{1-(\pi/K)^2}(\pi/K)i\right) \quad . \tag{2.27}$$

Since the eigenvectors determine the axes of the ellipses representing small librations about the fixed points, the similar shapes and orientations of the smallest librations in the middle and right-hand panels in each of Figures 2.4 and 2.5 confirm the eccentric mapping's accuracy.

For $a = 10^{2/3}$, $\mu = 10^{-4}$, the continuous approximation gives 11.6 orbits per tadpole libration (Eq. (2.16)). The eccentric mapping gives 11.4 orbits (Eq. (2.26)). This is close to the the 10.7 orbits per libration observed for very small librations

about the fixed points[6]. The negative power of a in Eq. (2.16) implies that as a increases, the number of periapse passages per tadpole libration period will decrease and the trajectory shapes will become increasingly warped.

In fact, when a grows so large that K falls below π, the tadpoles are destroyed. For $K < \pi$, the roots of Eq. (2.24) are real and distinct; therefore one of them is larger than unity. Then the fixed point is not stable despite being at a potential minimum. Our quantity K is closely related to the residue R discussed by Greene (1979): $R = 1 - (\pi/K)^2$.

The warping of the tadpoles which, at its extreme, leads to destruction of the resonances is absent in the continuous approximation. However, it can be understood as perturbations from nearby resonances. Interactions between neighboring first-order resonances should become large enough to destroy these resonances when the resonances begin to overlap. Eq. (2.19) implies that as a increases, the resonances widen in a while the distance between them decreases. Then we can find a condition on μ and a for resonance overlap by dividing half the distance between consecutive first order resonances by the width $\Delta a_{\max}$ of each resonance as given by equation (2.19). In the large-a limit, the distance between resonances is given by $\frac{2}{3}a^{-1/2}$ so we obtain

$$\frac{\text{resonance separation}}{2\Delta a_{\max}} = \left(\frac{\pi}{12}\right)^{1/2} a^{-5/4}\mu^{-1/2}[U^1(0) - U^1(\phi_4)]^{-1/2} = 0.18a^{-5/4}\mu^{-1/2} \quad . \tag{2.28}$$

This is proportional to K: in the large-a limit with $r_p = 9/8$, the right-hand side is $0.23K$ and first-order resonances overlap when $K < 4.5$. In this case, therefore, first-order resonances formally overlap before they are destroyed. Indeed, when $\mu = 10^{-3}$, stable first-order resonances are observed numerically to disappear for $a > \sim 4$. This agrees well with the $a > 4.0$ overlap criterion given by Eq. (2.28) with the left hand side set to 1 but is well below the $a > 5.25$ condition for resonance destruction given

[6]The largest tadpole libration shown in Figure 2.5 breaks into 14 islands. This is an example of the Poincaré-Birkhoff fixed-point theorem. It indicates that this tadpole's libration period is 14 orbits. This lengthening of the period is expected as the trajectory grows toward the separatrix passing through $\phi = \pi$.

by Eq. (2.31) or Eq. (2.16) with $K = \pi$.

2.5 Higher-order resonances

As defined in §2.2, higher-order resonances are the $p : p + q$ resonances with $p > 1$. These resonances are located at $a_{\rm res} = (N/p)^{2/3}$ where $N = p + q$ is an integer relatively prime to p. In analogy to our treatment of first-order resonances, we note that if we neglect energy kicks, a particle exactly at resonance should move in ϕ by 2π during each resonant cycle and by $2\pi q/p$ between consecutive periapse passages. The stationary points of this resonance should therefore occur at regular intervals of $2\pi/p$ in ϕ.

To study motion near but not at resonance, we include energy kicks. For a particle close to resonance, we can follow its trajectory by treating each resonant cycle as p applications of the eccentric mapping, one for each periapse passage in the cycle:

$$\begin{pmatrix} \Delta a^{(j+1)} \\ \Delta\phi^{(j+1)} \end{pmatrix} = \prod_{i=0}^{p-1} \begin{pmatrix} 1 & -2a_{\rm res}^2\mu \left.\frac{d^2U^1}{d\phi^2}\right|_{\phi=\phi_p^N+2\pi i/p} \\ 3\pi a_{\rm res}^{1/2} & 1 - 6\pi a_{\rm res}^{5/2}\mu \left.\frac{d^2U^1}{d\phi^2}\right|_{\phi=\phi_p^N+2\pi i/p} \end{pmatrix} \begin{pmatrix} \Delta a^{(j)} \\ \Delta\phi^{(j)} \end{pmatrix} \quad . \tag{2.29}$$

As before, $\Delta a^{(j)} = a^{(j)} - a_{\rm res}$ and $\Delta\phi^{(j)} = \phi^{(j)} - \phi_p^N$ where ϕ_p^N corresponds to the nearest fixed point in the resonance. The condition under which the linearization in $\frac{dU^1}{d\phi}$ is valid is now $\Delta a^{(j)} \ll a^{1/2}/p^2$ instead of $\Delta a^{(j)} \ll a^{1/2}$ because the number of energy kicks per resonant cycle is p instead of 1 and because the scale in ϕ over which the potential changes is now π/p instead of π. The condition under which linearization in μ is valid also changes because the largest term linear in μ that appears in the mapping matrix is $a_{\rm res}^{5/2}\mu\frac{d^2U^1}{d\phi^2}$. Though μ itself is small, cross-terms of order μ^2 and higher are now important unless $a_{\rm res}^{5/2}\mu\frac{d^2U^1}{d\phi^2} \ll 1$. This stronger condition is equivalent to $K \gg 1$, so the higher-order resonance treatment does not offer any simplifying advantages over the eccentric mapping discussed in §2.4 unless K is large.

Since $\Delta\phi$ changes very little between consecutive periapse passages in this $K \gg 1$ regime, we can use a variant of the continuous approximation where we neglect the

effects of drift in ϕ within a single resonant cycle. Then we can treat the particle's motion in terms of the net energy kick over an entire resonant cycle rather than a single particle orbit. The net energy kick is just the sum of p energy kicks spaced $2\pi/p$ apart in ϕ, so the particle appears to move in the potential

$$U_p^1 = \sum_{k=0}^{p-1} U^1(\phi - 2\pi k/p) \quad . \tag{2.30}$$

Note that effects of the star's reflex motion do not contribute to U_p^1 if $p > 1$: the indirect term in U^1 is exactly sinusoidal and the sum of p identical sine curves spaced $2\pi/p$ apart in phase is 0, so $U_{p,\mathrm{ind}}^1 = 0$. Since the part of U^1 due to the planet's direct contribution has just one maximum and one minimum at $\phi = 0, \pi$ respectively, U_p^1 has p identical maxima and minima (see Figure 2.6). Then a trajectory librating in one of the minima of U_n^1 should appear as a series of 'islands' spaced evenly in ϕ in the (a, ϕ) plane. As a result, no asymmetric librations are possible in higher-order resonances. Our result that, among exterior resonances, only $1 : N$ resonances show asymmetric librations is consistent with work done by Frangakis (1973). He analyzed expressions for the time-averaged direct and indirect terms of the disturbing function to find that asymmetric librations can exist only in $p : p+q$ resonances where $p = \pm 1$.

Because the p energy kicks received by the particle during each resonant cycle are spaced evenly by $2\pi/p$ in ϕ, we expect that the kicks will partially cancel over each resonant cycle and that this cancellation will improve exponentially as p increases. We therefore expect the amplitude of U_p^1 to decrease exponentially with p. As Figure 2.7 shows, this exponential decay is observed numerically: a best-fit line in log-log space gives amplitude $\propto 1.20^{-p}$.

2.6 Chaos in the large-a limit

We discuss just a few of the types and regions of chaos that arise when a is large. We first discuss 'global' chaos, which consists of chaotic regions that span a few resonance widths or more. We then give a few examples of 'local' chaos—chaos confined to

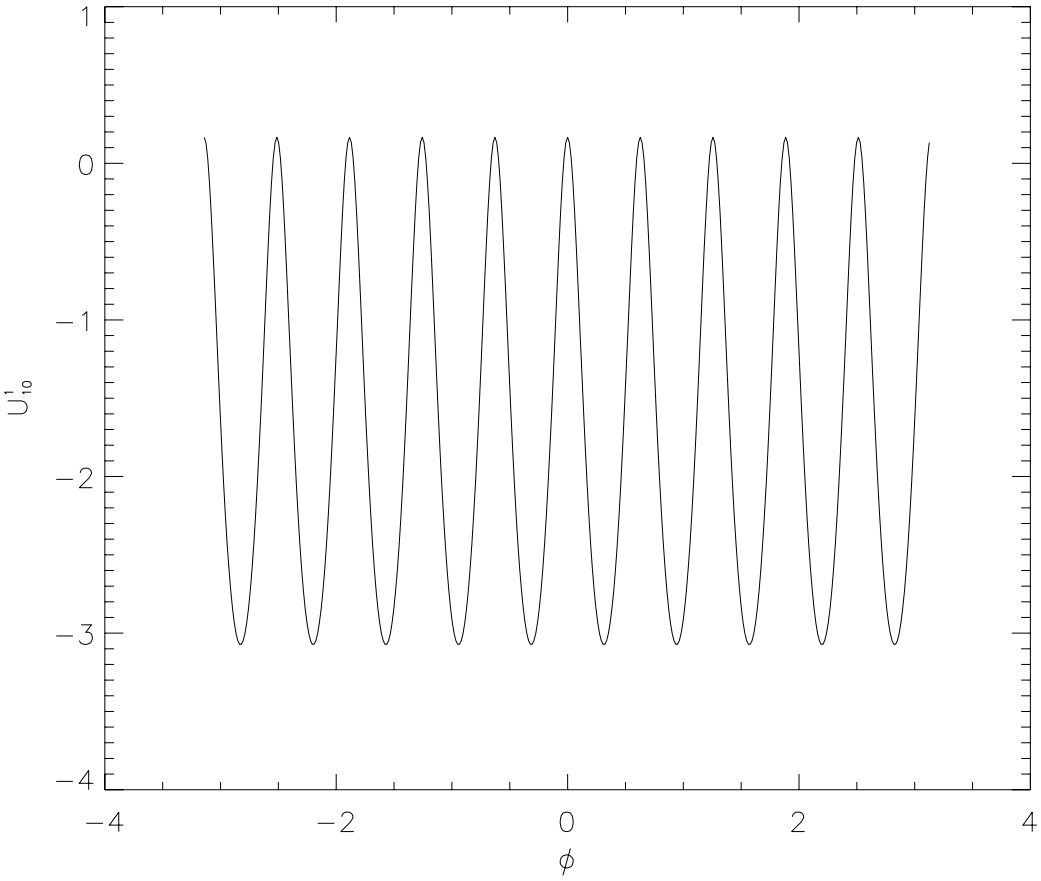

Figure 2.6: U^1_{10}, or U^1_p for a 10th-order resonance: U^1 summed over 10 consecutive periapse passages spaced evenly in ϕ. As before, $C_J = 3$.

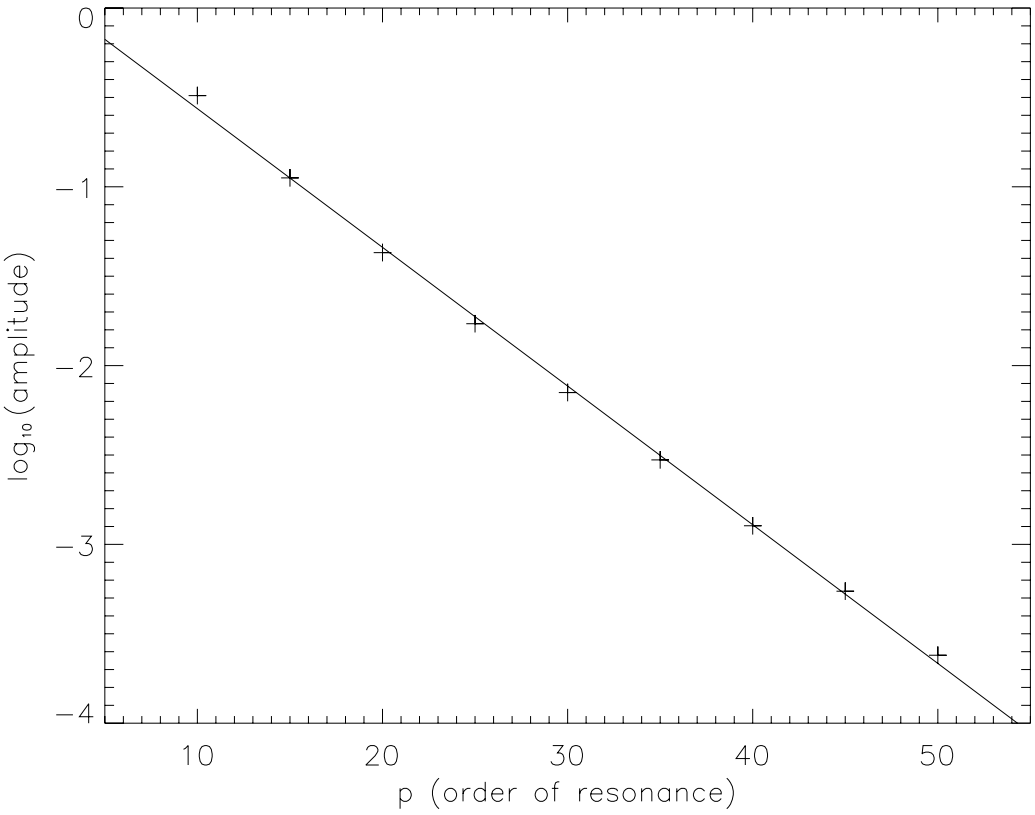

Figure 2.7: Amplitudes of U_p^1 plotted on a log scale as a function of p. Used $C_J = 3$. Best-fit line is $\log_{10}[\text{amplitude}] = -0.078p + 0.21$, or amplitude $\propto 1.2^{-p}$.

regions within a single resonance—and compare the structure seen in trajectories in the (a, ϕ) plane on local and global scales.

On large scales in a, chaotic regions arise where there is overlap between neighboring resonances or instability due to a small winding number as discussed in §2.4. In regions of the (a, ϕ) plane where first-order and/or higher-order resonances overlap even partially, we expect to see contiguous "globally" chaotic regions that span large ranges in a. Any remaining stable regions within resonances will appear as 'islands' of stable librations. Particles can undergo large changes in a only if they move in these chaotic regions, so such regions provide the only channels through which initially bound particles can escape from the star-planet system.

If a is large enough, K falls below π and these "islands" disappear as discussed in §2.4. For a given value of μ, we see from Eq. (2.16) that this occurs when

$$a > \mu^{-2/5} \left(\frac{3\pi}{2} \frac{d^2 U^1}{d\phi^2} \right)^{-2/5} = 0.33 \mu^{-2/5} \tag{2.31}$$

where, again, the numerical example corresponds to $r_p = 9/8$. The condition $K < \pi$ for resonance destruction in higher-order resonances does not follow simply from Eq. (2.28): effects of order μ^2 or higher may make the winding number expressions for higher-order resonances differ from the first-order resonance case in Eq. (2.16). However, numerical experiments suggest that the a at which higher-order resonances become unstable is comparable to but less than that given by Eq. (2.31).

If μ is small enough, there should be regions in a where the resonances do not overlap. In these regions we expect to see stable trajectories that circulate around the resonances instead of librating in them. We find numerically that stable circulating trajectories exist for μ values up to at least $\mu = 5 \times 10^{-6}$; an example is shown in Figure 2.8. Greene (1979) suggests that as μ increases, the last stable circulating trajectory should have semimajor axis a such that $a^{3/2}$ is the golden ratio $(1+\sqrt{5})/2$. Our situation differs qualitatively from Greene's in that our potential depends on its linear coordinate, the semimajor axis, while Greene's potential, which is given by the standard map, is independent of its linear coordinate r. Specifically, when a is not

much larger than 1, $r_p - 1 \ll 1$; this leads to a larger maximum energy kick and potential well depth than is expected for $r_p = 9/8$, so the resonances are wider and more prone to overlap for a given a close to 1 than we would expect in the large-a limit. However, as a increases the resonance spacing decreases as discussed in §2.4. These competing effects suggest that the last stable circulating trajectories—those which, in a sense, are 'farthest' from any resonances—should lie neither near $a = 1$ nor at $a \gg 1$. Also, effects of order μ^2 and higher that are present in our situation have no analogue in Greene's analysis of the standard map. So it is unsurprising that the last stable circulating trajectories that we found numerically have $a^{3/2}$ unrelated to $(1 + \sqrt{5})/2$.

Continuity and uniqueness imply that in a system with two degrees of freedom, stable trajectories in a two-dimensional surface of section cannot be crossed. In the planar restricted three-body problem, therefore, stable circulating trajectories divide the (a, ϕ) plane into separated regions in a. This implies that for any $\mu < 5 \times 10^{-6}$, chaotic and regular trajectories that start close enough to the planet are confined to a set range in a. Then the particles associated with these trajectories can never escape from the star-planet system.

This bounding of chaotic regions by stable trajectories also leads to confinement of chaos on very small scales in a. Regions of small-scale 'local' chaos arise from unstable fixed points that must be saddle points due to the area-preserving nature of the eccentric mapping; the separatrices associated with the saddle points are chaotic. If stable continuous trajectories exist near a saddle point, they act as boundaries to the chaotic separatrix. Prominent examples of these separatrices include those dividing tadpole and horseshoe analogue trajectories within individual first-order resonances. These regions are bounded by the largest stable tadpole and smallest stable horseshoe, so their maximum range in a is at most the resonance width. One of these is shown in Figure 2.9.

The existence of similar separatrices on all scales smaller than a single resonance width follows from the Poincaré-Birkhoff theorem, which states that for small enough μ, a trajectory with rational winding number K is associated with equal numbers of

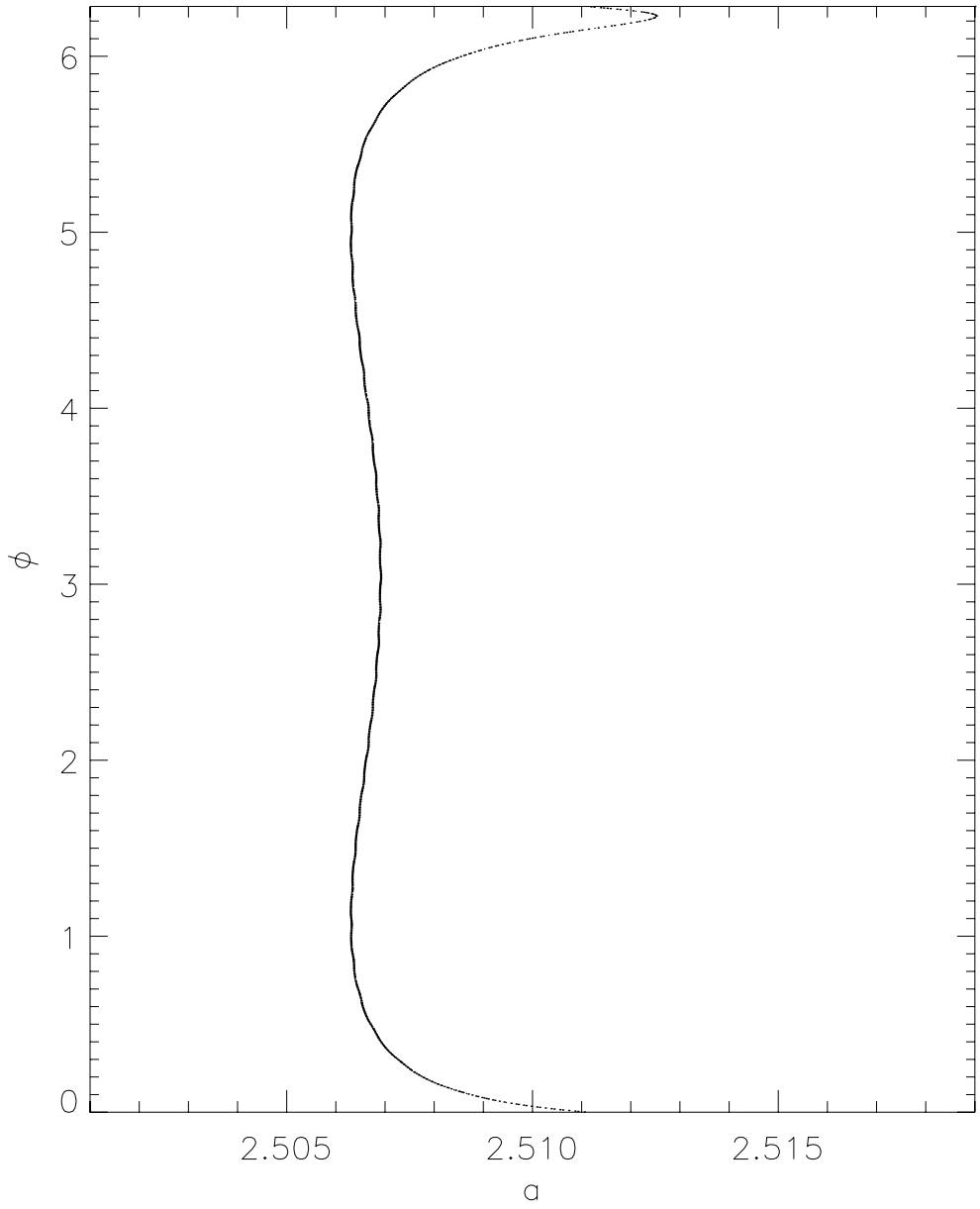

Figure 2.8: a vs. ϕ plot showing 1) a stable circulating trajectory, 2) a stable libration in a 10th-order resonance, and 3) a chaotic trajectory, all calculated via numerical integration with $\mu = 5 \times 10^{-6}$ and $C_J = 3$. The stable circulating trajectory prevents the chaotic trajectory from attaining large a values.

alternating stable and unstable fixed points. According to the KAM theorem, some continuous trajectories—that is, trajectories with irrational K—should also be stable as long as μ is small enough. If a trajectory with rational K is bounded on either side by stable continuous trajectories with irrational K, then the chaos associated with the unstable fixed points is confined to the region bounded by the continuous trajectories. As for the stable fixed points, they are associated with their own librating trajectories; the tadpole analogue made up of islands shown in Figure 2.5 gives an example of such librations. We expect some librations like these to have rational winding numbers and, therefore, their own sets of unstable fixed points and confined chaos on an even smaller scale. In principle, this argument can be applied repeatedly within a single resonance to unearth similar chaotic regions on scales as small as desired.

We can treat the entire (a, ϕ) plane as an extension of this self-similarity to the largest possible scales. If we plot (a, ϕ) as polar coordinates, a $p : p + q$ resonance trajectory appears to 'wind' around the point $a = 0$ with rational winding number $p/(p+q)$. Also, the corresponding resonance is associated with p stable and p unstable fixed points when $p > 1$ and 2 stable and 2 unstable fixed points when $p = 1$. This provides a striking visual analogy to the librations seen within a single resonance.

2.7 Discussion and conclusions

Using simple physical reasoning instead of explicit analysis of terms in the disturbing function, we have developed a framework for studying particles with C_J close to but larger than 3 perturbed into exterior high-eccentricity orbits in the circular planar restricted three-body problem. We have found that, to first order in μ, these orbits move in (a, ϕ) phase space according to a potential with maxima at $\phi = 0, \pi$ separated by symmetrical minima. In the special case of resonance orbits, movement in this potential translates into behavior governed by a modified pendulum equation. Previous pendulum-analogue analyses of this problem have usually been formulated via the disturbing function and the continuous resonant argument (Winter & Murray,

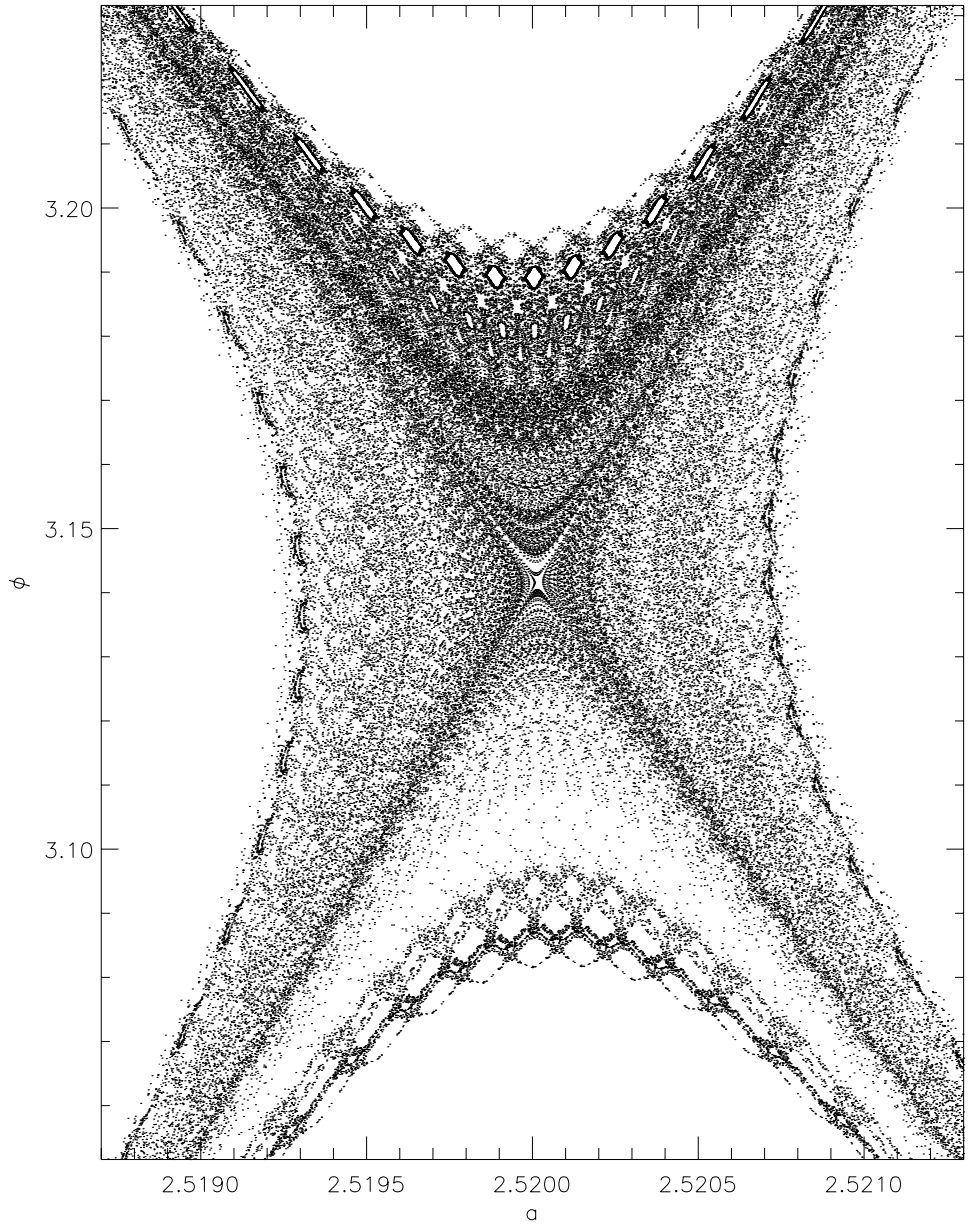

Figure 2.9: A single chaotic trajectory corresponding to the separatrix dividing 'tadpole' and 'horseshoe' librations in the $N = 4$ resonance when $\mu = 10^{-4}$ and $C_J = 3$. This trajectory was computed via numerical integration with the same initial conditions as were used to produce the separatrix trajectory in the middle panel of Figure 2.4. It is confined in the (a, ϕ) plane by stable librations similar to the smallest horseshoe and largest tadpoles shown in Figure 2.4. Note the empty spots in the outer reaches of the chaotic trajectory; these 'avoided' areas correspond to islands of stable librations around stable fixed points in trajectories with rational winding number.

1997a; Dermott & Murray, 1983).

Our analysis, specifically that of mapping, is most similar to that of Malyshkin & Tremaine (1999). They consider the evolution of high-eccentricity comet-like orbits in the low-inclination circular restricted three-body problem by integrating numerically to find the energy kick as a function of the resonant angle at periapse and then using this energy kick to create a mapping that takes one periapse passage to the next. However, Malyshkin & Tremaine (1999) are interested in particle orbits that cross the orbit of the secondary, so the form of their energy kick is qualitatively different from ours. In particular, while a small nonzero orbital inclination would barely affect our energy kick function, it could drastically change the shape of the overall energy kick function in the case of planet-crossing orbits. Partly because of this, they do not discuss their energy kick it in terms of a potential. Also, they focus on the chaotic diffusion of the particle toward escape or capture rather than on motion in resonances.

For $1 : N$ resonance orbits—that is, those we call first-order resonance orbits—the shape of the potential with C_J close to but larger than 3 generates analogues of the Lagrangian points for $N > 1$ resonances. The potential similarly leads to two kinds of libration analogous to the horseshoe and tadpole orbits seen in a $1 : 1$ resonance. $p : N$ resonances—that is, those we call higher-order resonances—show only one kind of libration: when the winding number is large, the sum relating the higher-order resonance potentials to the first-order resonance potential eliminates the indirect term responsible for the tadpole analogues.

Several authors discuss the tadpole analogues' presence or absence in mean-motion resonances in general under the name "asymmetric librations;" Nesvorný & Roig (2001) are the only others we know of to refer to the $1 : N$ resonance librations as "tadpoles" and "horseshoes," though they do not elaborate on this analogy. Some authors have used analytical studies of the Hamiltonian and the disturbing function to set conditions for the existence of asymmetric resonances (Bruno, 1994; Frangakis, 1973; Message, 1970). In particular, Frangakis (1973) analyzed the time-averaged direct and indirect parts of the disturbing function to deduce that only what we call first-order resonances should show asymmetric librations. Bruno (1994) also found

analytically that asymmetric librations only exist in what we call first-order exterior resonances. We confirm this and provide a simple physical explanation.

Others have used numerical methods to confirm the existence of asymmetric librations for particular $1 : N$ resonances and ranges in eccentricity (see, for example, Winter & Murray, 1997b; Beaugé, 1994; Message & Taylor, 1978; Frangakis, 1973; Message, 1958). Some of these also compare their numerical results to expressions for the Hamiltonian correct to first or second order in eccentricity. Although the agreement is generally good for what we call first-order resonances, the Hamiltonian expressions for what we call higher-order resonances tend to predict spurious asymmetric librations. We believe these are due to extra extrema introduced into the potential when too few terms are included in the eccentricity expansion of the Hamiltonian. In some of the more recent studies involving asymmetric librations (Nesvorný & Roig, 2001; Malhotra, 1996) the discussion is framed in terms of the dynamics of the classical Kuiper Belt and so is confined mostly to what we call low-N first-order and low-p higher-order resonances in the low- to moderate-eccentricity regime.

We find a limit on a for stable first-order resonances. Overlap between the resonances creates chaotic regions of (a, ϕ) phase space; for semimajor axes larger than some $a \propto \mu^{-2/5}$, the resonance centers are overlapped and no stable librations are possible. This is the high-eccentricity analogue of the well-known chaotic criterion $|a - 1| \simeq \mu^{2/7}$ found by Wisdom (1980) for the circular planar restricted three-body problem in the low-eccentricity case. We use the Chirikoff criterion for resonance overlap to estimate the location of the onset of chaos. For sufficiently narrow resonances, or small enough μ, there exist regions in (a, ϕ) space that lie outside all of the resonances but that are not chaotic. In the planar problem we consider, particles interior to the circulating trajectories in these regions are never able to escape from the star-planet system.

The basic framework for the behavior of high-eccentricity orbits and the properties of chaotic regions in (a, ϕ) space can be applied to the orbital evolution of small bodies in the solar system. Objects in the Kuiper Belt, for example, are believed to have arrived there via interactions with Neptune (see, for example, Malhotra et al., 2000);

we can apply this framework to study their trajectories. Many of these objects are known to be in resonances (see Chiang et al., 2003, for a recent compilation). The mass ratio between Neptune and the sun is $\mu_N = 4.4 \times 10^{-5}$. Since this is above the critical $\mu \approx 5 \times 10^{-6}$, Kuiper belt objects with $C_J = 3$ are either librating around a resonance or moving chaotically. The latter could, in principle, be ejected as there is no stable circulation for that value of $\mu = \mu_N$ and $C_J = 3$. However, the known Kuiper belt objects span a range in C_J of roughly $2.6 < C_J < 3.2$. In the planar problem with $\mu = \mu_N$ and, for example, $C_J = 3.1$, stable circulations exist and protect some of these objects from escape. To study the ultimate fate of such Kuiper belt objects, the effect of inclination must be understood.

Similarly, we might apply this framework to the scattering of small planetesimals by giant protoplanets and could provide insight to numerical integrations such as those of Rasio & Ford (1996) and Ford et al. (2001). Studies like this require an investigation of the way in which the energy kicks move orbits through the 'global chaos' region surrounding the resonances in the (a, ϕ) plane. Although the antisymmetry of $\Delta E^1(\phi)$ about $\phi = 0$ suggests that the orbits should random walk through phase space, effects of nearby resonances (e.g., Malyshkin & Tremaine, 1999) and terms of higher order in μ become important on timescales long enough for escape to become possible. The importance of second-order effects may be understood as follows. Since the amount of extra energy needed to escape is $1/a_{\rm init} \sim 1$ and the energy kick per orbit is $\sim \mu$, we expect that the average number of kicks needed to escape is $\sim \mu^{-2}$. Note that unlike the first-order kicks, the $\mathcal{O}(\mu^2)$ energy kicks do not average to 0 over the interval $(-\pi, \pi]$ in ϕ. This is also apparent from Figure 2.1. Therefore, with μ^{-2} kicks, the sum of $\mathcal{O}(\mu^2)$ effects produced by the energy kicks will be of order unity—that is, of size comparable to the total first order effect.

Acknowledgements. We thank Peter Goldreich for useful discussions.

This chapter was originally published in 2004 in the *Astronomical Journal*. It is reproduced here with the permission of the copyright holder, the American Astronomical Society.

Chapter 3

Shaping the Kuiper belt size spectrum by shattering large but strengthless bodies

Abstract

The observed size distribution of Kuiper belt objects (KBOs)—small icy and rocky solar system bodies orbiting beyond Neptune—is well described by a power law at large KBO sizes. However, recent work by Bernstein et al. (2004) indicates that the size distribution breaks and becomes shallower for KBOs smaller than about 70 km in size. Here we show that we expect such a break at KBO radius ∼40 km since destructive collisions are frequent for smaller KBOs. Specifically, we assume that KBOs are gravity-dominated bodies with negligible material strength. This gives a power-law slope $q \simeq 3$ where the number $N_{>r}$ of KBOs larger than a size r is given by $N_{>r} \propto r^{1-q}$; the break location follows from this slope through a self-consistent calculation. The existence of this break, the break's location, and the power-law slope we expect below the break are consistent with the findings of Bernstein et al. (2004). The agreement with observations indicates that KBOs as small as ∼40 km are effectively strengthless.

3.1 Introduction

The Kuiper belt, a population of small bodies moving beyond the giant planets, was discovered when its first member was found in 1992 (Jewitt & Luu, 1993). As of late 2003, ∼800 KBOs have been discovered. Due to KBOs' faintness, however, the size distribution of KBOs is well determined observationally only for bodies larger than ∼100 km (Trujillo et al., 2001; Gladman et al., 1998; Chiang & Brown, 1999). Their size distribution is usually parametrized as a power law $N_{>r} \propto r^{1-q}$; its slope is consistent with $q = 5$ ($N_{>r} \propto r^{-4}$) (Bernstein et al., 2004). Numerical studies concluded that the differential size distribution below ∼100 km should follow a power law with the somewhat shallower $q = 3.5$ ($N_{>r} \propto r^{-2.5}$) due to the effects of destructive collisions (Farinella & Davis, 1996; Davis & Farinella, 1997; Kenyon, 2002). The results seemed consistent with loose observational constraints available on the number of ∼2 km KBOs based on the number of Jupiter-family comets seen (Holman & Wisdom, 1993).

In this context, the deficit in small KBOs observed by Bernstein et al. (2004) was a surprise. Using the Advanced Camera for Surveys recently installed on the Hubble Space Telescope, they found just 3 KBOs of size ∼25–45 km where they expected ∼85 such bodies based on an extrapolation of the accepted best-fit large-KBO size distribution at the time (Trujillo et al., 2001). While this observed decrement of more than an order of magnitude in the number of small KBOs clearly indicates a break between 45 and 100 km, the exact break position and slope below the break may well be refined by future data on small KBOs. Still, the results of Bernstein et al. (2004) are inconsistent with the previously expected small-end distribution $q = 3.5$ at better than 95% confidence.

This paper describes a simple self-consistent analytic calculation of the break location and the slope below the break. Note that using the $N_{>r} \propto r^{-4}$ size distribution obtained by Bernstein et al. (2004) for large KBOs, we can estimate the size below which collisions between equal size bodies should be frequent to be $\sim$ 1 km—well below the observed break location. However, this estimate needs two modifications.

First, due to the large velocity dispersion in the Kuiper belt, small bodies can shatter much larger objects. Since there are more small than large bodies, destructive collisions will occur frequently even for objects much larger than 1 km. Second, when collisions are important, they reduce the number of small bodies; this in turn decreases the frequency of collisions. Therefore, calculations of the effects of collisions and the size below which collisions are important must be done in a self-consistent manner.

3.2 Slope of the steady-state distribution

In order to find the break location self-consistently, we first calculate the power-law slope q for a collisional population of bodies. We assume a group of bodies with isotropic velocity dispersion v in which the cumulative number of bodies of radius r is given by a power law $N_{>r} \propto r^{1-q}$. This implies a differential distribution $dN_{>r}/dr \propto r^{-q}$. If we assume that the population is in a steady state and that mass is conserved in the collision process, the total mass of bodies destroyed per unit time in a logarithmic interval in radius must be independent of size. This situation is analogous to that of a turbulent cascade where the total energy transported per unit time by eddies of a given size into smaller eddies is independent of size because the system is in steady-state and no energy pile-up occurs at any point.

Note that our conservation of mass argument is equivalent to the standard approach (see, for example, Dohnanyi, 1969; Tanaka et al., 1996; O'Brien & Greenberg, 2003) in which the rates of destruction and creation for a given body size are equated. Assume for simplicity that all of the mass in a dispersed target of size R will go into fragments of some characteristic size $r(R)$ (Fig. 3.1). The standard approach equates the mass creation rate of bodies of size $r(R)$, or process I in Fig. 3.1, to the mass destruction rate of the same bodies, or process II in Fig. 3.1. We reinterpret process I as the destruction of mass in bodies of size R since this is the process that creates bodies of size $r(R)$. Then the steady-state condition—rate of process I = rate of process II—says that the mass destruction rates for size $r(R)$ bodies and size R bodies

must be equal. Since this holds for all target sizes, the mass destruction rate must be independent of size. A more detailed discussion of the mass conservation argument is given in the Appendix.

We assume that the main channel for mass destruction is the shattering of larger "targets" of size r by smaller "bullets" of size $r_B(r)$ (Fig. 3.1). Under this condition, a constant mass destruction rate reads

$$\rho r^3 \cdot N_{>r} \cdot \frac{N_{>r_B}}{V} \cdot r^2 \cdot v = \text{constant} \quad . \tag{3.1}$$

Here ρ is the internal density of each body and $r_B(r)$ is the size of the smallest bullet that, on impact, can shatter a target of radius r. V is the volume occupied by all the bodies; their velocity dispersion and therefore their distribution within V are assumed independent of body size. We have also used the fact that $N_{>r}$ equals the number of bodies of size r up to a factor of order unity. When supplemented by a relation between the sizes of the bullet and target, Eq. 3.1 dictates the power-law index q.

This very simple formalism based on conservation of mass captures the essence of Dohnanyi's (1969) more elaborate pioneering treatment. Based on laboratory experiments that involved solid bodies dominated by material strength, Dohnanyi chose $r_B \propto r$. When $r_B \propto r$ and $N_{>r} \propto r^{1-q}$ are inserted into Eq. 3.1, we retrieve the $q = 7/2$ of Dohnanyi and several subsequent authors (for example, Williams & Wetherill, 1994; Tanaka et al., 1996). This slope is much steeper than the best-fit small-end $q = 2.3$ found by Bernstein et al. (2004), who rule out $q = 7/2$ at better than 95% confidence.

Indeed, work on the structure of small solar system bodies suggests that many of them are gravitationally bound rubble piles rather than solid monoliths. Based on oscillating lightcurves of the large KBO (20000) Varuna (radius $R > 100$ km), Jewitt & Sheppard (2002) find that this body has density ~ 1 g cm^{-3} and is therefore unlikely to be solid. However, other effects may also be responsible for the lightcurve shape (see, for example, Goldreich et al., 2004). The rotation statistics of much smaller bodies ($R \sim 10$ km) in the more easily observed region between the asteroid belt and

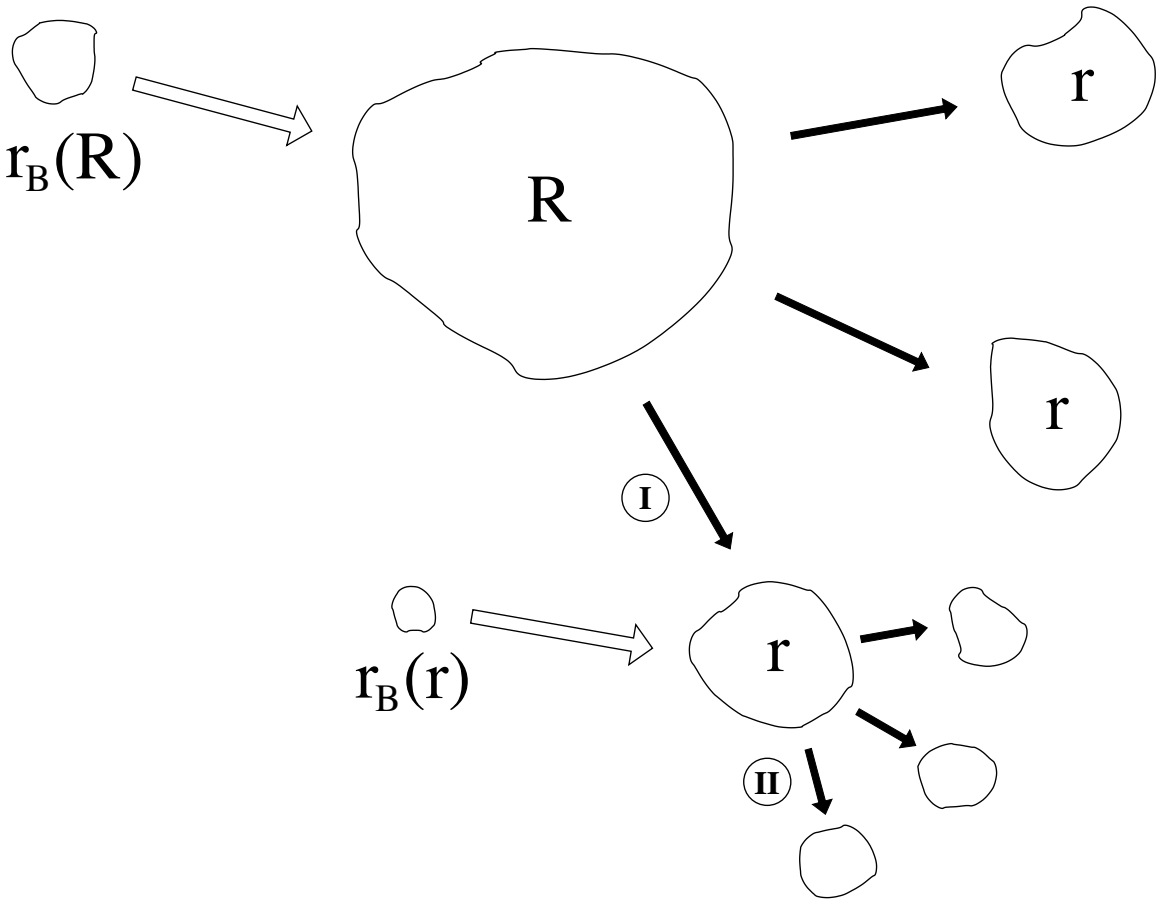

Figure 3.1: Schematic of the collisional cascade: bullets of size $r_B(R)$ shatter targets of typical size R (process I); these targets break into new targets of size r, which are in turn shattered by bullets of size $r_B(r)$ (process II); and so on. Since mass is conserved in collisions, the mass destruction rate of bodies of size R is the mass creation rate of bodies of size r. Steady state then requires that the rate of process I and process II be equal, so that the rate of mass destruction is independent of body size.

the sun also suggest that small bodies in the solar system are rubble piles rather than monoliths. That no small asteroids are observed to rotate faster than their breakup speed suggests that those which were spun up beyond breakup simply broke apart (Harris, 1996); this in turn suggests that these asteroids have no tensile strength. A study including 26 small near-earth asteroids came to similar conclusions about asteroid internal structure (Pravec et al., 1998). The most detailed probe available of the structure of small KBOs is research on short-period comets, kilometer-sized bodies that are thought to have originated in the Kuiper belt. Work on the breakup and impact of comet Shoemaker-Levy 9, thought to be 1–2 km in size, indicates that its strength before breakup was ~ 60 dyn cm^{-2} or less (Asphaug & Benz, 1996); a body like Shoemaker-Levy 9 would have a binding energy due to material strength of at most about ten times less than its gravitational energy. These indications motivate an investigation of the influence of negligible material strength on the fragmentation size distribution.

We might therefore replace the $r_B \propto r$ destruction criterion used by Dohnanyi with the requirement that the kinetic energy of the bullet be equal to the total gravitational energy of the target:

$$\rho r_B^3 v^2 \sim \rho r^3 v_{\rm esc}^2 \tag{3.2}$$

where $v_{\rm esc} \sim \sqrt{G\rho} r$ is the escape velocity from a target of size r, and, again, v is the bodies' constant velocity dispersion. Then

$$r_B(r) \sim \left(\frac{G\rho}{v^2}\right)^{1/3} r^{5/3} \sim r_{\rm eq}^{-2/3} r^{5/3} \quad , \quad r_{\rm eq} \sim \frac{v}{\sqrt{G\rho}} \quad . \tag{3.3}$$

Physically, $r_{\rm eq}$ is the size of a body whose escape velocity equals the velocity dispersion of the system. The Kuiper belt's current velocity dispersion of $v \sim 1$ km s^{-1} follows from the inclinations reported by Brown (2001) and Trujillo et al. (2001) and from the average eccentricity $\bar{e} \simeq 0.12$ obtained from data provided by the IAU Minor Planet Center. When velocity dispersion v and density $\rho \sim 1$ g cm^{-3} are used, $r_{\rm eq} \sim 10^3$ km $\sim$ the radius of Pluto. Equivalently, a target of size r_{eq}, or roughly

Pluto's size, would require a bullet of equal mass to shatter it. Then a body smaller than Pluto—that is, virtually any KBO—can be shattered by bullets smaller than itself. When we substitute Eq. 3.3, or essentially the proportionality $r_B \propto r^{5/3}$, into Eq. 3.1, we get the power-law slope

$$q = 23/8 \quad . \tag{3.4}$$

Recently, O'Brien & Greenberg (2003) extended Dohnanyi's treatment to other destruction conditions where r_B scales as an arbitrary power of r; they show that q is a simple function of this power so that a range of q values can be obtained from a calculation like Dohnanyi's. The simple argument we express in Eq. 3.1 reproduces their analytic results for q. Eq. 3.3 is a special cases of their general power law which is clearly motivated by energy considerations and which leads to the size distribution given by Eq. 3.4.

3.3 Realistic destruction criteria

The destruction criterion just discussed neglects any energy loss during the impact process. It is then a lower limit on the energy needed to shatter and disperse a given target. Indeed, numerical simulations and dimensional analysis of impact events find that in the "gravity regime," or target size range where gravity dominates material strength, the impact energy needed to shatter a given target lies well above the level indicated by Eq. 3.3 (Housen & Holsapple, 1990; Holsapple, 1994; Love & Ahrens, 1996; Melosh & Ryan, 1997; Benz & Asphaug, 1999). Further, the $r_B(r)$ scalings indicated by these studies[1] are consistently shallower than the one in Eq. 3.3. With $r_B \propto r^\alpha$, they give $1.37 \leq \alpha \leq 1.57$ rather than the $\alpha = 5/3$ in Eq. 3.3.

Upon insertion into Eq. 3.1, the $r_B(r)$ scalings above give $2.95 < q < 3.11$. These values indicate a power-law slope between the one given by Eq. 3.4 and Dohnanyi's $q = 3.5$. This range in q is consistent with the best-fit slope $q = 2.8 \pm 0.6$ (95%

[1] Again, we assume a constant velocity dispersion for the collisional population.

confidence) derived by Bernstein et al. (2004) below the break for the classical Kuiper belt and with the best-fit $q = 2.3^{+0.9}_{-1.1}$ (bounds of 68% confidence contour) slope they find for the entire Kuiper belt. The value for the entire belt may be skewed downward by the scattered Kuiper belt data, which include too few faint objects for the scattered belt's small-end slope to be well determined. The observed KBO size distribution is thus consistent with the assumption that gravity dominates material strength in KBOs of size near the break.

That the simulations give $r_B(r)$ scalings shallower than that of Eq. 3.3 implies that the energy lost in a catastrophic collision depends on the bullet/target size ratio. As has previously been noted (see, for example, Melosh & Ryan, 1997), we would expect energy loss in the impact of a small bullet on a much larger target. Initially the bullet would transfer most of its energy to a volume the size of itself at the impact site; much of this energy would escape from the site via a small amount of fast ejecta, though some would propagate through the target as a shock.

Somewhat more quantitatively, we can think of a collision between a very small bullet and a large target as a point explosion on the planar surface between a vacuum and a half-infinite space filled with matter. The analogous explosion in a uniform infinite material leads to the Sedov-Taylor blast wave, a self-similar solution of the first type in which total energy is conserved as the spherical shock propagates (Sedov, 1946; Taylor, 1950). By contrast, a point explosion in a half-infinite space is a self-similar solution of the second type (Zel'dovich & Raizer, 1967); the shock moving into the half-space must lose energy as some of the shocked material flows into the vacuum. Also, the nonzero pressure in the shocked material increases the momentum in the shock. So as the shock propagates, its velocity should fall off faster than it would have given conservation of energy but slower than it would have in the case of momentum conservation.

We can use these considerations to constrain $r_B(r)$ scalings for catastrophic collisions. We assume that a given target is destroyed if the velocity of the shock wave when it reaches the antipode of the impact site exceeds the escape velocity[2] (see, for

[2]Strictly speaking, this destruction condition requires that the velocity imparted to the target

example, Melosh et al., 1994). Let the shock velocity decay as $v_{\rm shock} \propto x^{-\beta}$ where x is the distance traveled by the shock. If the energy in the shock were conserved, we would expect $\beta = 3/2$ from dimensional analysis; if the momentum were conserved, we would expect $\beta = 3$. Note that both calculations involve the energy and momentum contained in the swept-up material behind the shock front since a strong shock front will impart its energy and momentum to the shocked material. The actual point explosion solution loses energy but gains momentum, so it must have $3/2 < \beta < 3$. To get the criterion for target destruction, we equate the target's gravitational binding energy and the energy in the shock when it arrives at the antipode. In Eq. 3.2 this available kinetic energy was simply the kinetic energy of the incoming bullet. Here the available energy is the energy of the shock after it has penetrated through the target: if we assume the bullet initially deposits its energy in a volume the size of itself, the available energy is smaller than the total impact energy by $(r_B/r)^{2\beta-3}$. The resulting destruction criterion is

$$\rho r_B^3 v^2 \left(\frac{r}{r_B}\right)^{3-2\beta} \sim G\rho^2 r^5 \quad . \tag{3.5}$$

This implies

$$r_B \propto r^{1+1/\beta} \quad , \quad q = \frac{7\beta+1}{2\beta+1} \quad . \tag{3.6}$$

The $3/2 < \beta < 3$ condition requires $4/3 < \alpha < 5/3$ and $23/8 < q < 22/7$, both of which are satisfied by all of the impact simulation and dimensional analysis results discussed at the beginning of this section. Holsapple (1994) mentions that energy and momentum conservation should represent limiting cases for the impact process and that laboratory experiments involving impacts into sand, rock, and water satisfy those limits. Also, the range in q implied by the $r_B(r)$ scalings found in the previous studies discussed above, $2.95 \leq q \leq 3.11$, spans most of the allowed range for q. This suggests that the catastrophic impact process and α depend on more specific details

material by the shock wave at the antipode (rather than the shock velocity itself at the antipode) exceed the escape velocity. However, for strong shocks in strengthless material, the imparted velocity grows linearly with the shock velocity via a slope of order unity (see, for example, Landau & Lifshitz, 1959) so the scalings derived here still hold.

of the collisions such as the equation of state. Finally, note that at $r_B \sim r$ there should be no energy loss because the initial energy is deposited in a volume of linear size r. Eq. 3.5 reflects this. Then the $r_{\rm eq}$ expression in Eq. 3.3 is still valid.

3.4 Location of the break

The above calculation of the size distribution treats $N_{>r}$ as constant in time. To maintain this steady state exactly would require the power law to extend to bodies of infinite size, which is impossible. To find the range of masses where this assumption holds, we first find the size $r_{\rm break}$ of the largest KBO to have experienced a destructive collision after an elapsed time τ. We equate τ to the timescale for destructive collisions for each KBO of size $r_{\rm break}$:

$$\frac{1}{\tau} \sim \frac{N_{>r_B(r_{\rm break})}}{V} \cdot r_{\rm break}^2 \cdot v \quad . \tag{3.7}$$

To get $N_{>r}$ we note that bodies of size $r > r_{\rm break}$, having never collided, should be effectively primordial at time τ. For their size distribution we write $N_{>r} = N_0 r^{1-q_0}$ where $N_0 \sim 4 \times 10^{7q_0-3}$ cm$^{q_0-1}$ from observations Trujillo et al. (2001). This is equivalent to a Kuiper belt with 4×10^4 bodies larger than 100 km. They are spread over an area $A \simeq 1200$ AU^2 in the plane of the solar system Trujillo et al. (2001), so $V \simeq Av/\Omega$ where $\Omega = 0.022$ yr^{-1} is the typical orbital angular velocity of the Kuiper belt. We can now use Eq. 3.5 and the $r_{\rm eq}$ expression in Eq. 3.3 to get $r_{\rm break}$ from Eq. 3.7. With q for the slope below the break and, as above, q_0 and N_0 for the slope and normalization above the break, we have

$$r_{\rm break} \sim \left[\frac{N_0 \Omega \tau}{A} r_{\rm eq}^{7-2q} \right]^{\frac{1}{4+q_0-2q}} \quad . \tag{3.8}$$

If we set $\tau \simeq 4.5 \times 10^9$ yr to be the age of the solar system, take $3/2 < \beta < 3$, and use the observed $q_0 = 5$, we get

$$20 \text{ km} \lesssim r_{\rm break} \lesssim 50 \text{ km} \quad . \tag{3.9}$$

This is consistent with the observed break position of ∼70 km Bernstein et al. (2004). Note that if the system had had the high velocity dispersion assumed above over a time considerably shorter than 4.5 Gyr, the break would have occurred at a much smaller KBO size. We therefore infer that the Kuiper belt's current excited state has been a long-lived phase of at least a few billion years' duration rather than a recent phenomenon.

The evolution of the total mass and velocity dispersion of the Kuiper belt is a potential concern, as the break location depends strongly on both. The mass of the Kuiper belt may have been larger by a factor of ∼100 when the solar system was very young (10^7–10^8 years old) (see, for example, Kenyon, 2002). The collision frequency would have been much higher then, so collisions during that period might be expected to have increased the break radius. At that time, though, the velocity dispersion of KBO precursors is believed to have been just ∼1 m/s (see, for example, Goldreich et al., 2002). With this impact velocity, $r_{\rm eq} \sim 1$ km, so only targets of size <1 km can be shattered by bullets smaller than they. As a result, collisional evolution during the early solar system should only have affected bodies of size <1 km. The observed break in the size distribution must have been created later. The break location could have been affected if there was a sufficiently long period during which both v and the Kuiper belt mass were large.

The timescale on which collisional equilibrium is established for bodies of size r is the time needed for all size r bodies to be replaced (destroyed by catastrophic collisions and, simultaneously, replenished by fragments). This timescale is equivalent to the total mass in bodies of size r divided by their mass destruction rate. Since the mass destroyed per unit time is independent of body size, the time to establish collisional equilibrium is proportional to the mass in bodies of size r. With $q \simeq 3$, the mass contained in bodies of size $r \ll r_{break}$ is $N_{>r}\rho r^3 \propto r$. The time taken to establish collisional equilibrium at body size $r_{\rm break}$ is by definition τ, so the timescale on which collisional equilibrium is established is $(r/r_{\rm break})\tau \ll \tau$. Then the steady-state approximation—our assumption that the rate at which $N_{>r}$ changes is much less than the rate of destructive collisions—is self-consistent for $r \ll r_{\rm break}$. Specifically,

as $r_{\rm break}$ increases, $N_{>r_{\rm break}}$ decreases—both on a timescale τ—and the $q \simeq 3$ power law below $r_{\rm break}$ follows adiabatically (Fig. 3.2). Our formalism yields the asymptotic size distribution far below $r_{\rm break}$ even though the system is not in steady state overall, since for $r \ll r_{\rm break}$ the destruction rate is faster than the evolution timescale of the system. Dohnanyi (1969) did not discuss the slow decrease in $N_{>r}$ by which the size distribution differs from a true steady state; he claimed that non-steady-state power-law solutions do not exist. Bernstein et al. (2004) conjectured that the disagreement between their results and Dohnanyi's calculations might indicate a non-steady-state condition in the Kuiper belt. However, the discussion above shows that the fragmentation size distribution below $r_{\rm break}$ should be unaffected by the system's evolution.

As for the lower size boundary, the strength limit derived by Asphaug & Benz (1996) implies that material strength dominates gravity at $r \lesssim 0.3$ km. Impact simulations reach similar conclusions; they put the threshhold in the 0.1–1 km size range (see, for example, Love & Ahrens, 1996; Melosh & Ryan, 1997; Benz & Asphaug, 1999). Below this size threshhold a different q will apply to an equilibrium collisional population. The changes introduced by this effect in the KBO size distribution below $\sim$100 m will affect the size distribution of larger bodies through catastrophic collisions. Both analysis of the shape of the collisional size distribution and numerical simulations of collisional populations indicate that "waves" may appear in the size distribution due to a break introduced by a different q (O'Brien & Greenberg, 2003). However, the average slope of the size distribution is not affected by its "wavy" shape (Fig 3.3).

3.5 Summary

We have derived a self-consistent size distribution given by $23/8 < q < 22/7$ for a collisional population of bodies whose binding energy is dominated by gravity. We emphasize that this distribution does not truly represent a steady state; instead, the number density of bodies decreases slowly compared to the collision timescale. For the case of the Kuiper Belt, the size distribution's small-end power-law slope $q \simeq 3$ and

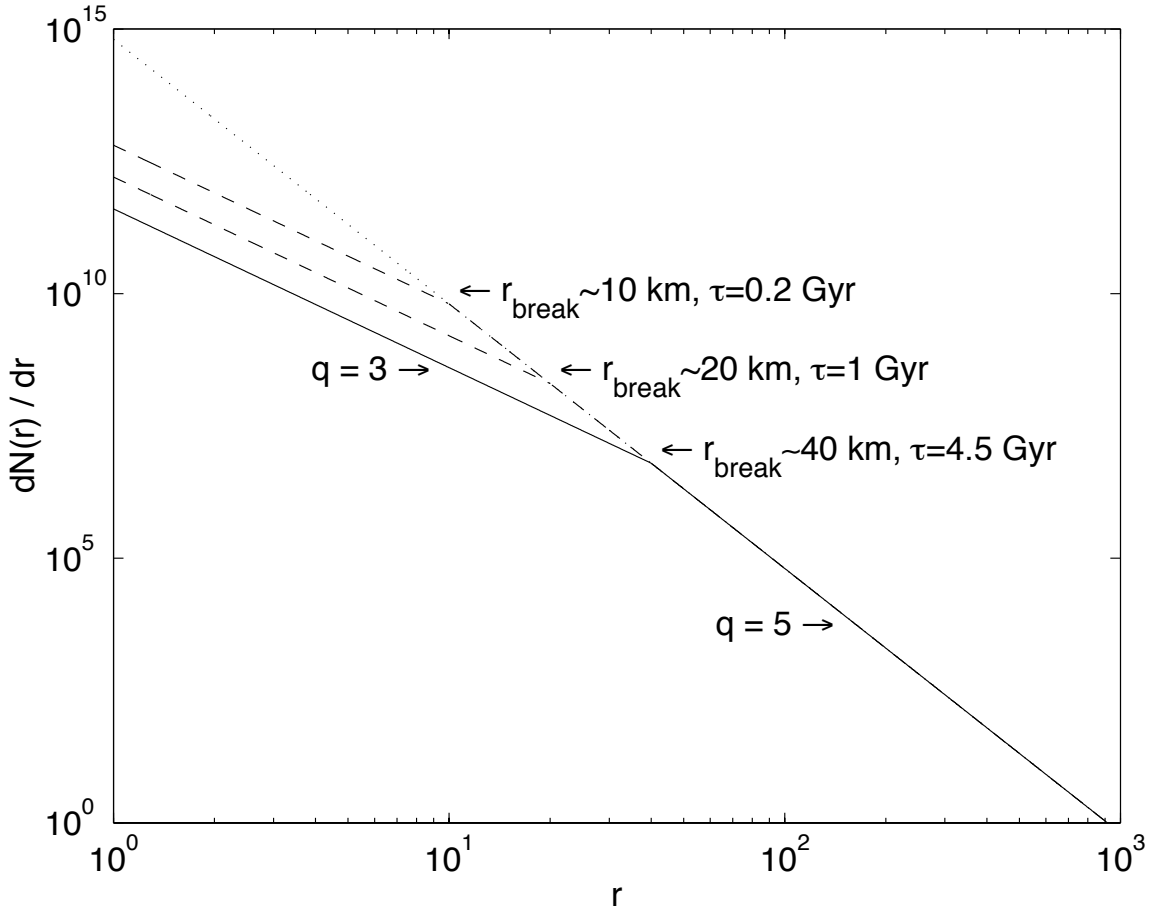

Figure 3.2: Temporal evolution of the number of bodies. Here we use $q = 3$ as a numerical example. The solid line represents the current KBO size distribution. The dotted line is the extrapolation of the large-KBO size distribution to small sizes; we assume this line also represents the primordial size distribution. Dashed lines show the size distribution at earlier times $\tau = 0.2$ and 1 billion years. Because $r_{\rm break}$ increases with time, $N_{>r_{\rm break}}$ decreases with time. The evolution of $r_{\rm break}$ and $N_{>r_{\rm break}}$ is much slower than the rates of collisional destruction and creation below $r_{\rm break}$, so these two rates must be very nearly in balance. Then the steady-state approximation is valid in this size range and the size distribution below $r_{\rm break}$ follows a $q = 3$ power law.

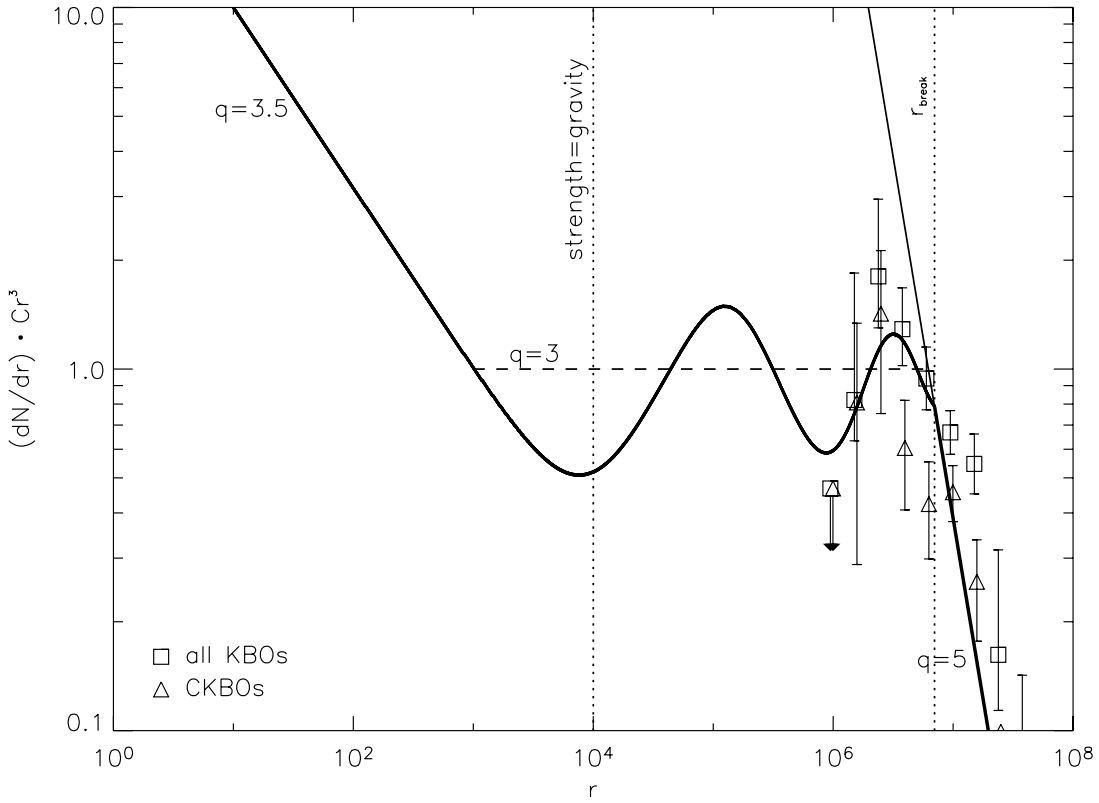
10.0
1.0
0.1
(dN/dr) • Cr³
q=3.5
strength=gravity
r_break
q=3
q=5
□ all KBOs
△ CKBOs
10⁰
10²
10⁴
10⁶
10⁸
r

Figure 3.3: Schematic KBO size distribution (heavy solid line). We multiplied the size distribution by r^3 for this figure in order to show the "waves" more clearly. $r_{\rm break}$ is marked by the vertical dotted line on the right. Bodies smaller than $r_{\rm break}$ have not undergone catastrophic collisions; they follow the primordial size distribution, which we take to be $q \simeq 5$. We assume the transition between strength- and gravity-dominated bodies occurs at $\sim 10^4$ cm (marked by the vertical dotted line on the left). Below this transition, the asymptotic size distribution is close to Dohnanyi's $q = 3.5$ power law. The region where 10^4 cm $< r < r_{\rm break}$, which has an average q of about 3, is the main focus of this paper. Due to the steepening of the size distribution below $\sim 10^4$ cm, there are more bullets of size less than 10^4 cm than would be expected if the $q \simeq 3$ size distribution continued to arbitrarily small sizes. Since these extra bullets can break the smallest targets in the gravity-dominated regime, the excess affects the size distribution far above 10^4 cm: "waves" are produced in the distribution for $\sim 10^4$ cm $< r < r_{\rm break}$ as described by O'Brien & Greenberg (2003). In our calculations of the "wavy" spectrum, we took the energy needed to break a given body to be the sum of the material strength and self-gravity contributions. This produced a smooth transition between the strength- and gravity-dominated parts of the size distribution and a significant decrease in the amplitudes of the "waves" as r increases. Despite the "waves," the gravity-dominated part of the size distribution below $r_{\rm break}$ retains an average q of 3 (shown by the dashed line) and, as a result, lies well below the extrapolation of the primordial size distribution to smaller r (thin solid line). The plotted points represent the KBO size distribution determined observationally by Bernstein et al. (2004) as shown in their Figs. 3 and 4. Squares mark the data points for the entire Kuiper belt; triangles mark the data points for the classical KBOs only. The points were given a constant vertical offset chosen to facilitate comparison between the theoretical and observed shapes of the size distribution. For clarity, the classical KBO data points have also been offset slightly in r.

break radius $r_{\rm break} \sim 40$ km agree well with those found observationally by Bernstein et al. (2004). Since the power-law slope derived in the steady-state approximation depends heavily on the particular criterion for catastrophic destruction adopted for the bodies, observations of the KBO size distribution constrain the balance between internal strength and gravitational binding in KBOs. The close agreement between this slope and break radius and the best-fit values found by Bernstein et al. (2004) suggests that large KBOs are virtually strengthless bodies held together mainly by gravity. Rubble-pile structure for KBOs of size $\sim r_{\rm break}$ and larger is consistent with but not required by these findings since the structural flaws expected in bodies this large may weaken their internal structure enough for gravity to dominate material strength. Further surveys of small KBOs between ∼10 and ∼70 km in size would better constrain both the exact position of the actual break in the size distribution and the power-law slope below the break. Data of this kind would thus confirm or refute our analysis. Such surveys would also allow more detailed comparison of the break locations in the classical and scattered KBO populations, which should reflect differences in the surface densities and velocity dispersions for those two groups.

3.6 Appendix: mathematical justification of the steady-state criterion

We can show mathematically that the standard criterion for a collisional steady state used in the literature (see, for example Dohnanyi, 1969; Tanaka et al., 1996; O'Brien & Greenberg, 2003) follows from our steady-state criterion as expressed in Eq. 3.1. In other words, we can show that if the mass destruction rate per logarithmic interval in target size is independent of target size, then the rates of collisional destruction and creation of bodies of a given size are equal.

We assume that all target bodies break in the same way—that is, that the size distribution of fragments has the same form for all targets and is a function only of the ratio between fragment and target sizes. Then the mass in fragments of size

r created via catastrophic destruction of targets of size R per unit time, per unit fragment size, and per unit target size can be expressed as

$$D(r, R) = A(R) f\left(\frac{r}{R}\right) \quad . \tag{3.10}$$

Here $f(r/R)$ is a dimensionless function that gives the shape of the fragment size distribution and $A(R)$ is a normalization factor that gives the total mass rate of destruction of bodies of size R.

Our criterion that the total mass of bodies destroyed per unit time in a logarithmic interval in body size be independent of body size is

$$\int_0^\infty R\, A(R) f\left(\frac{r}{R}\right)\, dr = \text{constant} \quad . \tag{3.11}$$

A change of variables to $x = r/R$ gives

$$R^2 A(R) = \frac{\text{constant}}{\int_0^\infty f(x)\, dx} \tag{3.12}$$

and, therefore,

$$A(R) = A_0 R^{-2} \tag{3.13}$$

for some constant A_0.

We now show that this form of $A(R)$ also satisfies the standard criterion for a collisional steady state. The mass creation rate for fragments of size r is

$$\int_0^\infty A(R) f\left(\frac{r}{R}\right)\, dR = \frac{A_0}{r} \int_0^\infty f(x)\, dx \quad , \tag{3.14}$$

and the mass destruction rate for targets of size r is

$$\int_0^\infty A(r) f\left(\frac{R}{r}\right)\, dR = \frac{A_0}{r} \int_0^\infty f(x)\, dx \quad , \tag{3.15}$$

so these rates are equal.

Acknowledgements. We thank Oded Aharonson and Andrew McFadyen for useful discussions.

This chapter was originally published in 2005 in *Icarus*.

Chapter 4

Self-similar solutions for relativistic shocks emerging from stars with polytropic envelopes

Abstract

We consider a strong ultrarelativistic shock moving through a star whose envelope has a polytrope-like density profile. When the shock is close to the star's outer boundary, its behavior follows the self-similar solution given by Sari (2005) for implosions in planar geometry. Here we outline this solution and find the asymptotic solution as the shock reaches the star's edge. We then show that the motion after the shock breaks out of the star is described by a self-similar solution remarkably like the solution for the motion inside the star. In particular, the characteristic Lorentz factor, pressure, and density vary with time according to the same power laws both before and after the shock breaks out of the star. After emergence from the star, however, the self-similar solution's characteristic position corresponds to a point behind the leading edge of the flow rather than at the shock front, and the relevant range of values for the similarity variable changes. Our numerical integrations agree well with the analytic results both before and after the shock reaches the star's edge.

4.1 Introduction

The surge of activity over the past decade or so in the fields of supernovae and of gamma-ray bursts and their afterglows has led to renewed investigation into the behavior of strong shocks. Much of the analytic work on strong shock propagation to date has focused on self-similar solutions to the hydrodynamic equations. In these solutions, the profiles of the hydrodynamic variables as functions of position have constant overall shapes whose time evolution consists simply of scalings in amplitude and position. As a result, self-similarity allows us to reduce the nominal system of two-dimensional partial differential hydrodynamic equations to a system of one-dimensional ordinary differential equations. The existence of self-similar solutions thus enables a significant simplification of problems free of spatial scales in regions far from the initial conditions. The best-known such solutions are the pioneering Sedov-Taylor solutions for nonrelativistic point explosions propagating into surroundings with power-law density profiles (Sedov, 1946; von Neumann, 1947; Taylor, 1950).

Self-similar solutions are traditionally divided into two categories (see, for example, Zel'dovich & Raizer (1967) for a detailed discussion). "Type I" solutions are those in which the time evolution of the shock position and hydrodynamic variables follows from global conservation laws such as energy conservation. The Sedov-Taylor solutions are Type I; their ultrarelativistic analogues were found by Blandford & McKee (1976). By contrast, global conservation laws are useless in "Type II" solutions, which are instead characterized by the requirement that the solution remain well-behaved at a singular point known as the "sonic point." If, for instance, the density of the surroundings falls off very quickly with distance, Type II solutions found by Waxman & Shvarts (1993) for nonrelativistic spherical explosions hold instead of the Sedov-Taylor solutions and relativistic solutions found by Best & Sari (2000) hold instead of the Blandford-McKee solutions.

Here we study the case of an ultrarelativistic shock wave moving outwards through a star whose envelope has a polytrope-like density profile. After the shock front reaches the outer edge of the star, an event we refer to as "breakout," the shock

front itself ceases to exist but the shocked fluid continues outward into the vacuum originally surrounding the star. We focus on the flow at times just before and just after breakout. As explained in §4.2, the shock evolution just inside the star's surface is identical to that expected for an imploding planar shock in a medium with a power-law density profile. Such a shock follows a Type II self-similar solution as discussed by Sari (2006) and Nakayama & Shigeyama (2005) and outlined briefly here. §4.3 describes the asymptotic solution as the shock front reaches the surface of the star, a singular point. In §4.4 we investigate the flow after breakout. We show that the self-similar solution for the evolution inside the star also describes the behavior outside the star except in that a different range of the similarity variable applies and in that the physical interpretation of the characteristic position changes. We show in §4.5 that the analytic results of §4.2,4.3,4.4 agree with our numerical integrations of the relativistic time-dependent hydrodynamic equations, and in §4.6 we summarize our findings. Throughout our discussion, we take the speed of light to be $c = 1$.

4.2 Shock propagation within the star

Since we are interested in the shock after it has reached the envelope or the outermost layers of a star, we assume that the mass and distance lying between the shock front and the star's outer edge are much less than the mass and distance between the shock front and the star's center. In this region, we can take the star's gravity g to be constant and the geometry to be planar. We also assume that the stellar envelope has a polytrope-like equation of state, that is, $p \propto \rho^q$ where p is the pressure, ρ is the mass density, and q is a constant. This type of equation of state occurs in various contexts including fully convective stellar envelopes, in which case q is the adiabatic index; radiative envelopes where the opacity has a power-law dependence on the density and temperature; and degenerate envelopes.

Under these assumptions we can find the density profile from hydrostatic equilibrium and the equation of state as follows. Let x be the radial coordinate such that

$x = 0$ at the star's surface and $x < 0$ inside the star. Then

$$0 = \frac{dp}{dx} + \rho g \tag{4.1}$$

and with the boundary condition $\rho = p = 0$ at the edge of the star, we have

$$\frac{q}{q-1}\rho^{q-1} \propto -gx \tag{4.2}$$

$$\rho \propto (-x)^{1/(q-1)} = (-x)^{-k} \quad . \tag{4.3}$$

For convective and degenerate envelopes, q is between 4/3 and 5/3; for radiative envelopes with Kramers opacity, $q = 30/17$. These give k values between -1 and -3.

With the power-law density profile $\rho \propto (-x)^{-k}$, the evolution of an ultrarelativistic shock propagating through the envelope is given by a Type II converging planar self-similar solution to the hydrodynamic equations representing energy, momentum, and mass conservation,

$$\frac{\partial}{\partial t}\left[\gamma^2(e + \beta^2 p)\right] + \frac{\partial}{\partial x}\left[\gamma^2\beta(e + p)\right] = 0 \tag{4.4}$$

$$\frac{\partial}{\partial t}\left[\gamma^2\beta(e + p)\right] + \frac{\partial}{\partial x}\left[\gamma^2(\beta^2 e + p)\right] = 0 \tag{4.5}$$

$$\frac{\partial}{\partial t}(\gamma n) + \frac{\partial}{\partial x}(\gamma\beta n) = 0 \quad , \tag{4.6}$$

with the ultrarelativistic equation of state

$$p = \frac{1}{3}e \quad . \tag{4.7}$$

Here we will simply state the solution; for a detailed derivation see Sari (2006) or Nakayama & Shigeyama (2005). We assume the effect of the star's gravity on the shock propagation is negligible. Following Sari (2006), we let $R(t)$ be the solution's characteristic position, which we choose to be the position of the shock front while the shock is within the star. We take $t = 0$ at the time the shock reaches the star's

surface ($R = 0$), and we take $R < 0$ when $t < 0$. We take $\Gamma(t)$, $P(t)$, and $N(t)$ to be respectively the characteristic Lorentz factor, pressure, and number density, and we define

$$\frac{t\dot{\Gamma}}{\Gamma} = -\frac{m}{2} \quad , \quad \frac{t\dot{P}}{P} = -m - k \quad , \quad \frac{t\dot{N}}{N} = -\frac{m}{2} - k \quad . \tag{4.8}$$

Following Blandford & McKee (1976), we define the similarity variable as

$$\chi = 1 + 2(m+1)\frac{R - x}{R/\Gamma^2} \quad . \tag{4.9}$$

Note that for $R < 0$, $x \leq R$ and the relevant range in χ is $-\infty < \chi < 1$ as long as $m > -1$. We define the hydrodynamic variables—the Lorentz factor γ, the pressure p, and the number density n—as follows:

$$\gamma^2(x,t) = \frac{1}{2}\Gamma^2(t) g(\chi) \tag{4.10}$$

$$p(x,t) = P(t) f(\chi) \tag{4.11}$$

$$n(x,t) = N(t)\frac{h(\chi)}{g^{1/2}(\chi)} \quad . \tag{4.12}$$

Here g, f, and h give the profiles of γ, p, and n; expressions for the dependence of m on k and for g, f, h as functions of χ make up the entire self-similar solution. The above definitions and the ultrarelativistic hydrodynamic equations in planar geometry put the sonic point, the point separating fluid elements that can communicate with the shock front via sound waves from those that cannot, at $g\chi = 4 - 2\sqrt{3}$. Requiring that the solution pass smoothly through this point gives

$$m = \left(3 - 2\sqrt{3}\right) k \tag{4.13}$$

$$g = C_g \left| \frac{g\chi}{3k - 2k\sqrt{3} + 1} - 2(2 + \sqrt{3}) \right|^{-\left(3 - 2\sqrt{3}\right)k} \tag{4.14}$$

$$f = C_f \left| -g\chi - 2k\sqrt{3} + 4 + 2\sqrt{3} \right|^{-\left(4 - 2\sqrt{3}\right)k} \tag{4.15}$$

$$h = C_h \left| g\chi + 2k\sqrt{3} - 4 - 2\sqrt{3} \right|^{-\frac{\left(2\sqrt{3}-3\right)(2k-1)k}{(-1+k\sqrt{3}-\sqrt{3})}} |g\chi - 2|^{\frac{k}{-1+k\sqrt{3}-\sqrt{3}}} \quad . \tag{4.16}$$

The boundary conditions $g(\chi = 1) = f(\chi = 1) = h(\chi = 1) = 1$ that hold inside the star allow us to determine the constants of integration C_g, C_f, C_h and write

$$g = \left[\frac{-g\chi - 2k\sqrt{3} + 4 + 2\sqrt{3}}{-1 - 2k\sqrt{3} + 4 + 2\sqrt{3}} \right]^{-\left(3-2\sqrt{3}\right)k} \tag{4.17}$$

$$f = \left[\frac{-g\chi - 2k\sqrt{3} + 4 + 2\sqrt{3}}{-1 - 2k\sqrt{3} + 4 + 2\sqrt{3}} \right]^{-(4-2\sqrt{3})k} \tag{4.18}$$

$$h = \left[\frac{g\chi + 2k\sqrt{3} - 4 - 2\sqrt{3}}{1 + 2k\sqrt{3} - 4 - 2\sqrt{3}} \right]^{-\frac{\left(2\sqrt{3}-3\right)(2k-1)k}{-1+k\sqrt{3}-\sqrt{3}}} [2 - g\chi]^{\frac{k}{-1+k\sqrt{3}-\sqrt{3}}} \quad . \tag{4.19}$$

4.3 Transition at breakout

To know what happens to the shocked material after the shock front emerges from the star, we need the behavior of the shock just as the front reaches the surface—the "initial conditions" for the evolution of the shock after breakout. Specifically, we are interested in the limiting behavior of each fluid element and in the asymptotic profiles of γ, p, and n as functions of x as t and R approach 0.

The limiting behavior of a given fluid element may be found as follows. Due to the self-similarity, we know the time taken for γ, p, and n of a given fluid element to change significantly is the timescale on which R changes by an amount of order itself. Since R can change by this much only once between the time a given fluid element is shocked and the time the shock breaks out of the star, the limiting values of γ, p, and n for that fluid element should be larger only by a factor of order unity from their values when the fluid element was first shocked.

We can also find the scalings of γ, p, and n with x at breakout via simple physical arguments. We denote by x_0, γ_0, p_0, n_0 the position, Lorentz factor, pressure, and number density of a fluid element just after being shocked and by x_f, γ_f, p_f, n_f those values at the time the shock breaks out. Since the shock accelerates to infinite

Lorentz factors, and since, as we found above, the Lorentz factor of a given fluid element remains constant up to a numerical factor, this fluid element will lag behind the shock by $x_f \sim x_0/\gamma_0^2$ at $t = 0$. Eq. 4.8 gives $\Gamma \sim t^{-m/2}$, so we have $\gamma_0 \sim (-x_0)^{-m/2}$; then $\gamma_f \sim ((-x_f)\gamma_f^2)^{-m/2}$ or

$$\gamma_f \sim (-x_f)^{-m/2(m+1)} \quad . \tag{4.20}$$

Likewise, since $P \sim t^{-m-k}$ and $N \sim t^{-m/2-k}$, we have $p_0 \sim x_0^{-m-k}$ and $n_0 \sim x_0^{-m/2-k}$; then

$$p_f \sim ((-x_f)\gamma_f^2)^{-m-k} \sim (-x_f)^{-(m+k)/(m+1)} \tag{4.21}$$

$$n_f \sim (-x_f)^{-(m/2+k)/(m+1)} \quad . \tag{4.22}$$

We can use the equations for the solution before breakout to perform equivalent calculations of the limiting behavior of fluid elements and asymptotic profiles of γ, p, n. For the limiting behavior of a fluid element, we take the advective time derivative of $g\chi$ and use the result to relate γ and g to time for that fluid element. The advective derivative is given by

$$\frac{D}{Dt} = \frac{\partial}{\partial t} + \beta\frac{\partial}{\partial r} = \dot{\Gamma}\frac{\partial}{\partial \Gamma} + \dot{P}\frac{\partial}{\partial P} + \frac{m+1}{t}(2/g - \chi)\frac{\partial}{\partial \chi} \quad . \tag{4.23}$$

We apply this derivative to Eq. 4.17 to get

$$\frac{D(g\chi)}{D\log t} = \frac{(2 - g\chi)\left(g\chi - 4 - 2\sqrt{3} + 2\sqrt{3}k\right)}{\left(g\chi - 4 - 2\sqrt{3}\right)} \tag{4.24}$$

and integrate to get

$$t/t_0 = |g\chi - 2|^{(3+\sqrt{3})/(3k-\sqrt{3}-3)} \left|\frac{g\chi - 4 - 2\sqrt{3} + 2k\sqrt{3}}{1 - 4 - 2\sqrt{3} + 2k\sqrt{3}}\right|^{-3k/\left(-\sqrt{3}-3+3k\right)} \tag{4.25}$$

where t_0 is the time at which the fluid element is shocked, that is, when $g = \chi = 1$. When $|g\chi| \gg 1$—which becomes true everywhere behind the shock front as $t \to 0$—

this simplifies to

$$t/t_0 \simeq |g\chi|^{-1} \left|1 - 4 - 2\sqrt{3} + 2k\sqrt{3}\right|^{3k/\left(-\sqrt{3}-3+3k\right)} \tag{4.26}$$

and Eq. 4.17 simplifies to

$$g \simeq \left[\frac{-g\chi}{-1 - 2k\sqrt{3} + 4 + 2\sqrt{3}}\right]^{-\left(3-2\sqrt{3}\right)k} \quad . \tag{4.27}$$

We substitute Eq. 4.26 into Eq. 4.27 to get the limiting Lorentz factor of the fluid element as $t \to 0$:

$$\gamma = \gamma_0 \left|1 - 4 - 2\sqrt{3} + 2k\sqrt{3}\right|^{-\left(3-3\sqrt{3}\right)k/\left(2\left(-\sqrt{3}-3+3k\right)\right)} \tag{4.28}$$

which is greater only by a numerical factor than the initial Lorentz factor γ_0 that the fluid element received right after being shocked. To relate the limiting p, n to p_0, n_0, we likewise take Eqs. 4.18, 4.19 in the limit $|g\chi| \gg 1$ and use Eqs. 4.26, 4.27 with the results to get

$$p = p_0 \left|1 - 4 - 2\sqrt{3} + 2k\sqrt{3}\right|^{-\left(6-2\sqrt{3}\right)k/\left(-\sqrt{3}-3+3k\right)} \tag{4.29}$$

$$n = n_0 \left|1 - 4 - 2\sqrt{3} + 2k\sqrt{3}\right|^{-\frac{\left(4k+k\sqrt{3}-3-\sqrt{3}\right)\left(3-2\sqrt{3}\right)k}{2\left(k\sqrt{3}-1-\sqrt{3}\right)}} \tag{4.30}$$

which again differ only by numerical factors from their values just after the fluid element is shocked. This is consistent with the behavior given above by simple physical considerations.

For the calculation of the asymptotic profiles of γ, p, and n as functions of x, we cannot simply apply Eqs. 4.10, 4.11, 4.12: Eqs. 4.8, 4.9 require that $\chi \to -\infty$ everywhere behind the shock and that Γ, P, and N diverge as $t \to 0$. Instead we take the $t \to 0$ or, equivalently, $\chi \to \infty$ limit at a fixed position x. First we have

$$\chi = 1 + 2(m+1)(1 - x/R)\Gamma^2 \simeq 2(m+1)(-x/R)\Gamma^2 \quad . \tag{4.31}$$

With Eqs. 4.10, 4.27 this gives

$$2\gamma^2/\Gamma^2 = g = \left[\frac{-4(m+1)(-x)\gamma^2/R}{-1-2k\sqrt{3}+4+2\sqrt{3}}\right]^{-m} \tag{4.32}$$

and

$$\gamma = \left[2\frac{(-R)^{-m}}{\Gamma^2}\right]^{-1/2(1+m)} \left[\frac{4(m+1)}{-1-2k\sqrt{3}+4+2\sqrt{3}}\right]^{-m/2(1+m)} (-x)^{-m/2(1+m)} \quad . \tag{4.33}$$

This is consistent with our qualitative discussion; the coefficient in the qualitative relation is a numerical factor times the constant $(-R)^{-m}/\Gamma^2$. For the p and n profiles, we apply a similar analysis to the expressions for f and h in the limit $t \to 0$.

$$p = P\left[2\frac{(-R)}{\Gamma^2}\right]^{\frac{m+k}{1+m}} \left[\frac{4(m+1)}{-1-2k\sqrt{3}+4+2\sqrt{3}}\right]^{-\frac{m+k}{1+m}} (-x)^{-\frac{m+k}{1+m}} \tag{4.34}$$

$$\begin{aligned} n &= N\left[2\frac{(-R)}{\Gamma^2}\right]^{\frac{m/2+k}{1+m}} [4(m+1)]^{-\frac{m/2+k}{1+m}} \left[-1-2k\sqrt{3}+4+2\sqrt{3}\right]^{\frac{m/2+k}{1+m}+\frac{k}{-1+k\sqrt{3}-\sqrt{3}}} \\ &\quad \times (-x)^{-\frac{m/2+k}{1+m}} \end{aligned} \tag{4.35}$$

These results are likewise consistent with our qualitative discussion.

4.4 Evolution after breakout

4.4.1 Self-similar solution

Since the breakout itself does not introduce new spatial scales into the flow, we expect the motion after breakout to remain self-similar. However, as the shock Lorentz factor diverges at $t = 0$, we cannot continue to associate the characteristic position, Lorentz factor, pressure, and number density with the values at the shock front after breakout. So we begin by providing physical motivation for a different characteristic Lorentz factor and exploring the implications of this choice.

We note that after breakout each fluid element expands and accelerates over time until the element's internal energy has been converted entirely into bulk motion. Given a relativistic strong shock, the internal energy of a shocked fluid element in the frame moving with the fluid is comparable to the bulk kinetic energy of the fluid element. This implies that the fluid element's final bulk Lorentz factor should be much greater than the value of the shock Lorentz factor just after the fluid element was shocked. The timescale t_x for the resulting expansion and acceleration is the time over which the fluid element's size and Lorentz factor change by a factor of order unity. For a fluid element located at $-x$ and with Lorentz factor γ_x at $t = 0$, the time of breakout, this timescale is $t_x = x\gamma_x^2$ due to relativistic beaming. That every time $t > 0$ is thus associated in a scale-independent way with a particular t_x and γ suggests that we pick $\Gamma(t = t_x) = \gamma_x$ to be the characteristic Lorentz factor.

To see how Γ evolves with time, we use $\gamma \propto (-x)^{-m/2(1+m)}$ from Eq. 4.33 with the t_x relation above to get $\Gamma \propto t^{-m/2}$. For the characteristic pressure P and number density N, Eqs. 4.34, 4.35 likewise give $P \propto t^{-m-k}$ and $N \propto t^{-m/2-k}$. In other words, Eq. 4.8 holds after breakout with exactly the same k, m that apply inside the star. The characteristic position R is again the position which evolves according to the Lorentz factor Γ: $\dot{R} \simeq 1 - 1/2\Gamma^2$. Since the hydrodynamic equations still hold as well, Eqs. 4.9, 4.14, 4.15, 4.16 must remain valid when $t > 0$.

To find the complete solution after breakout we need to specify the boundary conditions. We proceed by looking at the behavior of the similarity variables χ, g, f, h. The relevant range in χ depends on R, and while the relation between R and Γ is the same before and after breakout, R after breakout is not the position of the front. Instead, the front has infinite Lorentz factor and R lags farther and farther behind the front with increasing time. A nice physical interpretation exists for R after breakout. R tracks the position corresponding to a fluid element that has expanded by a factor of order unity, so R marks the transition in position between fluid elements that have expanded and accelerated significantly since being shocked and fluid elements whose size and speed have remained roughly constant. Since it takes longer for fluid elements with smaller Lorentz factors to expand and accelerate

significantly, R moves backward relative to the leading edge of the flow at $x = t$. R is positive after breakout, and the range of possible x in the solution outside the star is $x \leq t$. So $\chi = 0$ at the "front" $x = t$, and the relevant range in χ in the post-breakout solution is $0 < \chi < \infty$ rather than $-\infty < \chi < 1$.

Far behind $x = t$, the profiles of γ, p, and n before breakout must coincide with the profiles after breakout. We know this because at a given time after breakout, sound waves carrying the information that breakout occurred can only have traveled a finite distance; material farther behind the front continues to flow as if the breakout had never occurred. Also, the two sets of profiles must coincide at $t = 0$, when everything is far behind the front. To phrase this requirement on the profiles in terms of the similarity variable, $g(\chi \to -\infty)$, $f(\chi \to -\infty)$, and $h(\chi \to -\infty)$ before breakout must coincide with $g(\chi \to \infty)$, $f(\chi \to \infty)$, and $h(\chi \to \infty)$ after breakout. Then as $\chi \to \infty$ after breakout, $g, f, h \to 0$ and $g\chi \to \infty$. In addition, the constants C_g, C_f, C_h in Eqs. 4.14, 4.15, 4.16 must be the same for both the pre- and post-breakout solutions. In other words, the solutions before and after breakout, as specified by Eqs. 4.9, 4.14, 4.15, 4.16 and expressions for C_g, C_f, C_h, are the same; only the relevant ranges in χ and the physical interpretations of the variables differ. So the expressions for g, f, h after breakout are

$$g = \left[\frac{g\chi + 2k\sqrt{3} - 4 - 2\sqrt{3}}{-1 - 2k\sqrt{3} + 4 + 2\sqrt{3}}\right]^{-\left(3-2\sqrt{3}\right)k} \tag{4.36}$$

$$f = \left[\frac{g\chi + 2k\sqrt{3} - 4 - 2\sqrt{3}}{-1 - 2k\sqrt{3} + 4 + 2\sqrt{3}}\right]^{-(4-2\sqrt{3})k} \tag{4.37}$$

$$h = \left[\frac{-g\chi - 2k\sqrt{3} + 4 + 2\sqrt{3}}{1 + 2k\sqrt{3} - 4 - 2\sqrt{3}}\right]^{-\frac{\left(2\sqrt{3}-3\right)(2k-1)k}{-1+k\sqrt{3}-\sqrt{3}}} [g\chi - 2]^{\frac{k}{-1+k\sqrt{3}-\sqrt{3}}} \quad . \tag{4.38}$$

The boundary conditions after breakout are given explicitly by $g = f = 1$ and $h = \left(5 + 4\sqrt{3} - 4\sqrt{3}k\right)^{k/\left(-1-\sqrt{3}+k\sqrt{3}\right)}$ at $\chi = 7+4\sqrt{3}-4\sqrt{3}k$. A graphical comparison between the pre- and post-breakout γ versus position profiles is given in Figure 4.1 along with sample trajectories of fluid elements.

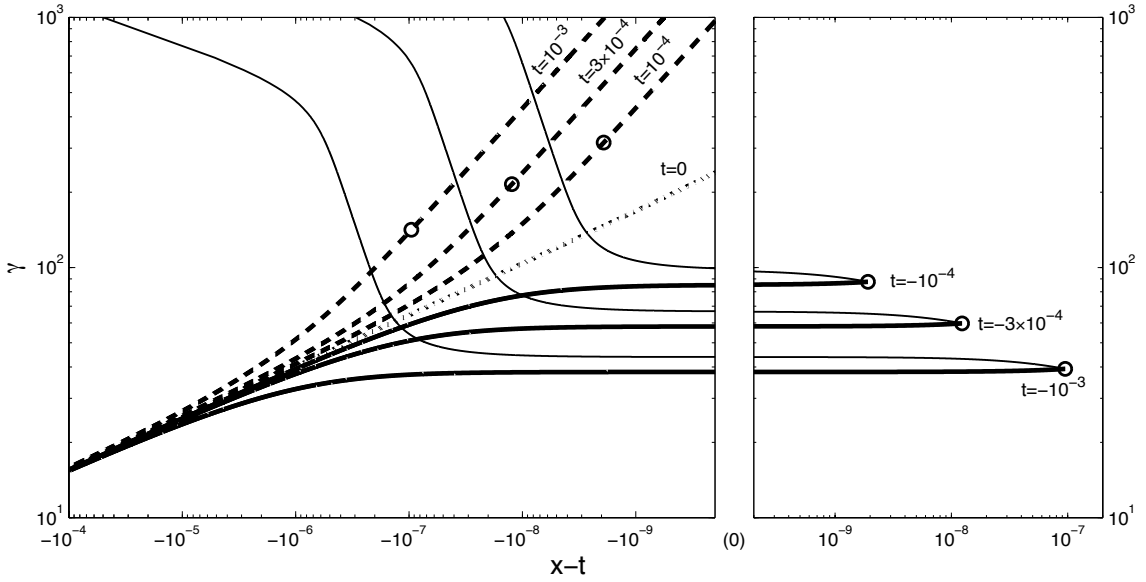

Figure 4.1: Profiles of γ as a function of position (heavy lines) at seven different times marked on the figure and trajectories of three fluid elements in position-Lorentz factor space (thin lines). Fluid elements at the characteristic positions R are marked by open circles. We use $x - t$ as the position coordinate to allow easy comparison of the profiles. The $t = 0$ curve (heavy dotted line) is the asymptotic profile corresponding to the pure power law $\gamma \propto (-x)^{-m/2(1+m)}$ given in Eq. 4.33. The profiles with $t < 0$ (heavy solid lines) are given by Eqs. 4.10, 4.17 and the profiles with $t > 0$ (heavy dashed lines) are given by Eqs. 4.10, 4.36. When $t < 0$, the natural choices for R and Γ are respectively the location of the shock front and the Lorentz factor of the front. When $t > 0$, a fluid element at position R has accelerated by a factor of order unity and its Lorentz factor is of order Γ. So the positions R lie just above the "knees" in the profiles, which separate fluid elements that have already expanded from those that have not. When $|x - t| \gg R/\Gamma^2$ or, equivalently, $|\chi| \to \infty$, all profiles approach the $t = 0$ power law since at $t = 0$, $|\chi| \to \infty$ everywhere behind the front. When $|x - t| \ll R/\Gamma^2$, the $t < 0$ profiles approach a constant ($\gamma \to \Gamma/\sqrt{2}$) and the $t > 0$ profiles approach $\gamma \propto |x - t|^{-1}$ ($g \propto \chi^{-1}$ from Eq. 4.36). Because every fluid element is always accelerating, the $t < 0$ profiles always lie below the $t = 0$ power law and the $t > 0$ profiles are always above the $t = 0$ power law. Trajectories of individual fluid elements before breakout are given by Eq. 4.25. After breakout, Eq. 4.25 still applies. The power laws relating t to $g\chi$ stay the same after breakout since the equations for g before and after breakout are nearly identical; also, matching the pre- and post-breakout trajectories at $t = 0$ gives the same $|t_0|$ in the evolution both before and after $t = 0$.

4.4.2 Type I or Type II?

While the flow before breakout follows a Type II self-similar solution, the solution describing the flow after breakout contains elements of Type I and Type II solutions. Unlike the Type II solution that applies before breakout, the post-breakout solution does not contain a sonic point. Differentiating Eq. 4.36 with respect to $g\chi$ shows that the only local extremum of $g\chi$ occurs at $g = \infty$ or $\chi = 0$, where $g\chi = 4+2\sqrt{3}-2k\sqrt{3}$; since $g\chi \to \infty$ as $\chi \to \infty$, $g\chi$ must attain its global minimum at $\chi = 0$. But then for $k < 0$ neither the sonic point, $g\chi = 4-2\sqrt{3}$, nor the other singular points, $g\chi = 2$ and $g\chi = 4 + 2\sqrt{3}$, is included in the solution after breakout. A more physical argument for the exclusion of the sonic point from the post-breakout solution is that since each fluid element is accelerating while Γ decreases with time, the fluid element moves forward relative to R and its χ must decrease with time. Using Eq. 4.23 we see that $D\chi/Dt < 0$ requires $g\chi > 2 > 4 - 2\sqrt{3}$ for every fluid element. Then the entire post-breakout solution is causally connected as would be expected if it were Type I.

Unlike Type I solutions, however, the solution after breakout contains infinite energy. As a result, global conservation laws do not apply just as would be expected in a Type II solution. So the post-breakout solution lies between the standard Type I and Type II solution categories. While this unusual situation implies that, in principle, the infinite energy contained in the solution can communicate with and affect the region near the front, the regions of the solution containing this infinite energy lie arbitrarily far behind $x = t$ and therefore take arbitrarily long to communicate with the fluid near the front. Similarly, in any application of the post-breakout solution, the flow will be truncated at some position well behind R, potentially introducing a spatial scale into the problem. However, the solution is valid until information from the truncation region propagates to areas close to the front. The further the truncation from the front, the longer this will take.

4.4.3 Behavior of fluid elements at late times

While in the post-breakout solution described above the fluid elements formally accelerate forever, each fluid element must in practice stop accelerating when all of its internal energy has been converted to bulk kinetic energy, or when $p/n \sim \gamma f/h \sim 1$. Then we can estimate the final Lorentz factor of a given fluid element from Eqs. 4.36, 4.37, 4.38. By taking the advective time derivatives of γ and of f/h we can write differential equations for their time evolution following a single fluid element. These are

$$\frac{D\gamma}{Dt} = \frac{\gamma}{t}\frac{\left(\sqrt{3}-3\right)k}{g\chi-4-2\sqrt{3}} \simeq \frac{\gamma}{t}\left(\frac{\sqrt{3}-1}{2}\right) \tag{4.39}$$

$$\frac{D(f/h)}{Dt} = \frac{(f/h)}{t}\left[\frac{(2-g\chi)+\left(g\chi-4-2\sqrt{3}+2k\sqrt{3}\right)}{g\chi-4-2\sqrt{3}}\right] \times \frac{k}{-1+k\sqrt{3}-\sqrt{3}} \tag{4.40}$$

$$\simeq \frac{(f/h)}{t}\left(\frac{-1}{\sqrt{3}}\right) \quad . \tag{4.41}$$

In the last steps we have taken the limit of late times when the accelerating fluid element approaches the front at $\chi = 0$. In this limit Eq. 4.36 implies $g \to \infty$ and $g\chi \to (g\chi)_0 = 4 + 2\sqrt{3} - 2k\sqrt{3}$. Let γ_0, f_0, and h_0 be the values of the functions in question just after our fluid element is shocked; then at late times $\gamma \gg \gamma_0$ so $(f/h)/(f_0/h_0) \sim \gamma^{-1}$. Integrating the above differential equations then gives

$$\frac{\gamma}{\gamma_0} = \left(\frac{t}{t_0}\right)^{\left(\sqrt{3}-1\right)/2} \sim \gamma^{\left(3-\sqrt{3}\right)/2} \quad \longrightarrow \quad \gamma \sim \gamma_0^{1+\sqrt{3}} \quad . \tag{4.42}$$

We know the fluid is thermally hot just behind the front: though p approaches 0 as χ approaches 0, n approaches 0 there faster than p does, and p/n actually increases toward the front. So the hottest fluid lies at the front of the solution, and we expect the cold fluid elements to lie behind it. Fluid elements at the back of the solution were shocked before fluid elements near the front, so elements at the back have smaller γ_0 values and smaller ratios $\gamma_0^{\sqrt{3}}$ between the final and initial Lorentz factors than do

those near the front. It turns out that the elements at the back cool faster than those near the front. We can see this by checking that $\overline{g\chi}$, the value of $g\chi$ that satisfies $p/n \sim 1$, decreases—that is, moves toward the front of the solution—with time:

$$1 \sim \frac{p}{n} \sim \Gamma\sqrt{g}\frac{f}{h} \propto t^{-m/2}\sqrt{g(\overline{g\chi})}\frac{f(\overline{g\chi})}{h(\overline{g\chi})} \tag{4.43}$$

$$\frac{d\ln\overline{g\chi}}{d\ln t} = -\frac{\overline{g\chi}-(g\chi)_0}{\overline{g\chi}}\cdot\frac{\overline{g\chi}-2}{\overline{g\chi}-2(3+4/\sqrt{3})} < 0 \tag{4.44}$$

where, again, we have used Eqs. 4.36, 4.37, 4.38.

Because the fluid is hot near the front, the relativistic hydrodynamic equations and equation of state apply there and our self-similar solutions should hold. However, to confirm the solutions' validity for fluid near the front, we need to check that information from the cold fluid at the back cannot reach the hot fluid before it cools. To do this we look at the forward characteristics, which we denote by $g\chi_+$. In the frame of the unshocked fluid, the speed of a sound wave with $\beta_s = 1/\sqrt{3}$ travelling forward relative to the flow moving at $\beta \simeq 1 - 1/2\gamma^2 = 1 - 1/\Gamma^2 g$ is

$$\frac{dx_+}{dt} = \frac{\beta+\beta_s}{1+\beta\beta_s} \simeq 1 - \frac{1}{\Gamma^2 g}\frac{\sqrt{3}-1}{\sqrt{3}+1} \tag{4.45}$$

so we have

$$\frac{d\chi_+}{dt} \simeq (1+2(m+1)\Gamma^2)\left(1-\frac{dx_+}{dt}\right)\frac{1}{t} - (m+1)\frac{\chi_+}{t} \tag{4.46}$$

$$\frac{d\ln g\chi_+}{d\ln t} = \frac{d\ln g\chi_+}{d\ln\chi_+}\frac{d\ln\chi_+}{d\ln t} = -\frac{g\chi_+-(g\chi)_0}{g\chi_+}\cdot\frac{g\chi_+-4+2\sqrt{3}}{g\chi_+-4-2\sqrt{3}} \quad . \tag{4.47}$$

For $g\chi > (g\chi)_0$, $d\ln\overline{g\chi}/d\ln t$ is always more negative than $d\ln g\chi_+/d\ln t$: by the time sound waves moving forward from the cold fluid reach a given fluid element farther forward, that fluid element has become cold. So the self-similar solution is valid for the hot fluid near the front. In the last line we have used Eq. 4.36. While the sound wave propagating along the forward characteristic may in principle move through both hot and cold fluid, the fluid temperature given by the self-similar solution is an upper bound on the actual temperature of the fluid, so Eq. 4.47 gives the path of the

fastest possible forward-moving sound wave.

4.4.4 Relation to previous work

The first analytic investigation of an ultrarelativistic planar shock wave was performed by Johnson & McKee (1971). The problem they consider is broadly similar to the one we discuss here, but our work differs in important respects from theirs. First, Johnson & McKee (1971) used the method of characteristics in their work: they analyzed the flow associated with the shock by tracing the paths of sound waves travelling through the fluid. Our analysis uses the self-similarity of the flow instead. So while some of their work can be applied to flows moving through fluids with arbitrary decreasing density profiles, their methods do not give profiles for the hydrodynamic variables as functions of x at a given time. By contrast, our self-similar solutions require a power-law density profile inside the star but give explicit profiles for the hydrodynamic variables. Second, the methods used by Johnson & McKee (1971) require initial conditions consisting of a uniform stationary hot fluid about to expand into cold surroundings. In our scenario the hot expanding fluid is never uniform or stationary and always follows the self-similar profile specified by our solution. The self-similarity analysis tells us that the solution is Type II, at least before breakout; this implies that the asymptotic solution is independent of the initial engine.

The behavior of individual fluid elements at very late times indicates that our asymptotic solution is consistent with the findings of Johnson & McKee (1971): according to both our and their solutions, the final Lorentz factor is $\gamma \sim \gamma_0^{1+\sqrt{3}}$ for a fluid element with initial Lorentz factor γ_0 in a strong ultrarelativistic shock propagating into a cold medium with decreasing density. The agreement provides additional support for our claim that the solution outside the star behaves like the solution describing a standard planar shock up to the initial conditions and the interpretation of the characteristic values R, Γ, P, N. Note that the differences between the initial conditions used in their work and in ours are unimportant to the scaling law relating the final and initial Lorentz factors of a given fluid element. This result agrees with

the findings of Tan et al. (2001) concerning the scaling law: partly because of uncertainty over the different initial conditions, they used numerical simulations to check the $\gamma \sim \gamma_0^{1+\sqrt{3}}$ result.

Recently, Nakayama & Shigeyama (2005) also investigated the problem of an ultrarelativistic planar shock. While the self-similar solution they give for the flow before breakout is identical to the one in Sari (2006) and outlined here, they do not give analytic results for or a physical interpretation of the self-similar solution after breakout. The case of a nonrelativistic planar shock approaching the edge of a polytropic atmosphere was studied by Gandel'man & Frank-Kamenetskii (1956) and Sakurai (1960); both papers investigate the nonrelativistic pre-breakout flow and asymptotic $t \to 0$ profiles. Sakurai (1960) also plots some nonrelativistic post-breakout profiles obtained via numerical integration.

4.5 Comparison with numerical integrations

To verify our results numerically, we integrated the time-dependent relativistic hydrodynamic equations using a one-dimensional code. Figure 4.2 shows curves for γ as a function of position at a single time before breakout, while Figure 4.4 shows the time evolution of Γ, P, and N before breakout. The numerical and analytic results are in excellent agreement. Figures 4.3 and 4.5 respectively show the γ versus x profile and time evolution of Γ, P, and N after breakout; the agreement between numerical and analytic results here confirms the choice of scale $R(t)$ after breakout that we discussed in § 4.1.

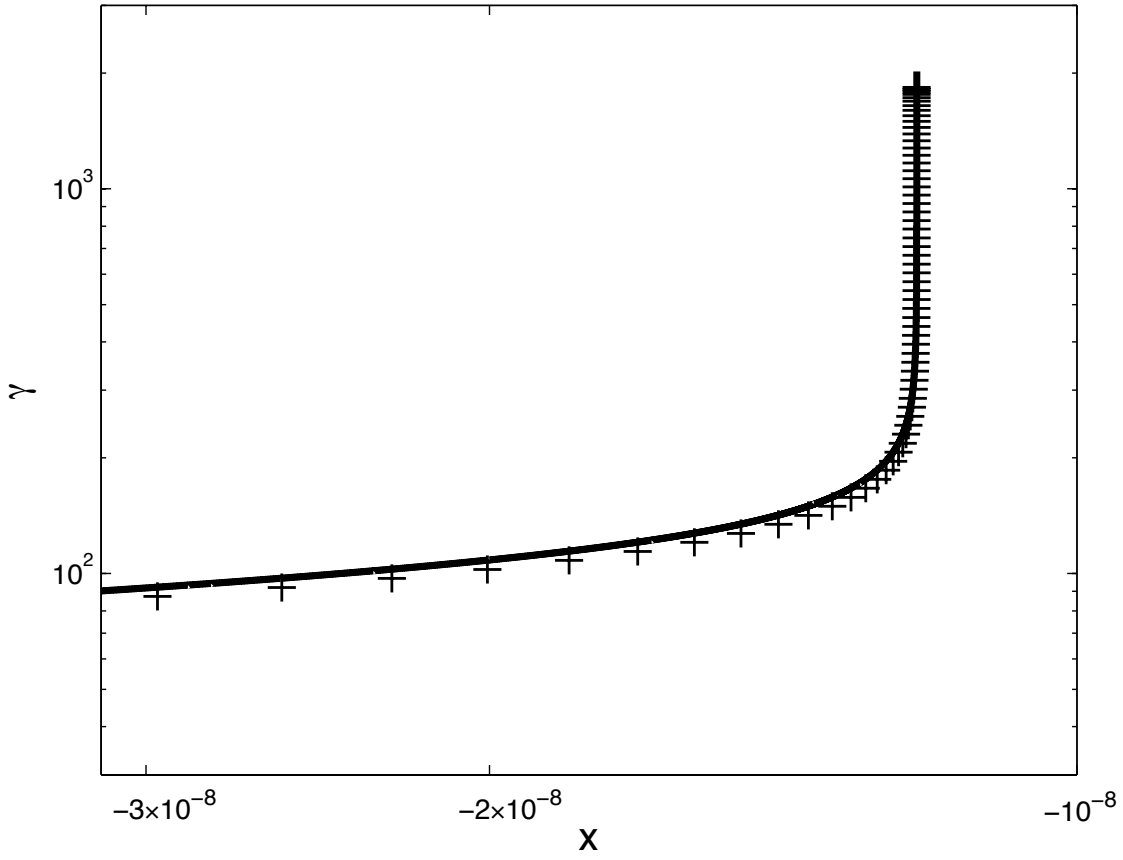

Figure 4.2: Lorentz factor γ as a function of position x shortly before the shock breaks out of the star. The density profile has power-law index $k = -1.5$. The analytic profile taken from the self-similar solution (solid line) agrees well with the numerical profile (crosses).

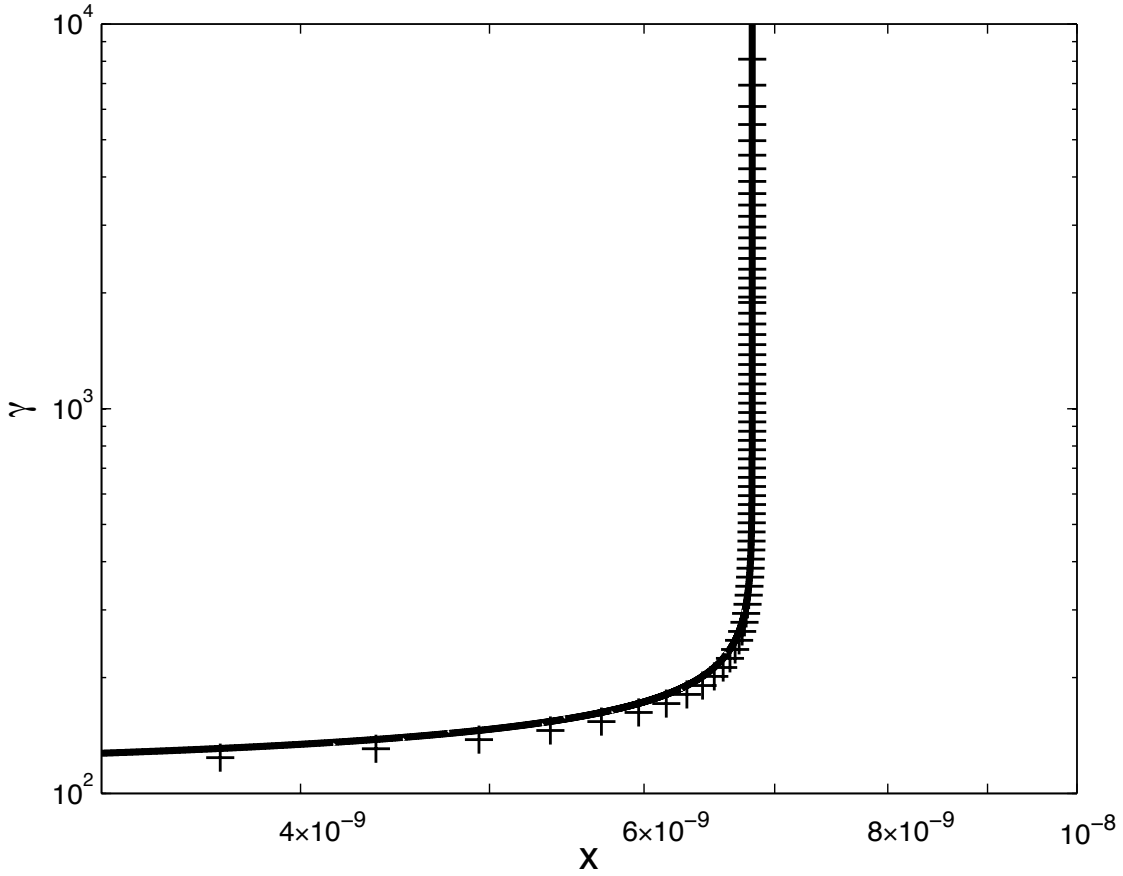

Figure 4.3: Same as Figure 4.2 but for a time shortly after the shock emerges from the star.

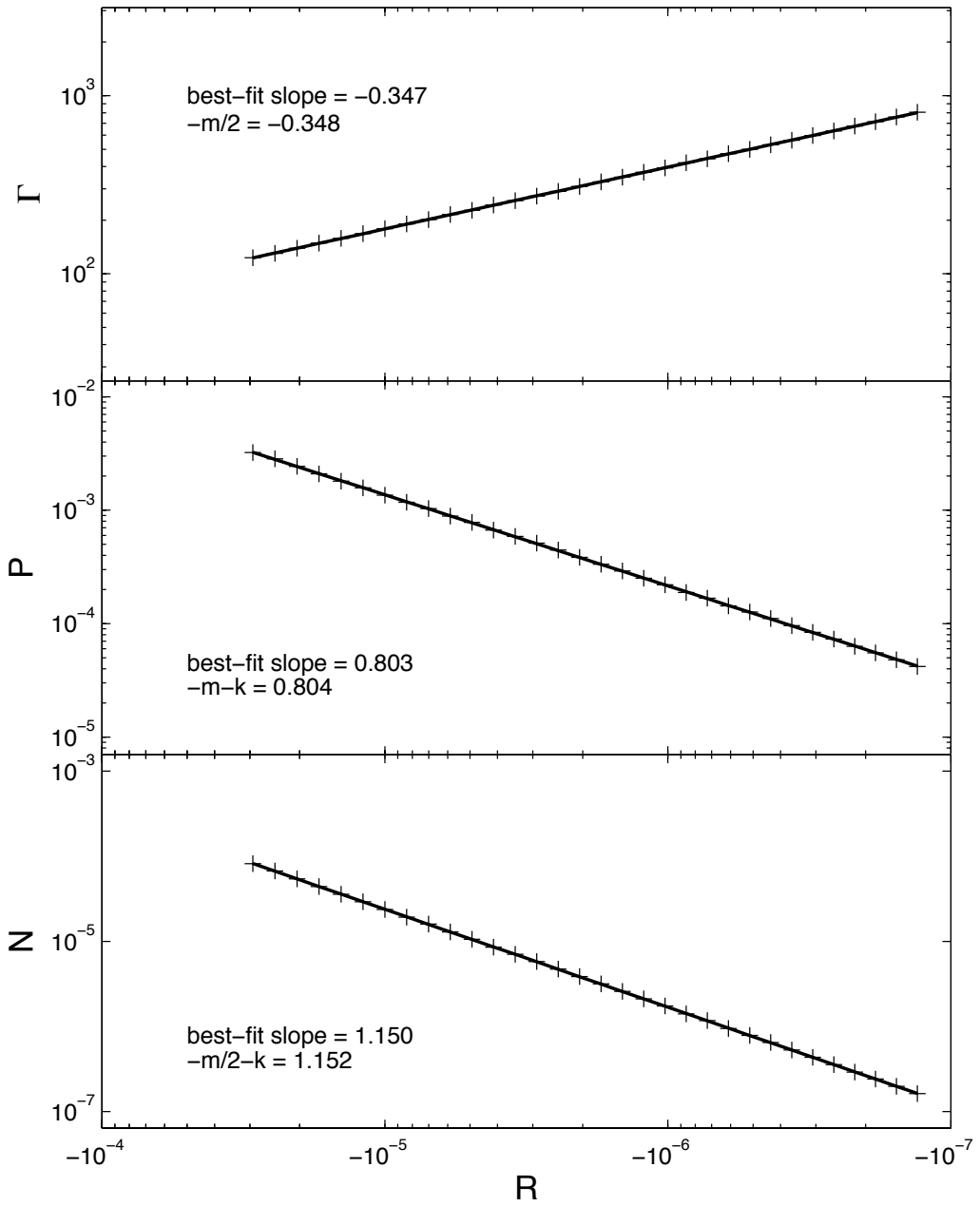

Figure 4.4: Evolution of Γ (top panel), P (middle panel), and N (bottom panel) with R while the shock is still inside the star. The density profile has power-law index $k = -1.5$. The evolution of Γ, P, N with R is equivalent to time evolution when $\Gamma \gg 1$. Crosses represent numerical data; solid lines are the best-fit lines to the data. That the data are well fit by lines implies that Γ, P, and N do indeed evolve as power laws; that the numerical and analytic slopes agree confirms that the evolution is as expected.

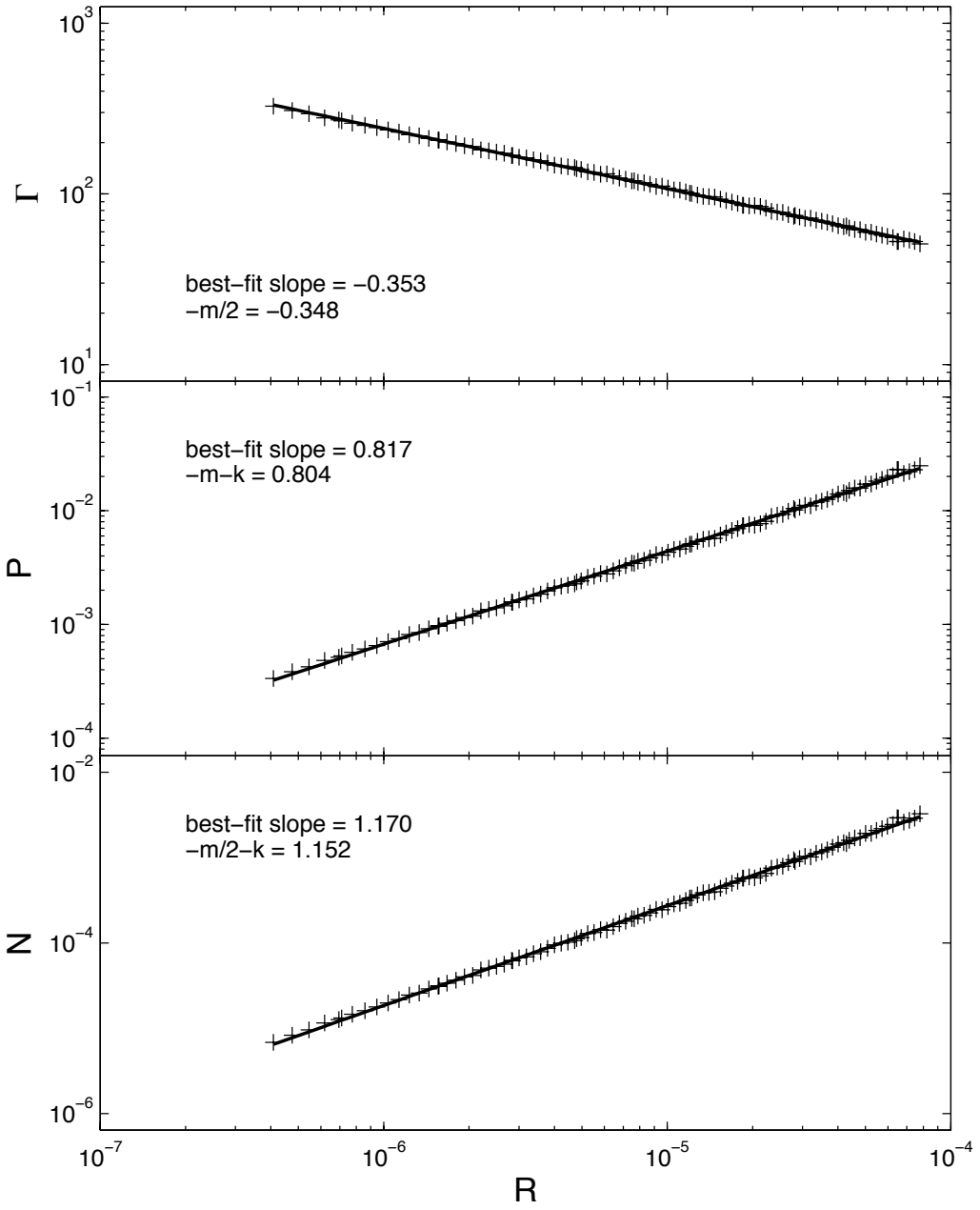

Figure 4.5: Same as Figure 4.4 but for times after the shock emerges from the star. Γ, P, N, and R were deduced from the numerical data by finding at each time the position where $\gamma^{-1}p/n$, the ratio of the thermal and the bulk kinetic energies in the frame of the fluid, fell just below the constant value we expect at the time of breakout.

4.6 Summary

We have shown that, given an ultrarelativistic shock propagating into a planar polytropic envelope, the flow upon the shock's emergence from the envelope into vacuum follows a self-similar solution strikingly similar to the self-similar solution describing the flow while the shock remains within the envelope. Both self-similar solutions obey the same relations with regard to the time evolution of the characteristic quantities R, Γ, P, N and with regard to the similarity variables χ, g, f, h. The pre- and post-breakout solutions differ only in that the applicable ranges in χ and the physical interpretations of the characteristic quantities differ. As a result of these differences, the behavior of the flow after breakout lies somewhere between the traditional Type I and Type II classes of self-similar solutions; before breakout a Type II solution applies. To arrive at these results we have looked in detail at the behavior when the shock reaches the outer edge of the envelope.

We have discussed these results in the context of an application—the motion of a shock wave through a polytropic envelope near the surface of a star, the shock's emergence from the surface, and the subsequent flow into vacuum. This situation may be related to the explosions believed to cause gamma-ray bursts and supernovae (see, for example, Tan et al., 2001) and should be especially relevant in very optically thick media such as neutron stars.

Acknowledgements. This chapter was originally published in 2006 in the *Astrophysical Journal*. It is reproduced here with the permission of the copyright holder, the American Astronomical Society.

Chapter 5

Self-similar solutions for relativistic shocks: the transition to cold fluid temperatures

5.1 Introduction

The energy and Lorentz factor that we expect in the ejecta in supernovae and gamma-ray bursts are important because they constrain the amount of energy that can be deposited in the photons we observe from these explosions. Previous work on the ejecta, notably Tan et al. (2001), uses as a starting point the analytic solutions of Johnson & McKee (1971) for a planar relativistic shock propagating into cold surroundings: by the time the shock reaches the outer envelope of the star, the likely source of the ejecta, it has accelerated to relativistic speeds and its geometry is planar. The work of Johnson & McKee (1971) and other analytic work on the flow from a relativistic shock that breaks out of a star (Nakayama & Shigeyama, 2005; Pan & Sari, 2006) show that significant acceleration occurs after the fluid is shocked. As the hot fluid expands adiabatically, its thermal energy is converted to bulk kinetic energy.

Since these authors assume an ultrarelativistic equation of state for the fluid, the final Lorentz factor their solutions predict for the fluid is formally infinite as the fluid never cools. They avoid this difficulty by following fluid elements in the flow only to the point where the fluid temperature becomes nonrelativistic and approximating

the final coasting Lorentz factor as the one given by their solutions at that point. They thus find that the final Lorentz factor of a given fluid element scales as $\gamma_0^{1+\sqrt{3}}$ where γ_0 is the Lorentz factor acquired by the fluid when it is shocked. This method neglects effects that occur around the time when the fluid cools to nonrelativistic temperatures and can only produce approximate relations for the energy and velocity of the ejecta. Also, since previous analytic work on the post-breakout flow assumes the fluid is hot, the portion of the flow for which this work is valid decreases with time as more and more of the flow becomes cold.

We approach this problem by introducing a new kind of self-similar solution for the cooling and expanding fluid. In this solution, we require that the fluid move at relativistic speeds but relax the assumption that the fluid be hot. We place the characteristic position at the point where the fluid temperature becomes nonrelativistic. We thus exploit the self-similarity of the transition between hot and cold fluid in the flow rather than the self-similarity in the acceleration of the hot fluid. Indeed, this flow when taken in its entirety is not self-similar: the size scales that characterize the acceleration and the hot/cold transition evolve with time according to different power laws. We derive this new solution in §2 and discuss its relation to previous self-similar solutions for the post-breakout flow in §3. In §4 we find the terminal velocities of fluid elements in the flow and compare our analytic results to numerical simulations. In §5 we summarize our findings. We take the speed of light to be $c = 1$ throughout our discussion.

5.2 Self-similar solution for the cooling fluid

We are interested in the behavior at late times of a fluid flow that begins as a relativistic shock propagating through the outer layers of a star with a polytropic envelope. We understand the behavior of the part of the flow that is hot ($p/n \gg 1$) and therefore obeys the equation of state $p = e/3$: it follows the self-similar solution given in Eqs. 4.8–4.13, 4.17–4.19, and 4.36–4.38. We note for convenience in our discussion

below that the self-similar variable χ, as given by Eq 4.9, is equivalent to

$$\chi = \frac{t - x}{t - R} \tag{5.1}$$

taken in the limit where $\Gamma \gg 1$, or where $t \simeq R(1 + 1/(2(m + 1)\Gamma^2)$. The implied characteristic length scale is $t - R = R/(2(m + 1)\Gamma^2)$.

As the fluid expands and accelerates after breakout, it cools adiabatically from the back of the flow towards the front. At late times, then, the above post-breakout solution, which we will refer to here as the "hot solution," holds only for a region at the very front of the flow, and this region shrinks with time. The hot solution sets the boundary conditions for the new solution we seek: as we approach the vacuum interface at $\chi = 0$, the two solutions must coincide.

In the new solution, which we will refer to as the "cooling solution," we must include cold fluid. We therefore use the equation of state

$$p = \frac{1}{3}(e - n) \tag{5.2}$$

rather than the ultrarelativistic $p = e/3$. We must also specify a characteristic scale and define the characteristic Lorentz factor, pressure, and number density to be consistent with this scale.

We seek the profiles of the hydrodynamic variables in the region where the fluid temperature transitions from hot to cold. The natural scale for this transition is the distance δ between the vacuum interface, where the fluid is hottest, and the point where the fluid temperature becomes nonrelativistic. We set this point to be where $p/n = 1$. Then the similarity variable is

$$\xi = \frac{t - x}{\delta} \tag{5.3}$$

and, by analogy with the hot solution, we express γ, p, and n as

$$\gamma^2(x, t) = \frac{1}{2}\bar{\Gamma}^2(t)\bar{g}(\xi) \tag{5.4}$$

$$p(x,t) = \bar{P}(t)\bar{f}(\xi) \tag{5.5}$$

$$n(x,t) = \bar{N}(t)\frac{\bar{h}(\xi)}{\bar{g}^{1/2}(\xi)} \quad . \tag{5.6}$$

We choose $\bar{\Gamma}$, $\bar{P}$, and $\bar{N}$, the new characteristic values of the Lorentz factor, pressure, and number density, to match the γ, p, and n values given by the hot solution where $p/n = 1$. We take $\chi_{\rm cold}$ to be the value of the old similarity variable χ corresponding to $p/n = 1$ in the hot solution:

$$\bar{\Gamma}^2 = \Gamma^2 g(\chi_{\rm cold}) \tag{5.7}$$

$$\bar{P} = P f(\chi_{\rm cold}) \tag{5.8}$$

$$\bar{N} = N\frac{h(\chi_{\rm cold})}{g^{1/2}(\chi_{\rm cold})} \quad . \tag{5.9}$$

This choice of characteristic values dictates

$$\bar{P} = \bar{N} \quad . \tag{5.10}$$

In the limit of late times, when $\delta \ll R/\Gamma^2$ and $g\chi - g\chi_0 \ll g\chi_0$, Eqs. 5.7 and 5.1 give

$$g\chi_0\frac{\Gamma^2}{\bar{\Gamma}^2} \simeq \chi_{\rm cold} \simeq \frac{\delta}{t-R} \simeq \delta \cdot \frac{2(m+1)\Gamma^2}{t} \tag{5.11}$$

$$\delta = \frac{g\chi_0}{2(m+1)}\frac{t}{\bar{\Gamma}^2} = \left(2+\sqrt{3}\right)\frac{t}{\bar{\Gamma}^2} \quad . \tag{5.12}$$

Note that the characteristic scale $t - R \sim R/\Gamma^2$ in the post-breakout solution for the hot fluid is unrelated to the new scale δ. R is the location of a fluid element that has expanded by a factor of order unity since breakout. Because R evolves according to the finite characterisitic Lorentz factor Γ, R lags farther and farther behind the front of the flow, where the Lorentz factors are arbitrarily large. Since Γ decreases with time as per Eq. 4.8, $t - R$ increases with time. In the limit of late times, then, R lags far behind the portion of the flow where the fluid remains hot and $t - R$ becomes much larger than the space occupied by the hot fluid. In other words, the scale $t - R$

that characterizes the hot solution becomes irrelevant to the transition between hot and cold fluid that is of interest here.

To get $\bar{\Gamma}$ and δ as functions of time, we apply Eqs. 4.36, 4.37, 4.38 at the point $p/n = 1$. We use $P/N = \Gamma/(3\sqrt{2})$, a relation that follows from the shock jump conditions applied in the pre-breakout solution.

$$1 = \frac{p}{n} = \frac{\Gamma}{3\sqrt{2}} \frac{\sqrt{g(\chi_{\rm cold})} f(\chi_{\rm cold})}{h(\chi_{\rm cold})} \tag{5.13}$$

$$= \frac{\Gamma}{3\sqrt{2}} \left[g(\chi_{\rm cold})\right]^{\frac{1}{m}\left(\frac{3m}{2}+k+\frac{m(2k-1)}{-1-\sqrt{3}+k\sqrt{3}}\right)} \left[g(\chi_{\rm cold})\cdot\chi_{\rm cold}-2\right]^{\frac{-k}{-1-\sqrt{3}+k\sqrt{3}}} \tag{5.14}$$

$$\bar{\Gamma}^2 = \Gamma^2 g(\chi_{\rm cold}) \tag{5.15}$$

$$= \Gamma^2 \left(\frac{3\sqrt{2}}{\Gamma} \left(g(\chi_{\rm cold})\cdot\chi_{\rm cold}-2\right)^{\frac{k}{-1-\sqrt{3}+k\sqrt{3}}} \right)^{m/\left(\frac{m}{2}-\frac{k}{-1-\sqrt{3}+k\sqrt{3}}\right)} . \tag{5.16}$$

This gives

$$2a = \frac{2t\dot{\bar{\Gamma}}}{\bar{\Gamma}} = \frac{\left(3-2\sqrt{3}\right)k}{1-\sqrt{3}-3\left(2-\sqrt{3}\right)k} \tag{5.17}$$

$$\frac{t\dot{\delta}}{\delta} = \frac{1-\sqrt{3}-\left(12-7\sqrt{3}\right)k}{1-\sqrt{3}-3\left(2-\sqrt{3}\right)k} . \tag{5.18}$$

Solving Eq. 5.13 for $f(\chi_{\rm cold})$ or $h(\chi_{\rm cold})/\sqrt{g(\chi_{\rm cold})}$ similarly gives

$$b = \frac{t\dot{\bar{P}}}{\bar{P}} = \frac{t\dot{\bar{N}}}{\bar{N}} = -\frac{4k}{1+\sqrt{3}+3k} . \tag{5.19}$$

We now proceed to solve the hydrodynamic equations. We use the equation of state Eq. 5.2 to rewrite Eq. 4.4, Eq. 4.6, and the difference equation obtained by subtracting Eq. 4.5 from Eq. 4.4. We take the limit $\gamma \gg 1$. We rewrite the differentiation operators as

$$\frac{\partial}{\partial t} = \dot{\bar{\Gamma}}\frac{\partial}{\partial\bar{\Gamma}} + \dot{P}\frac{\partial}{\partial P} + \dot{N}\frac{\partial}{\partial N} + \frac{1}{\delta}\left(1-\xi\dot{\delta}\right)\frac{\partial}{\partial\xi} \tag{5.20}$$

$$\frac{\partial}{\partial x} = -\frac{1}{\delta}\frac{\partial}{\partial \xi} \tag{5.21}$$

and substitute these and Eqs. 5.70-5.10, 5.17, and 5.19 to get

$$\begin{aligned} 0 &= b\left(2\bar{f} + \frac{\bar{h}}{\bar{g}^{1/2}}\right) + \frac{t}{\delta\bar{\Gamma}^2}\left[-\bar{g}'\left(4\frac{\bar{f}}{\bar{g}^2} + \frac{3}{2}\frac{\bar{h}}{\bar{g}^{5/2}}\right) + \frac{4\bar{f}'}{\bar{g}} + \frac{\bar{h}'}{\bar{g}^{3/2}}\right] \\ &\quad - \xi\frac{t\dot{\delta}}{\delta}\left[-\frac{\bar{g}'}{2}\frac{\bar{h}}{\bar{g}^{3/2}} + 2\bar{f}' + \frac{\bar{h}'}{\bar{g}^{1/2}}\right] \end{aligned} \tag{5.22}$$

$$\begin{aligned} 0 &= (2a+b)\left(2\bar{g}\bar{f} + \frac{\bar{h}\bar{g}^{1/2}}{2}\right) + \frac{t}{\delta\bar{\Gamma}^2}\left[-\frac{\bar{g}'}{4}\frac{\bar{h}}{\bar{g}^{3/2}} + \bar{f}' + \frac{\bar{h}'}{2\bar{g}^{1/2}}\right] \\ &\quad - \xi\frac{t\dot{\delta}}{\delta}\left[\bar{g}'\left(2\bar{f} + \frac{\bar{h}}{4\bar{g}^{1/2}}\right) + 2\bar{f}'\bar{g} + \frac{\bar{h}'}{4}\bar{g}\right] \end{aligned} \tag{5.23}$$

$$0 = (a+b)\bar{h} + \frac{t}{\delta\bar{\Gamma}^2}\left[-\bar{g}'\frac{\bar{h}}{\bar{g}^2} + \frac{\bar{h}'}{\bar{g}}\right] - \xi\frac{t\dot{\delta}}{\delta}\bar{h}' \quad . \tag{5.24}$$

We substitute Eqs. 5.12 and 5.18 into Eqs. 5.22, 5.23, and 5.24 and integrate this ODE system numerically to produce the solution shown in Figures 5.1, 5.2, and 5.3.

We can check that the behavior of this solution at large ξ—where the fluid is very cold and where the hot solution and cooling solution differ most—is physical. Consider a fluid element far behind the vacuum interface at position $x \ll t - \delta$. This fluid element must have become cold at some time $t_{\rm cold} \ll t$; as a result, it has long since stopped accelerating and has spent most of the time interval $t - t_{\rm cold}$ coasting at its current Lorentz factor γ. Then this fluid element has

$$\xi = \frac{t-x}{\delta} \simeq \frac{t - (t - t_{\rm cold})\sqrt{1 - 1/\gamma^2}}{\delta} \simeq \frac{t/\left(\bar{\Gamma}^2\bar{g}\right)}{t/\bar{\Gamma}^2 \cdot \left(2+\sqrt{3}\right)} = \frac{2-\sqrt{3}}{\bar{g}} \tag{5.25}$$

so at large ξ we expect

$$\bar{g}\xi = 2 - \sqrt{3} \quad . \tag{5.26}$$

We cannot get exact relations for $\bar{f}$ and $\bar{h}$ in the large ξ limit in this way because p and n change significantly while the fluid element finishes its acceleration. However, we can check the scalings of $\bar{f}$ and $\bar{h}$ with ξ. Because the fluid elements far behind

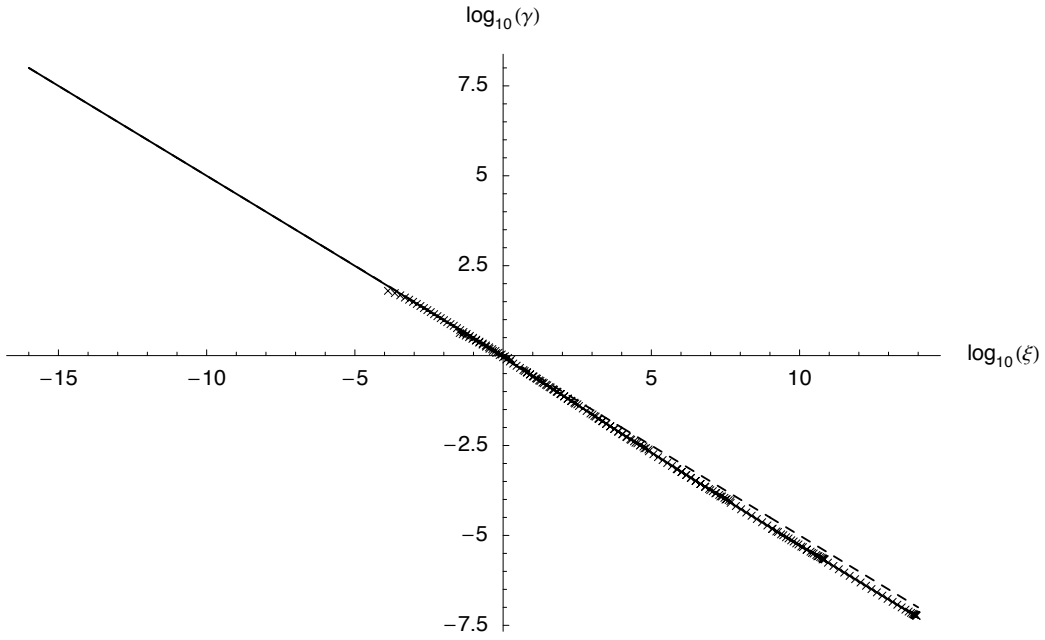

Figure 5.1: Profile of the Lorentz factor γ as a function of the similarity variable ξ. The dashed line is the hot solution valid for the fluid near the front, at small ξ; the solid line is the cooling solution. Data from numerical simulations are shown as crosses. In order to cover a substantial range in ξ, data from six γ vs. ξ profiles corresponding to different times in the same simulation run are shown. The data agree well with the cooling solution. The overall y-axis normalization is arbitrary, but the relative normalizations of the hot solution, the cooling solution, and the numerical simulations are correct.

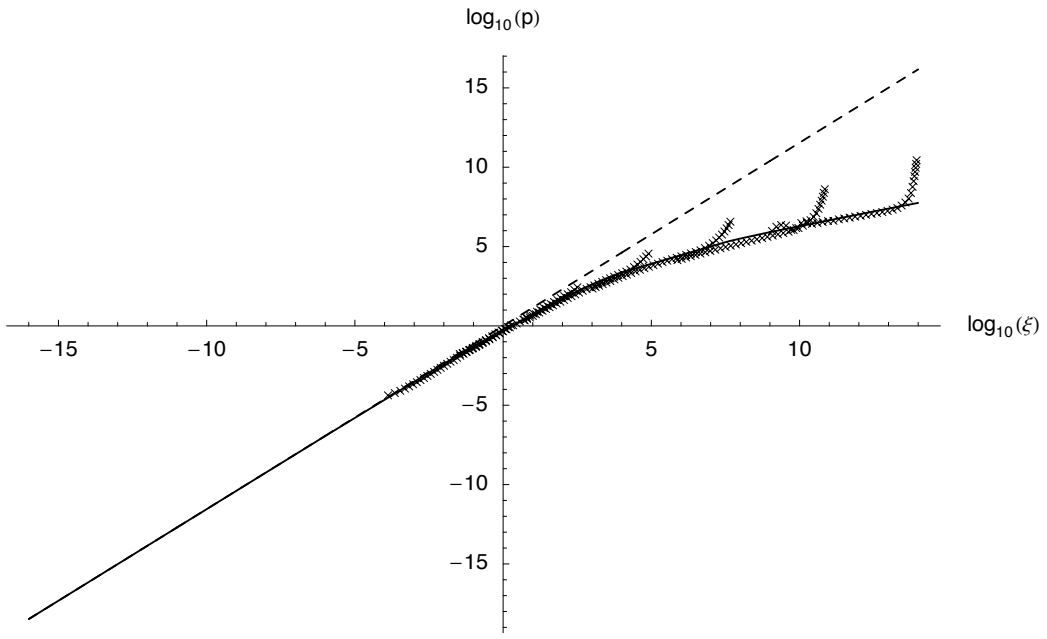

Figure 5.2: Same as Figure 5.1 for the pressure p rather than γ. The "tails" at the ends of the numerical simulation profile data are due to edge effects at the ends of the simulation grid that are not self-similar.

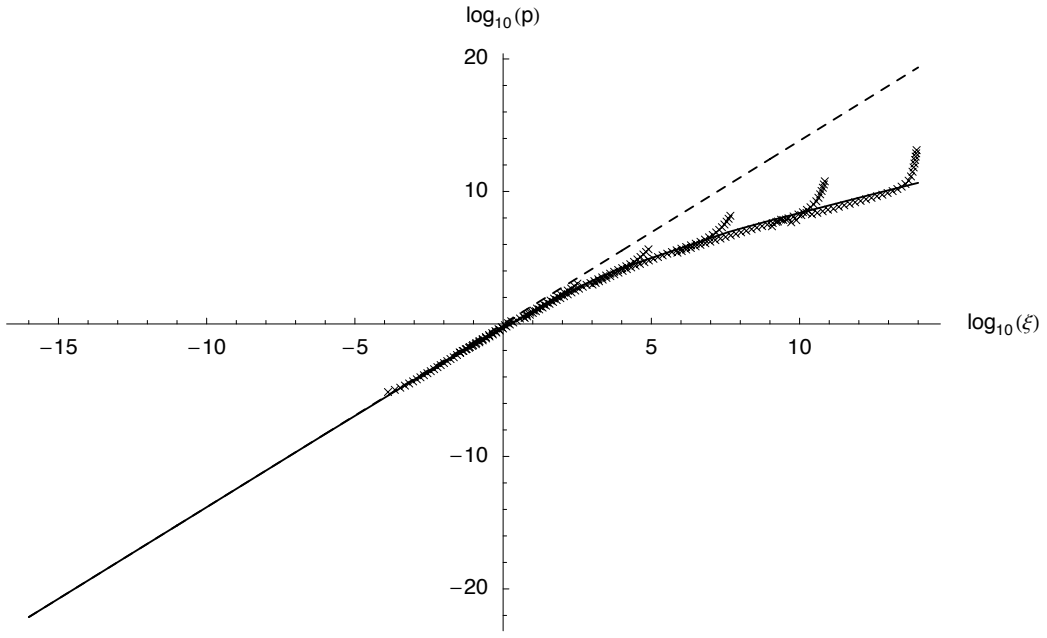

Figure 5.3: Same as Figure 5.2 for the number density n rather than p.

the front are coasting with Lorentz factors that are virtually constant in time, the volume of each fluid element increases linearly with time. This implies

$$n \propto t^{-1} \quad , \quad p \propto n^{4/3} \propto t^{-4/3} \tag{5.27}$$

for a single fluid element. From the definitions of $\bar{\Gamma}$, $\bar{P}$, and $\bar{N}$ in Eqs. 5.7, 5.8, and 5.9, we know $\gamma(\xi = 1)/\bar{\Gamma}$, $p(\xi = 1)/\bar{P}$, and $n(\xi = 1)/\bar{N}$ are constant in time. Then for a single fluid element,

$$p = p(t_{\rm cold}) \left(\frac{t}{t_{\rm cold}} \right)^{-4/3} \propto t_{\rm cold}^{b+4/3} \quad . \tag{5.28}$$

Since

$$\bar{g} = \frac{2\gamma^2}{\bar{\Gamma}^2(t)} \propto \frac{\bar{\Gamma}^2(t_{\rm cold})}{\bar{\Gamma}^2(t)} \propto t_{\rm cold}^{2a} \quad , \tag{5.29}$$

we have

$$\xi \propto t_{\rm cold}^{-2a} \propto p^{-\frac{2a}{b+4/3}} \quad \longrightarrow \quad p \propto \xi^{-\frac{b+4/3}{2a}} \quad . \tag{5.30}$$

A similar calculation yields

$$n \propto \xi^{-\frac{b+1}{2a}} \quad . \tag{5.31}$$

That the relations in Eqs. 5.26, 5.30, and 5.31 hold at large ξ is shown in Figure 5.4.

We can check that the behaviors of fluid elements and sound waves in the hot solution and the cooling solution are consistent. The characteristic position R in the hot solution moves backwards relative to the vacuum interface with time because Γ decreases with time. By contrast, the characteristic position $t - \delta$ in the cooling solution moves forwards relative to ct because fluid elements at the back of the solution cool faster than those at the front, and $t-\delta$ marks the location of a fluid element that has just cooled. We confirm the forward motion by looking at Eq. 5.18, which indeed gives $t\dot{\delta}/\delta < 0$ for the range of k of interest ($k < -1$). We expect fluid elements in the cooling solution to move backwards in the solution, or towards larger ξ: every fluid element must eventually finish accelerating and become cold, so the point $t - \delta$ that marks the hot/cold transition must overtake every fluid element. Fluid elements

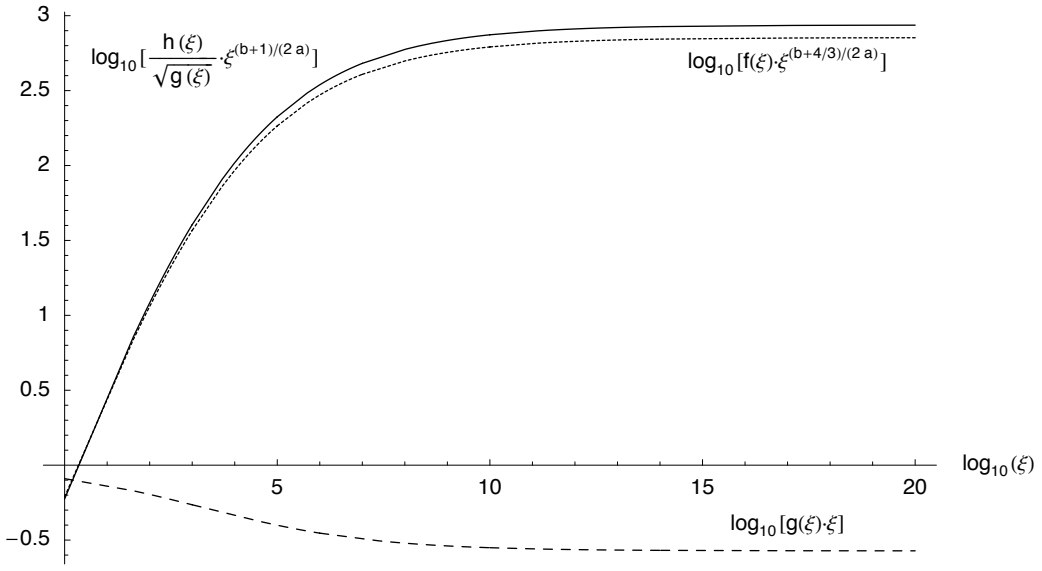

Figure 5.4: Verification of the scalings of $\bar{g}$, $\bar{f}$, and $\bar{h}$ with ξ at large ξ, or cold fluid temperatures. The functions plotted (dashed line for $\bar{g}$, dotted line for $\bar{f}$, solid line for $\bar{h}$) show that at large ξ the relations in Eqs. 5.26, 5.30, and 5.31 hold. In particular, $\bar{g}\xi$ approaches the expected value $2 - \sqrt{3} = 10^{-0.572}$.

in the hot solution move forwards in time since they accelerate while R decelerates.

If the proper sound speed in the fluid is $\beta_s = \sqrt{4/3}\bar{f}^{1/2}\bar{g}^{1/4}\bar{h}^{-1/2}$, then the motion of a sound wave in the new solution is given by

$$\frac{d\ln\xi_\pm}{d\ln t} = \frac{t}{\xi_\pm}\frac{1}{\delta}\left(1 - \frac{dx_\pm}{dt} - \xi_\pm\dot{\delta}\right) = \frac{2-\sqrt{3}}{\bar{g}\xi}\left(\frac{1\mp\beta_s}{1\pm\beta_s}\right) - \frac{t\dot{\delta}}{\delta} \tag{5.32}$$

where the signs denote forward- and backward-propagating sound waves. Since $t\dot{\delta}/\delta < 0$, $d\xi_\pm/dt > 0$ everywhere and all sound waves move backwards in the cooling solution. In other words, all fluid elements are disconnected from the vacuum interface. In the sense that the front is disconnected from the fluid far back in the flow, the cooling solution is similar to Type II solutions. However, in contrast to the usual Type II scenario, there is no sonic point constraining the solution.

5.3 Behavior of fluid elements at late times

Earlier analytic work has established that the final Lorentz factor $\gamma_{\rm final}$ of a given fluid element should scale according to

$$\gamma_{\rm final} = K\gamma_{\rm shocked}^{1+\sqrt{3}} \tag{5.33}$$

where $\gamma_{\rm shocked}$ is the fluid element's Lorentz factor immediately after it is shocked in the pre-breakout flow and the coefficient K is independent of $\gamma_{\rm shocked}$ (Johnson & McKee, 1971; Pan & Sari, 2006). Tan et al. (2001) have found numerically that $K \simeq 2.6$ for $k = -3$. They note, and we confirm from our own experience, that it is difficult to continue numerical simulations until the very end of the fluid acceleration since the conversion of thermal to bulk kinetic energy is quite slow. To derive their scaling relation, Tan et al. (2001) applied correction factors to their simulation results of up to $\sim$50% for fluid elements with final Lorentz factors of order $\sim 10^3$.

We can find $\gamma_{\rm final}$ for a given fluid element directly from our pre- and post-breakout solutions. To track the acceleration of the fluid element while it is hot, we take the advective time derivative of γ in the pre- and post-breakout solution for the hot fluid and integrate with the proper limits.

$$\frac{D\gamma}{Dt} = \frac{\gamma}{t}\frac{\left(\sqrt{3}-3\right)k}{g\chi - 4 - 2\sqrt{3}} \tag{5.34}$$

$$\frac{Dg\chi}{Dt} = \frac{1}{t}\frac{(2-g\chi)\,(g\chi - g\chi_0)}{g\chi - 4 - 2\sqrt{3}} \tag{5.35}$$

$$\frac{D\gamma}{Dg\chi} = \gamma\,\frac{\left(\sqrt{3}-3\right)k}{(2-g\chi)(g\chi - g\chi_0)} \tag{5.36}$$

Before breakout, the fluid element's $g\chi$ goes from $g\chi = 1$ when it is shocked to $g\chi \to -\infty$ at breakout. After breakout, the fluid element's $g\chi$ goes from $g\chi \to \infty$ to $g\chi \simeq g\chi_{\rm cold}$. So when the fluid becomes cold, we have

$$\gamma = \gamma_{\rm shocked}(g\chi_0 - 1)^{\frac{(\sqrt{3}-3)k}{g\chi_0 - 2}}\left(\frac{g\chi - 2}{g\chi - g\chi_0}\right)^{\frac{(\sqrt{3}-3)k}{g\chi_0 - 2}} \quad . \tag{5.37}$$

To find the correct $g\chi$ at which to evaluate the above, we set $C = \gamma f/h$ to be the temperature (up to a factor of 3) at the $g\chi$ of interest and use Eqs. 4.37, 4.38 to express $(g\chi - 2)/(g\chi - g\chi_0)$ in terms of C. This gives

$$\gamma = C^{-\sqrt{3}} \gamma_{\rm shocked}^{\sqrt{3}+1} \quad . \tag{5.38}$$

To this we add the extra factor given by the solution shown in Figure 5.1 to get

$$\gamma_{\rm final} = 1.95 \gamma_{\rm shocked}^{\sqrt{3}+1} \qquad k = -3 \tag{5.39}$$

$$\gamma_{\rm final} = 2.71 \gamma_{\rm shocked}^{\sqrt{3}+1} \qquad k = -3/2 \quad . \tag{5.40}$$

This result is close to the results of Tan et al. (2001), who find a coefficient of ~ 2.6 when $k = -3$. Note that $p/n = 1$ corresponds to $C^{-\sqrt{3}} = 0.149$: γ grows by a factor of ~ 15 after the fluid element becomes nominally cold.

The growth of γ as a function of the temperature for a single fluid element is shown in Figure 5.5, which also shows good agreement between the cooling solution and direct numerical simulations of the hydrodynamic equations. Because the Lorentz factors near the front of the flow in particular become very large at late times, it is difficult to produce numerical simulations that remain accurate as the fluid cools all the way to $p/n \ll 1$. As a result, the numerical simulation shown in Figure 5.5 cuts off while the fluid Lorentz factor is 9% smaller than the final Lorentz factor predicted by the cooling solution.

5.4 Summary

We have derived a new self-similar solution, the cooling solution, for the flow that results when a relativistic shock breaks out of a polytropic envelope. The cooling solution is based on our identification of the characteristic position with the point where the fluid cools to nonrelativistic temperatures. The cooling solution shows that the transition between hot and cold fluid in the flow is self-similar even though

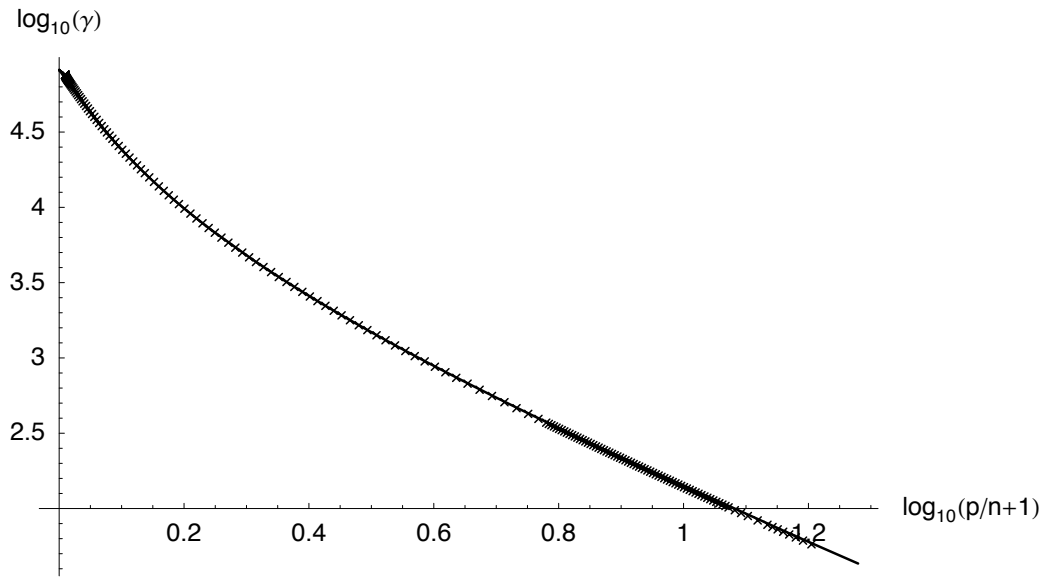

Figure 5.5: Lorentz factor γ of a single fluid element as a function of the temperature p/n of that fluid element. Lower temperatures and later times are towards the left. The solid line is the self-similar solution; the points are the results of numerical simulations. Both calculations were done for $k = -3$.

this transition is not included—indeed, is not self-similar—in the old post-breakout solution for the hot fluid alone. The cooling solution allows an accurate calculation of the final Lorentz factors of the shocked fluid elements.

Bibliography

Asphaug, E., & Benz, W. 1996, Icarus, 121, 225

Beaugé, C. 1994, Celestial Mechanics and Dynamical Astronomy, 60, 225

Benz, W., & Asphaug, E. 1999, Icarus, 142, 5

Bernstein, G. M., Trilling, D. E., Allen, R. L., Brown, M. E., Holman, M., & Malhotra, R. 2004, AJ, 128, 1364

Best, P., & Sari, R. 2000, Physics of Fluids, 12, 3029

Blandford, R. D., & McKee, C. F. 1976, Physics of Fluids, 19, 1130

Brown, M. E. 2001, AJ, 121, 2804

Bruno, A. D. 1994, The Restricted 3-Body Problem: Plane Periodic Orbits (Berlin: Walter de Gruyter)

Chiang, E. I., & Brown, M. E. 1999, AJ, 118, 1411

Chiang, E. I., Jordan, A. B., Millis, R. L., Buie, M. W., Wasserman, L. H., Elliot, J. L., Kern, S. D., Trilling, D. E., Meech, K. J., & Wagner, R. M. 2003, AJ, 126, 430

Davis, D. R., & Farinella, P. 1997, Icarus, 125, 50

Dermott, S. F., & Murray, C. D. 1983, Nature, 301, 201

Dohnanyi, J. W. 1969, J. Geophys. Res., 74, 2531

Farinella, P., & Davis, D. R. 1996, Science, 273, 938

Ford, E. B., Havlickova, M., & Rasio, F. A. 2001, Icarus, 150, 303

Frangakis, C. N. 1973, ApSS, 22, 421

Gandel'man, G. M., & Frank-Kamenetskii, D. A. 1956, Soviet Phys. Dokl., 1, 223

Gladman, B., Kavelaars, J. J., Nicholson, P. D., Loredo, T. J., & Burns, J. A. 1998, AJ, 116, 2042

Goldreich, P., Lithwick, Y., & Sari, R. 2002, Nature, 420, 643

Goldreich, P. M., Lithwick, Y., & Sari, R. 2004, ARA&A, 42, 549

Greene, J. M. 1979, Journal of Mathematical Physics, 20, 1183

Harris, A. W. 1996, in *Lunar and Planetary Institute Conference Abstracts*, 493–494

Holman, M. J., & Wisdom, J. 1993, AJ, 105, 1987

Holsapple, K. A. 1994, Planet. Space Sci., 42, 1067

Housen, K. R., & Holsapple, K. A. 1990, Icarus, 84, 226

Jewitt, D., & Luu, J. 1993, Nature, 362, 730

Jewitt, D. C., & Sheppard, S. S. 2002, AJ, 123, 2110

Johnson, M. H., & McKee, C. F. 1971, Phys. Rev. D, 3, 858

Kenyon, S. J. 2002, PASP, 114, 265

Landau, L. D., & Lifshitz, E. M. 1959, *Fluid Mechanics* (Oxford: Pergamon Press)

Love, S. G., & Ahrens, T. J. 1996, Icarus, 124, 141

Malhotra, R. 1996, AJ, 111, 504

Malhotra, R., Duncan, M. J., & Levison, H. F. 2000, in *Protostars and Planets IV*, ed. V. Mannings, A. P. Boss, & S. S. Russell (Tucson: University of Arizona Press), 1231–+

Malyshkin, L., & Tremaine, S. 1999, Icarus, 141, 341

Melosh, H. J., Nemchinov, I. V., & Zetzer, Y. I. 1994, in *Hazards Due to Comets and Asteroids*, ed. T. Gehrels, M. S. Matthews, & A. M. Schumann, 1111–1132

Melosh, H. J., & Ryan, E. V. 1997, Icarus, 129, 562

Message, P. J. 1958, AJ, 63, 443

Message, P. J. 1970, in *On Asymmetric Periodic Solutions of the Plane Restricted Problem of Three Bodies*, ed. Giacaglia, G. E. O. (Dordrecht: D. Reidel Publishing Company), 19–32

Message, P. J., & Taylor, D. B. 1978, in *Dynamics of Planets and Satellites and Theories of Their Motion*, ed. Szebehely, V. (Dordrecht: D. Reidel Publishing Company), 319–323

Nakayama, K., & Shigeyama, T. 2005, ApJ, 627, 310

Nesvorný, D., & Roig, F. 2001, Icarus, 150, 104

O'Brien, D. P., & Greenberg, R. 2003, Icarus, 164, 334

Pan, M., & Sari, R. 2004, AJ, 128, 1418

—. 2005, Icarus, 173, 342

—. 2006, ApJ, 643, 416

Pravec, P., Wolf, M., & Sarounova, L. 1998, Icarus, 136, 124

Rasio, F. A., & Ford, E. B. 1996, Science, 274, 954

Sakurai, A. 1960, Comm. Pure & App. Math., 13, 353

Sari, R. 2006, Physics of Fluids, 18

Sedov, L. I. 1946, Appl. Math. Mech. Leningrad, 10, 241

Tan, J. C., Matzner, C. D., & McKee, C. F. 2001, ApJ, 551, 946

Tanaka, H., Inaba, S., & Nakazawa, K. 1996, Icarus, 123, 450

Taylor, G. I. 1950, Proc. R. Soc. London Ser. A, 201, 175

Trujillo, C. A., Jewitt, D. C., & Luu, J. X. 2001, AJ, 122, 457

von Neumann, J. 1947, Blast Waves, Tech. Rep. 7, Los Alamos National Laboratories

Waxman, E., & Shvarts, D. 1993, Physics of Fluids, 5, 1035

Williams, D. R., & Wetherill, G. W. 1994, Icarus, 107, 117

Winter, O. C., & Murray, C. D. 1997a, A&A, 319, 290

—. 1997b, A&A, 328, 399

Wisdom, J. 1980, AJ, 85, 1122

Zel'dovich, Y. B., & Raizer, Y. P. 1967, *Physics of Shock Waves and High-Temperature Phenomena* (New York: Academic Press)